

Energetic ion composition and acceleration mechanisms in the magnetosphere of Jupiter

Von der Fakultät für Physik und Geowissenschaften
der Technischen Universität Carolo-Wilhelmina
zu Braunschweig
zur Erlangung des Grades einer
Doktorin der Naturwissenschaften
(Dr.rer.nat.)
genehmigte
Dissertation

von Aikaterini Radioti
aus Ptolemaida/Griechenland

Bibliografische Information Der Deutschen Bibliothek

Die Deutsche Bibliothek verzeichnet diese Publikation in der Deutschen Nationalbibliografie; detaillierte bibliografische Daten sind im Internet über <http://dnb.ddb.de> abrufbar.

1. Referentin oder Referent: Prof. Dr. K.-H. Glassmeier

2. Referentin oder Referent: Prof. Dr. D. C. Hamilton

eingereicht am: 13 Februar 2006

mündliche Prüfung (Disputation) am: 2 Mai 2006

Copyright © Copernicus GmbH 2006

ISBN ISBN 3-936586-56-X

Copernicus GmbH, Katlenburg-Lindau

Druck: Schaltungsdienst Lange, Berlin

Printed in Germany

Vorveröffentlichungen der Dissertation

Teilergebnisse aus dieser Arbeit wurden mit Genehmigung der Fakultät für Physik und Geowissenschaften, vertreten durch den Mentor oder den Betreuer der Arbeit, in folgenden Beiträgen vorab veröffentlicht:

Publikation

Radioti A., N. Krupp, J. Woch, A. Lagg, K.-H. Glassmeier, L. S. Waldrop, *Ion abundance ratios in the Jovian magnetosphere*, J. Geophys. Res., 110, A07225, doi:10.1029/2004JA010775, 2005.

Tagungsbeiträge

Radioti A., J. Woch, N. Krupp, A. Lagg, K.-H. Glassmeier, *The magnetosphere of Jupiter - A unique plasma laboratory* (Poster), 40th Culham Plasma Physics Summer School, Oxford, UK, 2003

Radioti A., N. Krupp, J. Woch, A. Lagg, K.-H. Glassmeier, *Plasma composition in the Jovian magnetosphere* (Poster), Deutsche Physikalische Gesellschaft (DPG)- Arbeitsgemeinschaft Extraterrestrische Forschung (AEF), Frühjahrstagung, Kiel, Germany, 2004

Radioti A., N. Krupp, J. Woch, A. Lagg, K.-H. Glassmeier, *Ion abundance ratios in the Jovian magnetosphere* (Talk), European Geophysical Union (EGU), First General Assembly, Nice, France, 2004

Radioti A., N. Krupp, J. Woch, A. Lagg, K.-H. Glassmeier, *Energy dependence of the Jovian ion abundance ratios - Ion acceleration by Alfvén waves* (Talk), European Geophysical Union (EGU), Wien, Austria, 2005

Radioti A., N. Krupp, J. Woch, A. Lagg, K.-H. Glassmeier, *Jovian ion energy spectra - Ion stochastic acceleration by Alfvén waves* (Talk), The International Association of Geomagnetism and Aeronomy (IAGA), Toulouse, France, 2005

Radioti A., N. Krupp, J. Woch, A. Lagg, K.-H. Glassmeier, *Ion stochastic acceleration by Alfvén waves: Implications for the energetic ion composition in the Jovian magnetosphere* (Poster), Magnetospheres of the Outer Planets (MOP), Leicester, UK, 2005

Contents

Contents	5
List of Figures	7
List of Tables	11
Abstract	13
1 Magnetospheric systems	15
1.1 The magnetosphere of the Earth as a prototype	15
1.2 The Jovian magnetosphere	17
1.2.1 The magnetospheric configuration	19
1.2.2 Plasma sources and transport	21
1.3 Particle acceleration and ion energy spectra	26
1.4 Ion abundances of the Jovian magnetosphere	33
1.5 Summary and outline	39
2 Instrumentation used	41
2.1 The Galileo mission	41
2.2 The EPD instrument	43
2.2.1 The Composition Measurement System (CMS)	45
2.2.2 The Low Energy Magnetosphere Measurement System (LEMMS)	49
2.2.3 Record and real time mode	51
2.3 Test of the reliability of the dataset	52
3 Ion composition in the Jovian magnetosphere as derived by Galileo measurements	57
3.1 Ion energy spectra in Jovian magnetosphere	57
3.2 Ion abundance ratios	60
3.2.1 Global maps	64
3.2.2 Local time asymmetries	68
3.2.3 Ion composition during reconfiguration events	74
3.2.4 Temporal variations	77
3.2.5 Comparison with Voyager 2 results	81
3.3 Summary	88

4	Ion acceleration mechanisms	89
4.1	Ion stochastic acceleration by Alfvén waves	89
4.2	Ion acceleration during the reconfiguration events	94
4.2.1	Acceleration in the current sheet	94
4.2.2	Acceleration during small scale variations of the magnetic field lines	98
5	Summary and conclusions	109
	Bibliography	111
	Acknowledgements	119
	Curriculum Vitae	121

List of Figures

1.1	A sketch of the magnetosphere of the Earth	16
1.2	A sketch of the spacecraft trajectories of all missions to Jupiter	18
1.3	A sketch of the Jovian magnetosphere	20
1.4	A sketch of the flow of particles through the Io torus	21
1.5	Schematic representation of convection-corotation equipotentials	22
1.6	Flow pattern in the equatorial plane of the Jovian magnetosphere - Galileo measurements	23
1.7	Schematic representation of the plasma flow and magnetic field	24
1.8	Anisotropy vectors in the equatorial plane of the Jovian magnetosphere - Galileo measurements	25
1.9	Charged particle motion in the Jovian magnetosphere	27
1.10	Recirculation model	28
1.11	Schematic representation of the current sheet ion acceleration model	29
1.12	Proton ion energy spectra - Voyager 2 measurements	31
1.13	Ion energy spectra - Galileo measurements	32
1.14	He/p ratio - Pioneer 10 measurements	33
1.15	Ion abundance ratios - Voyager 2 measurements	34
1.16	Oxygen and sulfur energy spectra - Voyager 2 measurements	35
1.17	Ion composition pattern - Voyager 2 measurements	36
1.18	p/He ²⁺ flux ratio - Ulysses measurements	37
1.19	S/O abundance ratio - Galileo HIC measurements	38
2.1	The Galileo interplanetary trajectory	42
2.2	A sketch of the Galileo spacecraft	43
2.3	A sketch of the Energetic Particles Detector	44
2.4	View of the EPD instrument	45
2.5	Graphical summary of EPD channels	46
2.6	Time of Flight energy channel matrix	48
2.7	$\Delta E \times E$ energy channel matrix	48
2.8	Sketch of the Composition Measurement System telescope	49
2.9	Sketch of the Low Energy Magnetosphere Measurement System telescope	51
2.10	Sulfur energy spectra	52
2.11	Comparison between the cps of the three EPD telescopes - energy spectra described by power law cutoff	53
2.12	Comparison between the cps of the three EPD telescopes - energy spectra described by power law	54

2.13	Helium energy spectra of the magnetosphere of the Earth	55
3.1	Proton, helium and oxygen ion energy spectra at Earth and Jupiter	58
3.2	Proton, helium, oxygen and sulfur ion energy spectra	59
3.3	Ion energy spectra in pairs	60
3.4	The first 15 orbits of Galileo projected on the x-y and x-z plane	61
3.5	Proton, helium, oxygen and sulfur differential intensities - C10 orbit	62
3.6	Proton, helium, oxygen and sulfur differential intensities - the first 15 orbits of Galileo	63
3.7	S/O ion abundance ratio - C10 orbit	64
3.8	S/O abundance ratio along the first 15 orbits of Galileo	65
3.9	S/O, S/He, O/He and p/He global maps	66
3.10	S/O ion abundance ratio along the first 15 orbits of Galileo - separation of the 8 local time sectors is shown	69
3.11	S/O abundance ratio along the 6 local time sectors	70
3.12	S/He abundance ratio along the 6 local time sectors	71
3.13	O/He abundance ratio along the 6 local time sectors	72
3.14	p/He abundance ratio along the 6 local time sectors	73
3.15	S/O ion abundance ratio together with first order anisotropy and magnetic field - G2 orbit	74
3.16	S/O, S/He, O/He and p/He ion abundance ratios along a part of the G2 orbit	75
3.17	S/O, S/He, O/He and p/He ion abundance ratios - separation between bursts events and quiet time	76
3.18	S/O, S/He, O/He and p/He ion abundance ratios along a part of the G2 orbit	77
3.19	E6 and G8 Galileo orbits	78
3.20	Temporal variations of the S/O, S/He, O/He and p/He ion abundance ratios	79
3.21	Temporal variations for sulfur, oxygen, protons and helium intensities	80
3.22	Global map of S/O ion abundance ratio together with the Voyager 2 tra- jectory	81
3.23	Ion energy spectra from low and high energy channels in pairs	82
3.24	Ion energy spectra by Galileo and Voyager 2	83
3.25	S/O ion abundance ratio compared with the Voyager 2 results	84
3.26	S/He ion abundance ratio compared with the Voyager 2 results	84
3.27	O/He ion abundance ratio compared with the Voyager 2 results	85
3.28	p/He ion abundance ratio compared with the Voyager 2 results	85
3.29	S/O, S/He, O/He and p/He abundance ratios along a part of the G8 orbit compared with the Voyager 2 results	86
3.30	Oxygen and helium ion differential intensities compared with the Voyager 2 results	87
4.1	Wave spectra observations	91
4.2	Ion energy spectra fit as derived by the model of ion stochastic acceleration	92
4.3	Schematic illustration of the current sheet model for Jupiter	95
4.4	Ion final energy (in keV) as a function of their initial energy (in keV).	96
4.5	Ion final energy (keV/nuc) as a function of their initial energy (keV/nuc) for quiet and disturbed periods	97

4.6	South-north component of the magnetic field for a reconfiguration event	98
4.7	North-south magnetic field - Induced electric field	100
4.8	Schematic illustration of the simplified dipolarization model	101
4.9	Particle's energy as a function of $\chi = \frac{\tau}{\tau_g}$	102
4.10	Particle's energy as a function of the time scale of the magnetic field duration τ	103
4.11	Ion energy spectra before and after the acceleration due to dipolarization	105
4.12	S/O, S/He, O/He and p/He ion abundance ratios along a part of the G2 orbit - comparison with the model	106
4.13	S/O, S/He, O/He and p/He ion abundance ratios as a function of the time scale of the magnetic field variation τ	107

List of Tables

2.1	Galileo Energetic Particle Detector - general characteristics	45
2.2	CMS energy channels	47
2.3	LEMMS energy channels	50
3.1	The E/nuc that fits best the EPD TOF energy channels	61
3.2	Ion abundance ratios in the Jovian magnetosphere.	67
4.1	Initial parameters for the model of stochastic acceleration	90
4.2	Final parameters as derived by the model of stochastic acceleration	93
4.3	Ion abundance ratios during quiet and disturbed time	105

Abstract

Based on the first 15 orbits of the Galileo spacecraft the composition of the energetic ion population of the Jovian magnetosphere has been studied for the first time on a global scale. More specific, three different types of ions are investigated: helium as the tracer of the solar wind, sulfur and oxygen to a large extent as tracers of the internal source Io and protons with a mixed origin from the solar wind, Jovian atmosphere/ionosphere and the Europa gas torus. The ion energy spectrum fundamental for the study of the ion composition is investigated and a characteristic shape is established as a distinct feature of the Jovian magnetosphere. Based on the observed ion energy spectra the relative ion abundance ratios of S/O, S/He, O/He and p/He at a specific energy/nucleon are derived and global maps are constructed. The global coverage of the Galileo trajectories enables a quantitative comparison with results of previous flyby missions for the same radial distance and local time. The large discrepancies derived from the comparison with the Voyager 2 results are attributed to temporal variations and to a strong energy dependence of the ion abundance ratios associated with the energy spectral shapes. The ion energy spectra are further discussed in terms of ion stochastic acceleration by Alfvén waves. Temporal variations of the ion abundance ratios not only on time scales of several years but also of several weeks, only implied by previous missions are now established. They are attributed to the different ion sources but also to time-varying acceleration processes. A comparative study of the ion composition for different local time sectors is for first the time investigated. It is shown that pronounced composition changes along the predawn sector are associated with reconfiguration processes that occur in the magnetotail. The composition in this region is studied in terms of two acceleration mechanisms: nonadiabatic ion interaction with the current sheet where ions are accelerated by the time-stationary dusk to dawn convection electric field and ion acceleration due to small-scale variations of the south-north component of the magnetic field during the reconfiguration events, where particles are accelerated by the induced electric field. It is concluded that the latter one is responsible for the observed ion composition.

1 Magnetospheric systems

The ancient Greeks, particular those that originate from the area called Magnesia, and also the Chinese knew of the existence of rare stones with the power to attract iron. At around 1000 the Chinese found that a steel needle stroked with such a stone, became magnetic and pointed north-south. The magnetic needle spreading in Europe was used by Columbus to navigate through the Atlantic ocean. It was only around 1600 that William Gilbert, physician to Queen Elizabeth I of England introduced the concept of the Earth behaving as a huge magnet.

The solar wind interacts with Earth's magnetic field creating a cavity called magnetosphere. Not only the Earth but many other planets are surrounded by this huge magnetic structure, sometimes larger than the planet itself. The strength of the magnetic field, the solar wind and the charged particle population within the magnetosphere determine its shape. All magnetospheres contain charged particles, however, the origin, the composition and the density of the particles may vary from planet to planet. The interaction of the particles with magnetic and electric fields trigger very complex physical mechanisms which are at least partly not well understood. To understand better the various acceleration and transport processes that the particles suffer the study of the ion composition is necessary.

This chapter gives an introduction of the Earth's magnetosphere, studied extensively for centuries by ground based observations, rockets and orbiting satellites and often used as a prototype. Jupiter's magnetosphere, which existence is known since a few decades, is also described pointing out the main morphological and dynamical characteristics, which are of prime interest in the context of this thesis.

1.1 The magnetosphere of the Earth as a prototype

Earth has a dipole magnetic moment of $8 \times 10^{15} \text{ Tm}^3$ which creates an equatorial magnetic field strength of 31.000 nT at the surface and 31 nT at 10 Earth radii (R_E). The solar wind, an almost collisionless plasma consisting of electrons and protons flowing outward from the Sun at supersonic speed interacts with the magnetic field of the Earth, distorts the magnetic field lines, forming a cavity known as the magnetosphere. Figure 1.1 shows a schematic representation of the basic structure of the terrestrial magnetosphere, the primary currents and its plasma regions. The internal configuration of a magnetosphere is the result of the superposition of a number of currents generated by the interaction of the solar wind and the interplanetary magnetic field with the planetary magnetic field and plasma.

Because the solar wind travels faster than any fluid plasma wave propagating in the

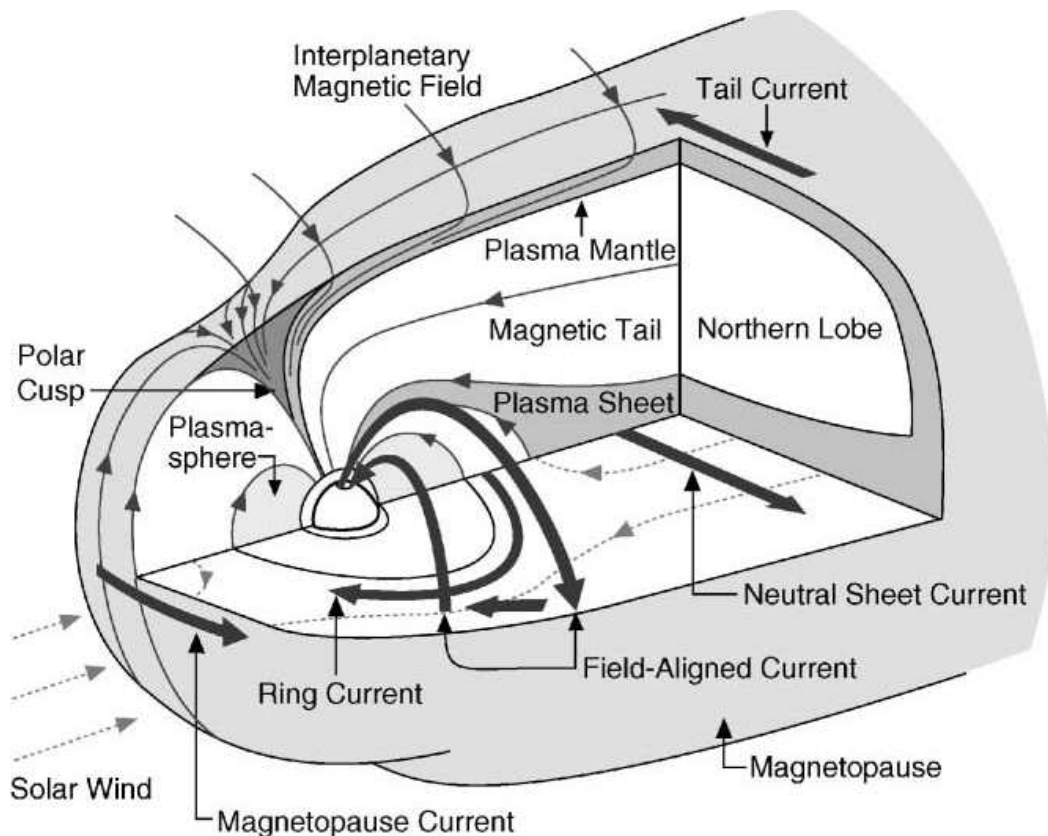


Figure 1.1: A sketch of the Earth's magnetosphere illustrating in three-dimensions its plasma regions and current systems (from Russell et al. (2001)).

magnetized solar wind plasma a standing shock wave, known as the bow shock, is created in front of the planet that slows, heats and deflects the solar wind plasma. The solar wind force compresses the dayside of the magnetosphere and pulls part of the magnetic field into a cylindrical magnetotail in the nightside. Even though the solar wind is deflected by the terrestrial magnetosphere, coupling between the magnetosphere and the solar wind does occur through the process of magnetic reconnection, initially proposed by Dungey (1961, 1963). By this process magnetic field lines in the solar wind merge with those of the planetary magnetosphere, increasing the tangential stress on the magnetosphere and adding magnetic energy to the magnetotail.

The balance between the solar wind pressure and the Earth's magnetic field pressure creates the outer magnetospheric boundary, the magnetopause. Upon the magnetopause flows the magnetopause current, a large current which separates the terrestrial magnetic field and the solar wind. The main role of this current is to rotate the field direction from that of the deflected solar wind to that of the magnetosphere. Additionally, it locally increases the strength of the magnetic field.

Close to the equatorial plane extending up to the tail lies the plasma sheet, a thick layer of hot plasma, mainly originating from the solar wind. North and south of the plasma sheet are the lobes, regions with oppositely directed magnetic flux. Even though these two regions are almost empty of plasma, the large volume of relatively strong magnetic

field is a reservoir of magnetic energy. The configuration with opposite magnetic field directions between the north and south magnetic lobe is maintained by a current sheet, the neutral sheet. The current sheet is embedded in the plasma sheet and the currents close along the magnetopause forming the tail current system.

Apart from the solar wind, plasma in the terrestrial magnetosphere originates also from the ionosphere. The ultraviolet radiation from the Sun is absorbed by the Earth's upper atmosphere and is partly ionized creating the ionosphere. The ionosphere, the physical link between the atmosphere and the magnetosphere supplies the magnetosphere with a dense population of ions and electrons. However these particles are initially only at thermal energies and are thus much less energetic than those coming from the solar wind. The extension of the ionosphere into the inner magnetosphere, where plasma motion is dominated by the corotation electric field is called the plasmasphere. The plasmasphere extends out to about 5 Earth radii. Within this distance magnetic flux tubes are filled up with cold plasma from the ionosphere.

Overlapping the plasmasphere and extending out to the plasma sheet the radiation belts are found. They are populated by high energy ionized particles, originating mainly from the solar wind and under specific conditions also from the ionosphere. The eastward (electrons) and westward (ions) particle drift in the radiation belts and generate the ring current. The ring current opposes the magnetopause current by decreasing the magnetic field strength on the surface of the Earth. Finally, field-aligned currents couple the Earth's ionosphere and magnetosphere. The field-aligned current system, which closes in pressure gradient regions in the equatorial magnetosphere, forces the flow in the ionosphere to follow the flow in the magnetosphere. It transports energy from the magnetosphere to the ionosphere where it is dissipated in the form of Joule heating and charged particle precipitation generating aurora.

The magnetospheric configuration is additionally influenced by the transfer of momentum and energy from the solar wind. The solar wind acts as a dynamo which sets up large scale magnetospheric and ionospheric plasma convection. The convection pattern in the inner part is strongly affected by the rotation of the Earth. The competing influence of the solar wind and the planetary rotation gives rise to the general plasma flow pattern indicated by dotted lines in Figure 1.1, with local time asymmetries and strong radial variations.

The purpose of this brief description of the Earth's magnetosphere is only to address the main morphological and configuration characteristics of the planet often used as prototype. The magnetosphere of Jupiter has many similarities with the terrestrial one. However important differences exist. The following section gives a detailed description of the Jovian magnetosphere, emphasizing on selected characteristics dealt with in this thesis.

1.2 The Jovian magnetosphere

By the mid 70s, while the Earth magnetosphere has already been investigated intensively both theoretically and observationally, the study of the Jovian magnetosphere was mainly restricted to the interpretation of the observed radio emissions (Burke and Franklin 1955, Carr and Gulkis 1969). Approximations of the planet's magnetic field, the inclination angle between the rotation and the dipole axis were the first achievements. Information

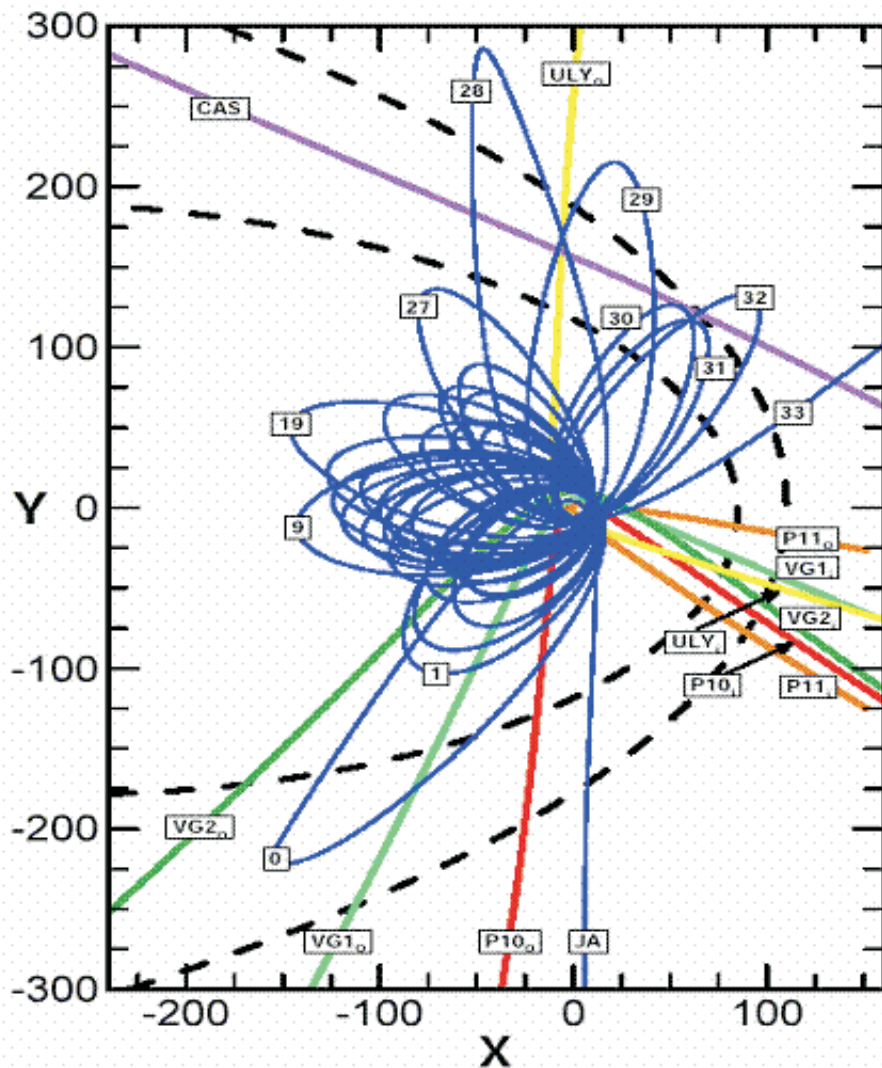


Figure 1.2: A sketch of the spacecraft trajectories of the previous missions to Jupiter projected in the $x - y$ plane of the Jupiter Solar Ecliptic (JSE) coordinate system with Jupiter at the center. The Sun is to the right and the dotted lines stand for the nominal bow shock and magnetopause location. Pioneer 10 and 11 flybys are presented by red and orange, Voyager 1 and 2 by light and dark green, Ulysses by yellow, Cassini by purple and the Galileo orbits by blue.

concerning the fundamental plasma properties like the ionic composition, and the plasma sources as well as the particle transport and acceleration processes was essentially not existing.

Some of the first theoretical models and preliminary derived properties of the Jovian magnetosphere were confirmed by in situ measurements of the flyby and orbiter missions to Jupiter and new perspectives for the exploration of the Jovian system were given. A comparative sketch of the spacecraft trajectories passing through the Jovian magnetosphere projected into Jupiter's equatorial plane is shown in Figure 1.2. Pioneer 10 reached

Jupiter in 1973, travelled mainly in the equatorial plane and sent back the first in situ data of the Jovian system. One year after its successful encounter, its sister spacecraft Pioneer 11 arrived at Jupiter in 1974, reaching northern latitudes of 30° , close to local noon. Voyager 1 and 2 passing by Jupiter in 1979, approached the planet within 5 and $10 R_J$ ^a and encountered the Galilean moons. Both missions were concentrated on the study of the Jovian atmosphere, the satellites and the magnetosphere. Pioneer and Voyager entered the magnetosphere at 9:00 - 10:00 local time (LT). Three of them left the magnetosphere through the dawn-predawn sector but only Pioneer 11 left it close to the local noon. Ulysses observations complemented and extended those of Pioneer and Voyager flybys. It was the first mission that passed through the dusk side of the magnetosphere reached magnetic latitudes of 45° . In addition, it carried instrumentation with different capacities compared to previous missions.

While before 1995 the exploration of the Jovian system was restricted only to flybys, a breakthrough in our knowledge was obtained by the first and up to now the only orbiter mission, Galileo. Galileo arrived at the giant planet in 1995 and completed 8 years of orbits around Jupiter, mainly in the equatorial plane. It provided an extended data set in radial distance and local time and among other instrumental improvements covered a broader ion energy range than the instrumentation on previous missions. A more detailed description of Galileo and its highlights are presented in Chapter 2.

Finally, Cassini, a mission destined to reach Saturn was launched in October 1997 and flew by Jupiter between October 2000 and April 2001, while Galileo was completing its 28th and 29th orbits. It was the first time that two spacecraft were investigating Jupiter simultaneously. Cassini offered measurements at the dusk flanks of the Jovian magnetosphere in the equatorial plane with the closest approach to Jupiter at $138 R_J$.

1.2.1 The magnetospheric configuration

The interior of Jupiter produces a surface magnetic field in the equatorial plane with an intensity of ~ 4 Gauss. This strong magnetic field and Jupiter's fast rotation with 9 h 55 min period creates a unique magnetosphere (Figure 1.3). The size of the Jovian magnetosphere with a standoff magnetopause distance of around $100 R_J$ is so large that if it would be seen from the Earth it would appear bigger than the moon. Jupiter's magnetosphere is divided into three main regions: the inner, the middle and the outer magnetosphere (Khurana et al. 2004).

Within $10 R_J$ from Jupiter (inner magnetosphere), the magnetic field configuration is dominated by the contribution from the planetary dipole. Unlike to the Earth's magnetosphere in this region most of the plasma is produced. The dense Io plasma torus lies between 5.2 and $10 R_J$, which consists of several hundreds tons of plasma diffusing slowly outwards. Jupiter's vast reservoir of plasma is confined to a thin plasma disk located close to the dipole magnetic equator. Due to Jupiter's fast rotation the plasma is enforced to corotate. The plasma β , the ratio of particle energy density to magnetic energy density, is <0.2 implying that the effect of the plasma on the configuration of the magnetic field in that region is minimal.

Beyond this region, in the middle magnetosphere ($10 R_J$ to $\sim 40 R_J$), the magnetic

^aThe Jovian radius (R_J) is 71.492×10^3 km.

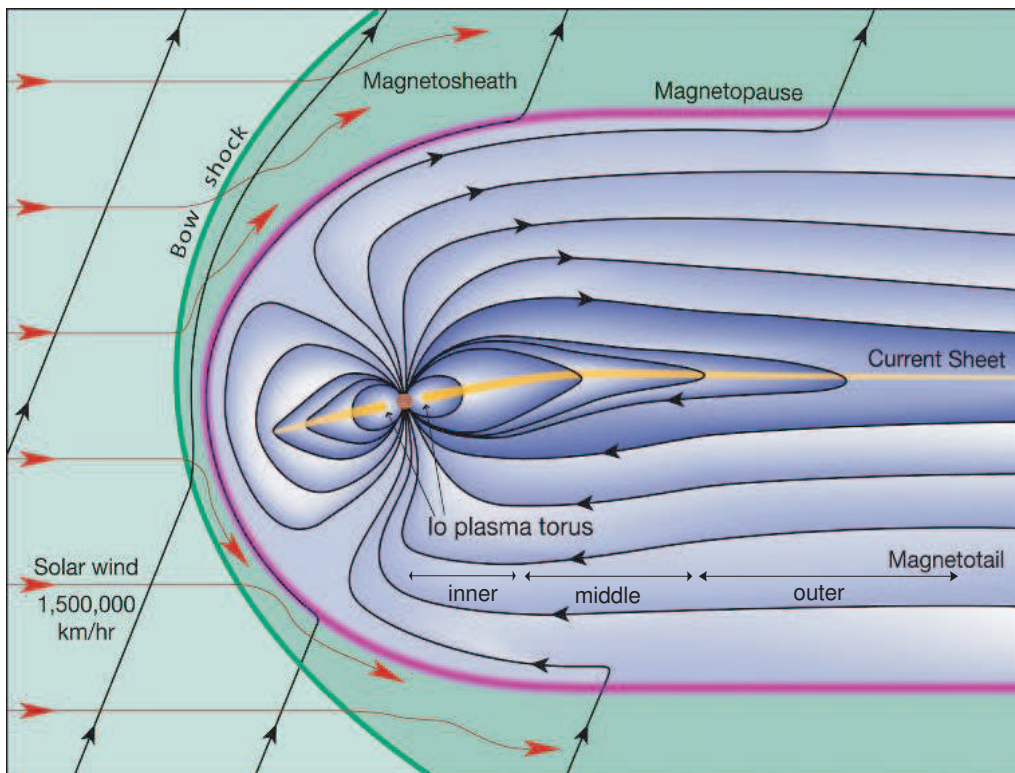


Figure 1.3: A sketch of the Jovian magnetosphere.

field becomes stretched due to the strong centrifugal and thermal pressure forces, resulting in a dominant radial magnetic field in contrast to the dipolar field in the inner region. The plasma is confined to a thin sheet around the current layer, which originates from centrifugal forces acting to maintain the trapped plasma. Both terms plasma sheet and current sheet are often used interchangeably to describe this plasma reservoir, since plasma and currents are found to be more or less at the same sheet-like region. The conducting ionosphere of Jupiter is not able to create sufficient angular momentum to the outflowing plasma and as a result the plasma corotation in Jupiter's magnetosphere gradually breaks down. The radial currents accelerate electrons into the ionosphere via the action of large field-aligned potentials, generating the main aurora (Cowley and Bunce 2001). The current sheet composes a complex structure, because the solar wind dynamic pressure, the particle thermal pressure and the centrifugal force are affecting and determining its form and location. Ulysses measurements on the dusk magnetosphere suggested a thicker plasma sheet in the dusk sector than at dawn, indicative of strong local time asymmetries.

The outer magnetosphere is extending from $40 R_J$ up to the magnetopause. Depending on the solar wind dynamic pressure the dayside magnetopause can be found anywhere from a distance of ~ 45 to $100 R_J$. The current sheet sensitive to external sources such as the solar wind direction, is expected at large distances ($r > 60 R_J$) to become parallel to the solar wind. The nightside outer magnetosphere contains an additional current system that connects the magnetodisk current to the current along the magnetopause. Because of this current the magnetic field is further stretched extending Jupiter's magnetotail beyond the orbit of Saturn.

Particle Flow

$$\text{Total} = 10 \text{ (} 10^{-4} \text{ cm}^{-3} \text{ s}^{-1}\text{)}$$

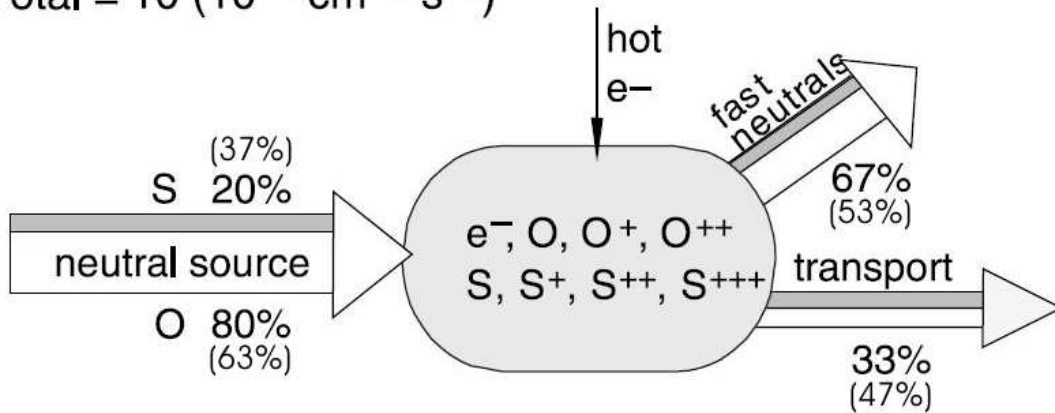


Figure 1.4: The flow of particles through the Io plasma torus consistent with a model of Voyager 1 conditions. The values in the brackets correspond to recent modifications according to Cassini observations (adapted from Delamere and Bagenal (2003) and Delamere et al. (2004)).

1.2.2 Plasma sources and transport

The primary plasma source of Jupiter is the volcanic moon Io. Already based on Pioneer measurements a large amount of particles was found close to Io (Fillius et al. 1975). Later on, Voyager 1's closest approach to Jupiter at about $5 R_J$, provided evidence of a cold corotating plasma consisting mainly of heavy ions (Warwick et al. 1979) while the active volcanism on the moon Io was for the first time discovered (Morabito et al. 1979). Io releases sulfur and oxygen in the form of SO_2 gas at a rate of ~ 1 ton/s (Hill et al. 1983). The molecules are dissociated and ionized into oxygen and sulfur ions by ionization processes and charge exchange. Mainly through electron impact ($e^- + A \rightarrow A^+ + 2e^-$) and photoionization ($A + h\nu \rightarrow A^+ + e^-$) an atom is converted into a positively charged ion. Through charge exchange ($A_{ECP}^+ + B \rightarrow A_{ENA} + B^+$) an energetic singly charged particle (ECP) collides with a neutral atom or molecule and captures one of its electrons, thereby it becomes an energetic neutral atom (ENA). The major species produced are S^+ , S^{2+} , S^{3+} , O^+ and O^{2+} (Bagenal and Sullivan 1981). They populate a torus region covering a radial distance of $5.2 R_J$ to $\sim 10 R_J$. The energy of the torus charged particles is estimated to range between 20 to 30 eV for the oxygen ions and between 60 to 80 eV for the sulfur ions (Frank and Paterson 2001). Mass is lost from the system through fast neutral escape due to charge exchange and from radial transport, consistent with Voyager 1 (Delamere and Bagenal 2003) and Cassini measurements (Delamere et al. 2004) as shown in Figure 1.4. The total source rate is consistent with net plasma production of 0.5 - 1.3 tons/s. This plasma production is apparently different than the generally accepted estimate of mass addition 1 ton/s and indicative for strong variations in the neutral source (Delamere et al. 2004). The observed composition of the torus requires the ratio of oxygen

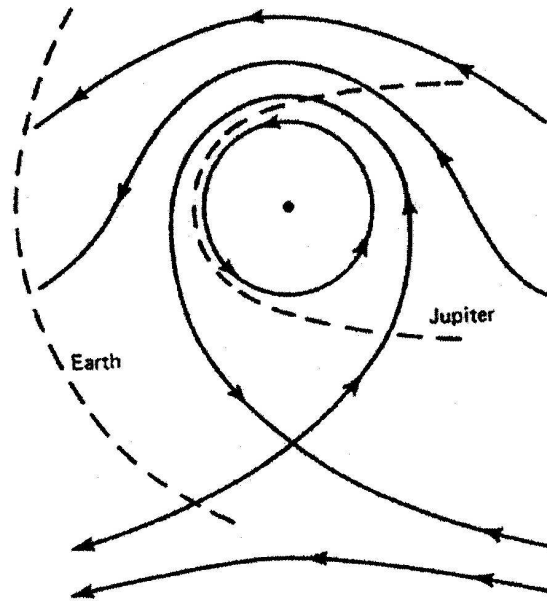


Figure 1.5: A schematic representation of the convection-corotation equipotentials (solid lines). The approximate magnetopause locations at Earth and Jupiter are shown by the dashed lines (from Cheng and Krimigis (1989)).

to sulfur neutrals to be greater than the expected value of 2, which would result from the dissociation of SO_2 . This is mainly because of the efficiency of the $O + O^+ \rightarrow O^+ + O^*$ charge exchange reaction, which preferentially removes oxygen neutrals from the system. A source strength O/S ratio of 4 is required to produce the ion composition that is consistent with Voyager 1 era measurements (Delamere and Bagenal 2003). However, Cassini measurements showed that this ratio can change to 1.7 (Delamere et al. 2004) indicative of large temporal variations of the Io emissions. In addition to the main species a number of minor species are detected in the torus such as SO^+ , SO_2^+ , Na^+ (Bagenal and Sullivan 1981) and Cl^+ , Cl^{2+} (Küppers and Schneider 2000, Feldman et al. 2001) but each of them contributed only a small percentage $< 5\%$ of the main total ion content. The newly created thermal ions (up to a few hundred eV) are picked up by the ambient electric field and are accelerated to the bulk plasma corotational flow speed near Io with a relative velocity of 57 km/s. By acceleration processes that will be discussed in the section 1.3 the thermal ions gain energies up to the MeV range.

While Io is the main internal plasma source, solar wind is the main external source. It provides the Jovian magnetosphere with helium and protons. It is estimated that the solar wind source amounts to less than 100 kg/s (Hill et al. 1983), significantly lower than the Io contribution. However the number density of protons may be comparable to the iogenic plasma number density in the regions where the solar wind accesses the magnetosphere, such as the middle and outer magnetosphere. He^{2+} is the best indicator of the presence of the solar wind (Geiss et al. 1992). It is not expected a significant amount

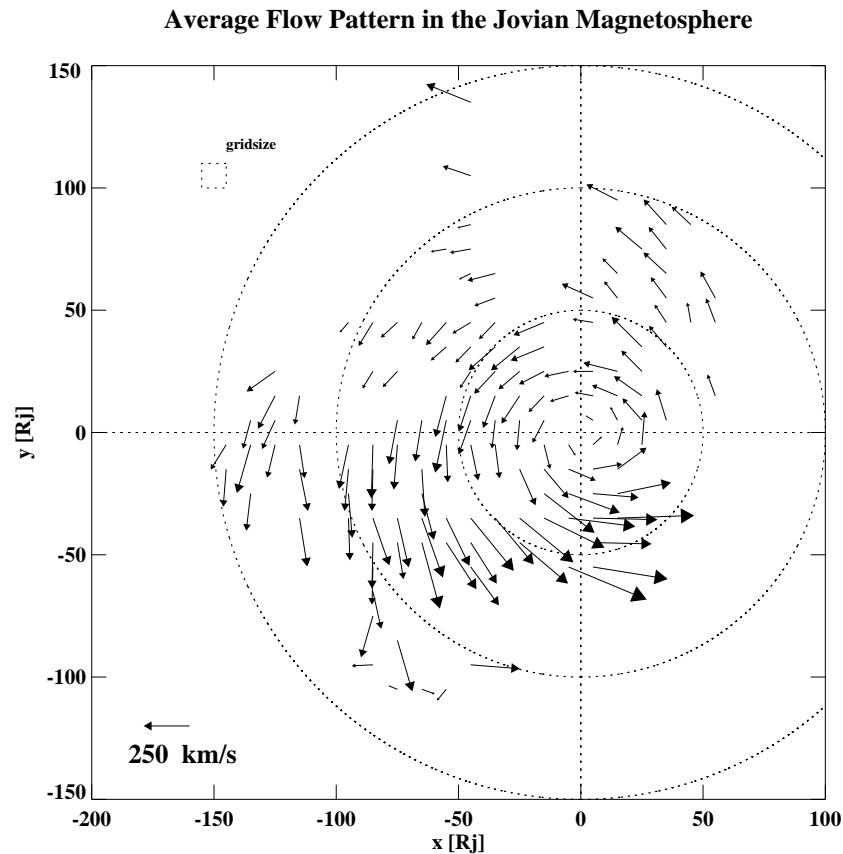


Figure 1.6: A global strongly averaged view of the flow pattern in the equatorial plane of the Jovian magnetosphere derived by Galileo EPD measurements during the time period 1995 - 2002. The ion flow values are binned into $10 \times 10 R_J$ grid and then averaged (from Woch et al. (2004)).

of this ion to come from the ionosphere of Jupiter, because its progenitor He^+ is relatively low primarily due to reactions with H_2 ($He^+ + H_2 \rightarrow H^+ + H + He$ and $He^+ + H_2 \rightarrow H_2^+ + He$). Charge discriminative instruments confirmed this (Geiss et al. 1992, Mall et al. 1993) and established helium ion as the tracer of the solar wind. Protons, however have a multiple origin other than the solar wind.

The next significant source of magnetospheric plasma is Jupiter's ionosphere. Mainly energetic H^+ , H_2^+ and H_3^+ are added to the magnetosphere through the ionospheric source. Molecules of H_2^+ and H_3^+ , produced in the upper ionosphere by energetic particle precipitation, are locally accelerated by parallel electric fields and/or resonant and non-resonant particle-wave interactions (Hamilton et al. 1980). The Jovian ionosphere, in contrast to the Earth's, is not considered a major source of plasma for the Jovian magnetosphere and its source strength is estimated to be around ~ 20 kg/s.

The icy satellite Europa is considered as a rather weak source of oxygen ions (Bagenal et al. 1992, Schreier et al. 1993). Oxygen ions are removed from its surface through sputtering by iogenic matter and is added to the magnetosphere. Europa's contribution to the magnetospheric plasma is smaller compared to that of Io, however, has an effect on the local plasma composition. In addition, the Europa neutral gas torus is an additional

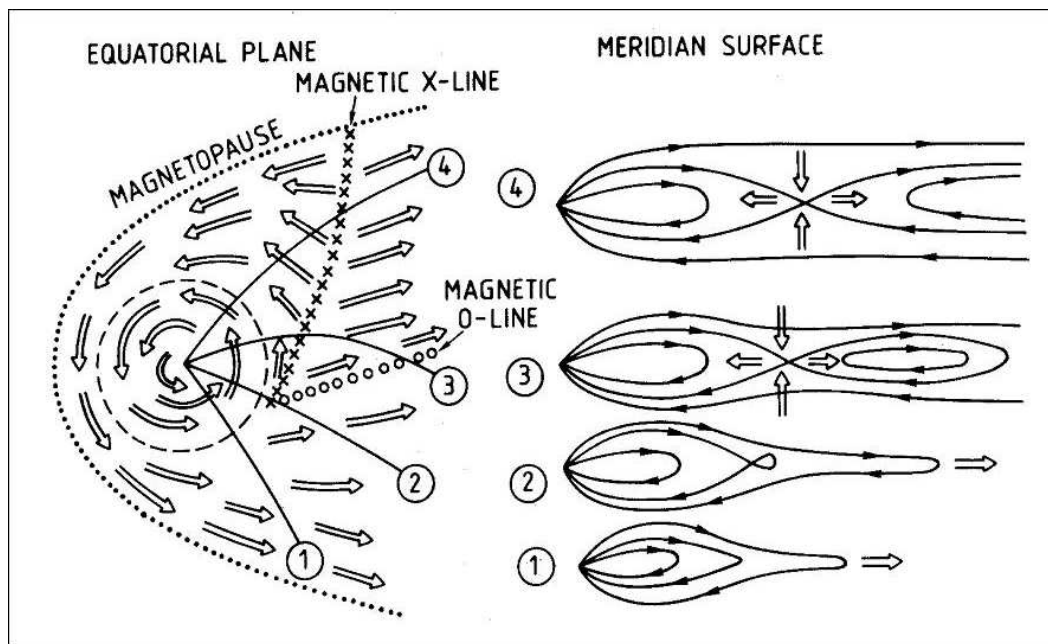


Figure 1.7: Schematic representation of the plasma flow in the equatorial plane together with the associated magnetic field and plasma flow in the meridian plane along cuts 1-4 shown on the left (from Vasyliūnas (1983)).

source of Energetic Neutral Atoms (ENA) (Mauk et al. 2003) and a sink of energetic protons (Lagg et al. 2003). In general the three icy Galilean satellites Europa, Ganymede and Callisto provide an additional but less significant source of plasma of the Jovian magnetosphere. Since sputtering has removed the light elements only heavy ions are on their surfaces which are difficult to sputter. The total pick up plasma from these satellites is estimated to be less than 20 kg/s (Cooper et al. 2001).

Ultimately, the plasma generated by Io must escape so that the plasma losses balance the sources. The plasma is accelerated to roughly the corotation speed of Jupiter. However, corotation alone cannot remove plasma from the magnetosphere, which led to the suggestion that the accumulated plasma is transported outward by the interchange instability driven by centrifugal forces (Ioannidis and Brice 1971). Beyond a certain distance known as the Hill corotation radius R_H (between 15 and 30 R_J), the corotation breaks down (Hill 1979).

The influence of the solar wind on the plasma flow is described by the tear drop equipotential pattern shown in Figure 1.5 (Cheng and Krimigis 1989). The circles near the planet show the region that is dominated by the corotation, while the open curves describe the region dominated by the sunward convection. The last closed equipotential, the separatrix (teardrop), divides the corotating flow in the plasmasphere from the convecting plasma. At Earth, also shown in the figure, the separatrix is located at ~ 0.6 times the dayside magnetosphere. However, at Jupiter this separatrix is expected to lie well beyond the dayside magnetosphere. This corotation-convection model was used to explain the composition profiles observed on the Voyager 2 outbound trajectory as will be presented in section 1.4.

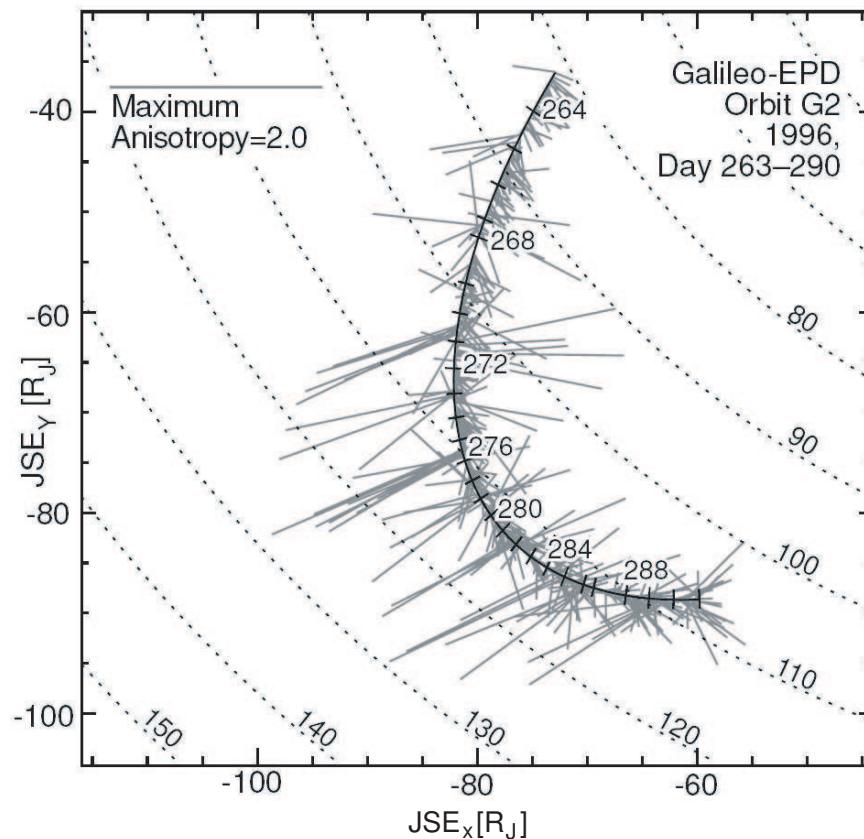


Figure 1.8: First order anisotropy vectors of protons (80-220 keV) projected on the equatorial plane along the Galileo orbit G2 near the apojoVe at radial distances of 80 - 130 R_J (from Krupp et al. (1998)).

Observations by the Galileo instrumentation provided a global characterization of the plasma flow in the Jovian magnetosphere (Krupp et al. 2001). Under the assumption that directional anisotropies are produced predominantly by convective flow, global maps of ion velocity vectors in the Jovian equatorial plane are derived as shown in Figure 1.6. The ions appear to corotate in the dawn-noon quadrant and significantly subcorotate in the noon-dusk sector. The existence of clear asymmetries between dawn and dusk sectors, as well as the evidence of radial motion also in the outer magnetosphere compose a complex interaction between a rotationally dominated system and the solar wind.

A sketch of the expected flow pattern of the Jovian magnetosphere associated with topological changes in the magnetotail is shown in Figure 1.7 (Vasyliūnas 1983). It was suggested that a flow transition to a planetary wind outflow might occur via a reconnection process involving the formation of an x-line. Heavily mass-loaded magnetic flux tubes become stretched as they rotate, resulting in spontaneous reconnection and the release of plasmoids downtail. Bursty flow is directed away and also towards the planet.

Energetic particle observations confirmed the theoretical predictions of magnetic reconnection line formation in the Jovian magnetotail mainly because of internal processes. Quasi-periodic energetic particle bursts occur in the magnetotail region (Krupp et al. 1998, Woch et al. 2002, Kronberg et al. 2005). These reconfiguration processes are character-

ized by strong radial flow anisotropies, changes in the energy spectra of energetic particles, polarity changes in the magnetic field north-south component and their correlation with radio emissions (Louarn et al. 1998). As it is shown in Chapter 3 during the burst events also the heavy ion composition is changed. An example of flow bursts occurring every 2.5-3 days is shown in figure 1.8 (Krupp et al. 1998). The example is from the predawn Jovian magnetotail, where most of these events are observed.

1.3 Particle acceleration and ion energy spectra

Ions that are injected into the magnetosphere of Jupiter are initially accelerated up to twice the local corotation velocity of 57 km/sec close to their source Io. However, those particles are later on accelerated to energies much larger than the local corotation velocity by various mechanisms. The acceleration mechanisms are sorted out by the way they violate the three adiabatic invariants of the particle motion into adiabatic, quasiadiabatic and nonadiabatic processes (Hill et al. 1983).

The adiabatic invariants are quantities related to the charged particle motion in a magnetosphere: the gyromotion around the field line, the bounce motion along the field line between mirror points and the drift motion around the planet as shown in Figure 1.9.

The gyromotion describes a circular motion around the field line, with a gyroradius of:

$$|R_L| = \frac{p_{\perp}}{qB}, \quad (1.1)$$

where q is the particle charge, B is the magnetic field magnitude and p_{\perp} is the momentum perpendicular to the magnetic field.

If during the particle's gyro period the magnetic field changes are small then the magnetic moment μ of the particle remains constant. This invariant is known as the first adiabatic invariant and is normally expressed by:

$$\mu = \frac{p_{\perp}^2}{2mB} = \frac{W_{\perp}}{B} = \frac{W \sin^2 \alpha}{B}, \quad (1.2)$$

where m is the particle's mass, W_{\perp} its kinetic energy and α the pitch angle of the particle.

If changes in the magnetic field are small over the time of one bounce period, the second invariant J_B is derived. J_B is the integral of the particle's momentum along the field line, between the mirror points:

$$J_B = 2 \int_{S_m}^{S'_m} p_{\parallel} ds = 2mlu_{\parallel}, \quad (1.3)$$

where p_{\parallel} and u_{\parallel} are the particle's momentum and velocity parallel to the magnetic field, m the particle's mass, S_m and S'_m are the mirror points and l the total length of the field line between the two mirror points.

The particles drift longitudinally around the planet. Considering that over a drift period the magnetic field is not changing, then a third constant of motion is derived, known as the third adiabatic invariant:

$$\Phi = \oint B ds, \quad (1.4)$$

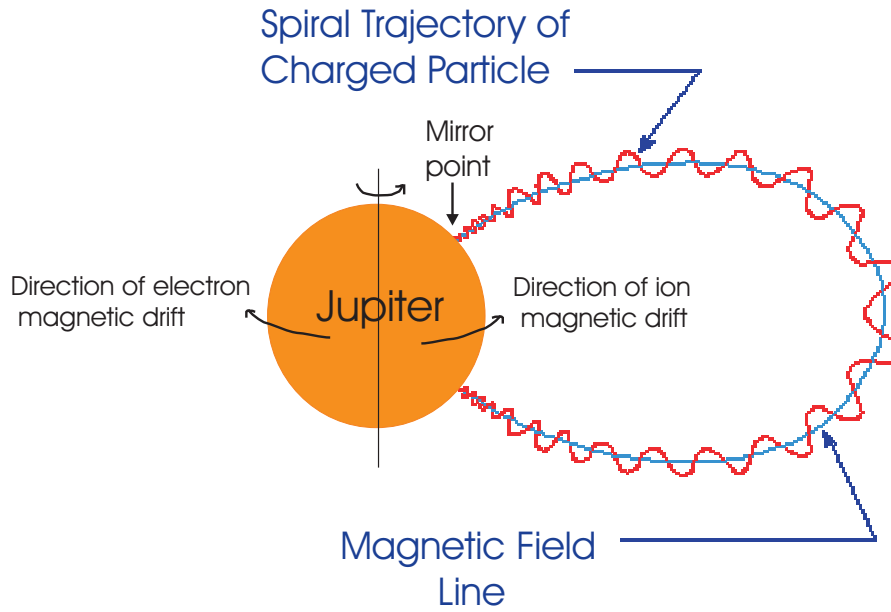


Figure 1.9: Trajectory of trapped particles showing gyromotion around the field line, bounce motion along the field line between mirror points and drift motion around the planet (adapted from Walt et al. (1994)).

where Φ is the magnetic flux enclosed by the drift path ds , and B the magnetic field magnitude.

As adiabatic processes are described those during which the particle is transported inward through violation of the third invariant while adiabatic compression is produced by the conservation of the first and second invariants. Conservation of the first invariant has an important effect when the particles drift across the field lines. When a particle moves along its drift path from a region of magnetic field strength B_1 into a region of increasing field strength B_2 the conservation of the magnetic moment from equation (1.2) gives:

$$\frac{W_{\perp 2}}{W_{\perp 1}} = \frac{B_2}{B_1}, \quad (1.5)$$

which results in $W_{\perp 2} > W_{\perp 1}$. The perpendicular energy of the particle is increased, and the parallel remains constant. This type of energization of the particle is called adiabatic heating and is some kind of betatron acceleration.

The conservation of the second invariant implies that the parallel energy of the particle will also change during the combined drift and bounce motion of the particle along and across the field. During the particle's drift motion from weaker into stronger fields, the particle necessarily moves from one field line of length l_1 to another of length l_2 . Simultaneously its average parallel velocity changes from $u_{\parallel 1}$ to $u_{\parallel 2}$. Equation (1.3) gives:

$$\frac{W_{\parallel 2}}{W_{\parallel 1}} = \frac{l_1^2}{l_2^2}. \quad (1.6)$$

If the length of the field line which corresponds to the bounce motion decreases, $l_1 > l_2$ then the parallel energy of the particle increases $W_{\parallel 2} > W_{\parallel 1}$. This is the principle of the Fermi acceleration.

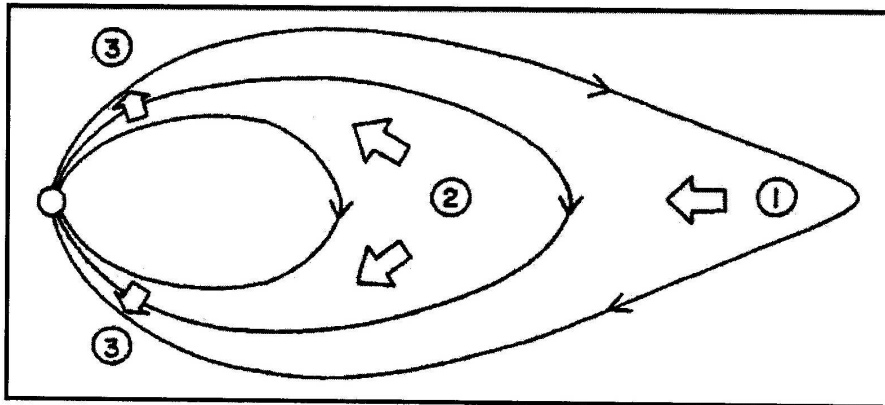


Figure 1.10: Multiple diffusion process as proposed by Nishida (1976). The three different stages are marked (from Nishida (1976)).

Another category of acceleration processes are the quasiadiabatic processes. They are characterised by alternating repetition of adiabatic compression and nonadiabatic scattering. Nishida (1976) proposed a model of multiple diffusion processes, shown in Figure 1.10. From step 1 to 2 inward diffusion takes place and the conservation of the first adiabatic invariant increases W_{\perp} . At step 2 pitch angle scattering occurs and particles are moved to lower altitudes. Finally at step 3 the particles are diffused across field lines conserving only the first adiabatic invariant and reach point 1 with large field-aligned velocities. To this model an additional pitch angle scattering is added at step 1 (Sentman et al. 1975). By this way the field-aligned energy is partially converted to cyclotron energy. The particles gain much higher energies by repeating the cycle many times. However, during a cycle the particle has the same possibility to lose or gain energy and as a result only a small percentage of the initial population gains high energies. Fujimoto and Nishida (1990) considering the recirculation model (Nishida 1976, Sentman et al. 1975) included a fourth step of pitch angle scattering in the current sheet and confirmed it by Monte Carlo simulations. Another model involving quasiadiabatic processes is based on the day-night side asymmetry of the magnetic field (Goertz 1978). The strength of the magnetic field is stronger in the dayside and weaker in the nightside at a given distance, due to compressed magnetic field lines on the day side and a stretched configuration in the tail. The model predicts that a particle drifting from noon to midnight suffers betatron deceleration and from midnight to noon betatron acceleration. By the first process W_{\perp} is decreased and by the second it is increased (equation 1.5).

The nonadiabatic processes require the violation of the first and second invariants as a necessary condition for the acceleration itself. Magnetic merging or reconnection is one of the nonadiabatic processes, responsible for particle acceleration in a magnetosphere. During this process the magnetic field energy is converted into particle energy in a region of reverse magnetic field (Vasyliūnas 1975). Another nonadiabatic mechanism is acceleration by parallel electric fields and is essential for the aurora regions. Nonadiabatic particle acceleration can also be obtained by wave-particle heating. Resonant wave-particle interactions result in energy transfer between plasma waves and the energetic particle

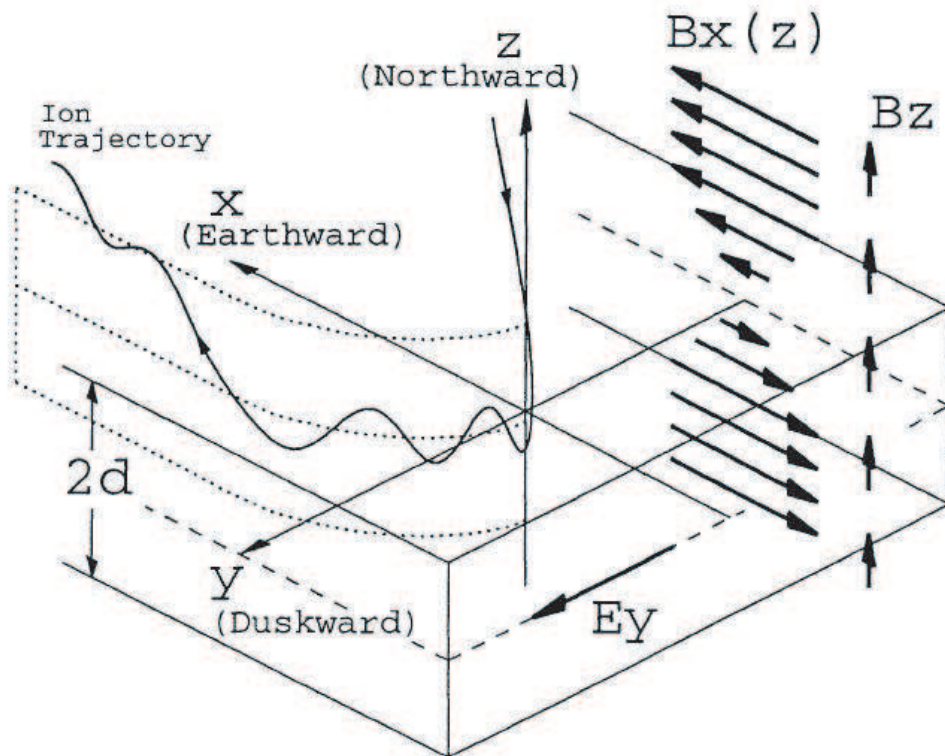


Figure 1.11: A schematic representation of the 'Speiser' orbits for protons and electrons for the magnetosphere of the Earth. Adapted from Speiser (1965).

population.

Nonadiabatic particle motions occur also by the interaction of energetic ions entering the current sheet (Speiser 1965). The particle motion is examined in a simplified model shown in Figure 1.11 for electrons and protons in the magnetosphere of Earth. The current sheet has a width of $2d$. The dawn to dusk electric field is described by $\mathbf{E} = E_y \hat{y}$, where the E_y is constant and the magnetic field is given by $\mathbf{B} = B_x \hat{x} + B_z \hat{z}$. The B_x is assumed to be constant at $|z| > d$ and decrease linearly ($B_x \propto z$) at $|z| \leq d$ while the northward component of the magnetic field B_z is constant. Away from the current sheet the particles are gyrating along the magnetic field lines executing adiabatic motion. The particle is accelerated by the current sheet only if the spatial scale of the magnetic field change is less than a particle gyro radius so as the first adiabatic invariant is no longer conserved in the vicinity of the current sheet. Thus, the requirement for a non adiabatic particle interaction with the current sheet is that the particle's gyro radius becomes comparable or greater than the minimum curvature radius of the field lines, $r_g \geq R_c$ (Cheng 1990, 1992). The curvature of radius R_c is related to the curvature force (magnetic tension) and it is estimated by the Goertz (1976) model to vary between 1 to $0.02 R_J$ for radial distance of 10 to $140 R_J$.

A proton (for electron the signs are opposite) entering the current sheet starts to oscillate about the $z=0$ plane and moves towards dusk, accelerated by the dawn to dusk electric field E_y . Since the B_z component is non-zero the ion is diverted toward the Earth and finally ejected from the current sheet. Such trajectories are called 'Speiser orbits' and

are shown in a schematic representation in Figure 1.11 for electrons and protons in the magnetosphere of Earth. The time of the ejection $\tau_{ej} \propto \frac{m}{qB_z}$ and the distance the particles drift is $x \propto \frac{mE_y}{qB_z^2}$. Thus protons drift further and are ejected from the neutral sheet much later than electrons. The velocity of the ejected particles ($\frac{x}{\tau_{ej}}$) is $u_{ej} \propto \frac{E_y}{B_z}$ and independent of the $\frac{m}{q}$ (Speiser 1965). Cheng (1990) has shown that this nonadiabatic interaction with Jupiter's rotating current sheet can energize heavy ions up to hundreds of keV. Later on in this thesis, ion composition changes in the Jovian magnetotail are discussed in terms of this nonadiabatic interaction of particles with the current sheet.

An accurate measurement of the ion energy spectrum provides information about the source of the particles and any dynamical processes that have intervened from the time the particle is injected until the detection. The ion energy spectral shapes are a useful tool to investigate the acceleration processes for the ion species. Particle energy spectra in planetary magnetospheres are often characterised by kappa distributions (Lorentzian distributions) originally introduced by Vasyliūnas (1971). They are defined as having Maxwellian shapes at lower energies ($E \exp[-E/kT]$) and power law shapes ($E^{-\gamma}$) at higher energies. Figure 1.12 shows an example of the ion energy spectra measured by Voyager 2 (LECP) in the outer magnetosphere of Jupiter (Krimigis 1981, Kane 1991). The kappa distribution which fits the data consists of a Maxwellian distribution with temperature $kT = 28$ keV and of a power law with $\gamma = 3$.

The Galileo energetic particle instrumentation provided more detailed measurements at the high energy part of the spectra leading to the conclusion that a kappa distribution cannot sufficiently describe the ion energy spectra in the Jovian magnetosphere. Instead, the spectral slope has an additional break at higher energies (Mauk et al. 1996, 1998, Radioti et al. 2005).

The ion energy spectrum for a given ion species can be described by the following equation (Mauk et al. 1998):

$$I = C \frac{E[E + kT(1 + \gamma_1)]^{-1-\gamma_1}}{1 + (E/et)^{\gamma_2}}, \quad (1.7)$$

where I is the differential intensity ($cm^{-2}s^{-1}sr^{-1}keV^{-1}nuc$), E is the energy (keV/nuc), γ_1 and γ_2 are the spectral indices, before and after the change in the spectra and C , kT and et are additional fitting parameters. The numerator of (1.7) is equivalent to the kappa distribution. The denominator describes the additional break, so as at very high energies the spectrum has a power law shape with spectral index $\gamma = \gamma_1 + \gamma_2$. It should be noted that equation (1.7) is a functional form of the energy spectra and is a good approximation of the measured ion fluxes vs. energy. Figure 1.13 shows an example of the ion intensity spectra for protons, oxygen and sulfur ions at $7.48 R_J$ as measured by the Galileo instrumentation. The fits are produced by model distributions based on equation (1.7) and it is clear that the ion energy spectra changes from a harder to a softer one. More detailed information about the ion energy spectra shapes for the different species and various local time and distances is part of this work and is presented later in this thesis.

The shape and the properties of the ion energy spectra in the Jovian magnetosphere were studied in terms of a nonadiabatic acceleration process based on the interaction of

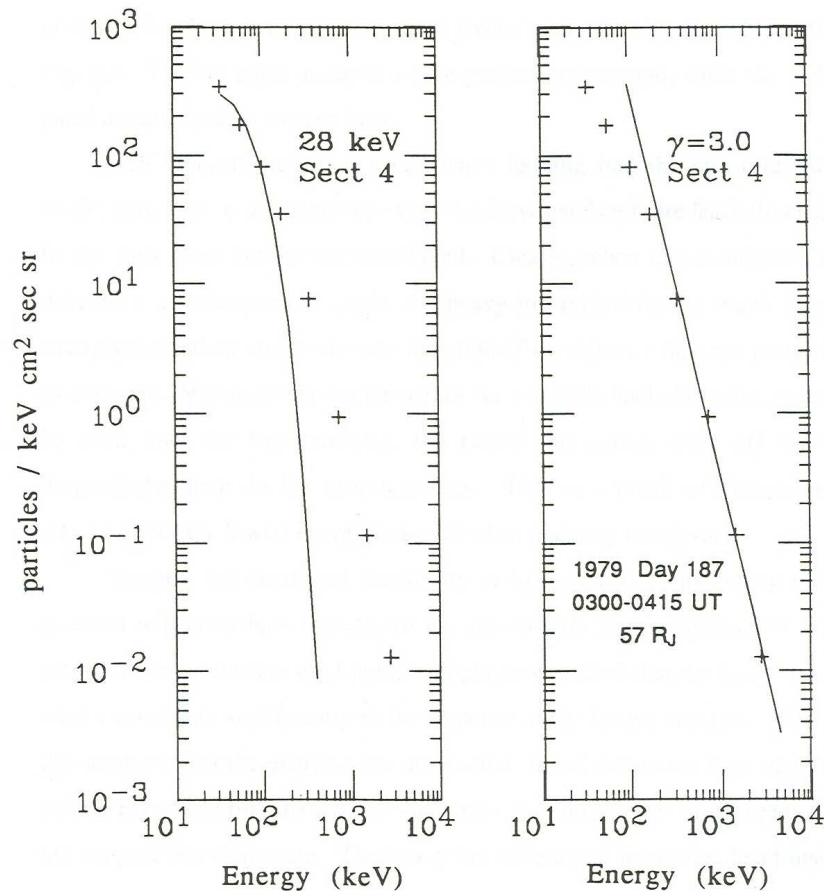


Figure 1.12: Ion intensities of protons versus energy measured by the Voyager 2 LECF instrument. A Maxwellian distribution with temperature 28 keV fits the low energy data and a power law with a spectral index of 3 fits the high energy (from Kane (1991)).

ions with Alfvén waves (Barbosa et al. 1984, Barbosa 1994). The model defined as 'ion stochastic acceleration by Alfvén waves' was initially developed to explain the production of energetic protons during solar flares (Barbosa 1979). It describes a steady state process in which the ions are interacting with intense Alfvén waves propagating along the magnetic field. The effect of the turbulence is to scatter the particles in pitch angle fast enough to violate the first adiabatic invariant and isotropize the angular distribution. On a longer time scale the isotropic distribution is scattered in energy by stochastic acceleration.

Barbosa et al. (1984) used this model as a mechanism to energize ions up to several MeV in the Jovian magnetosphere. They defined the properties of the ion energy spectra in accordance with measured proton energy spectra by Voyager 1 and 2 (Mc Donald et al. 1979, Schardt et al. 1981) and related them to the power spectrum of MHD fluctuations observed by the magnetometer (Kivelson et al. 1976). Barbosa (1994) merged the non-adiabatic model of ion stochastic acceleration by Alfvén waves with the standard radial diffusion model, where both the first and second adiabatic invariants are conserved. By

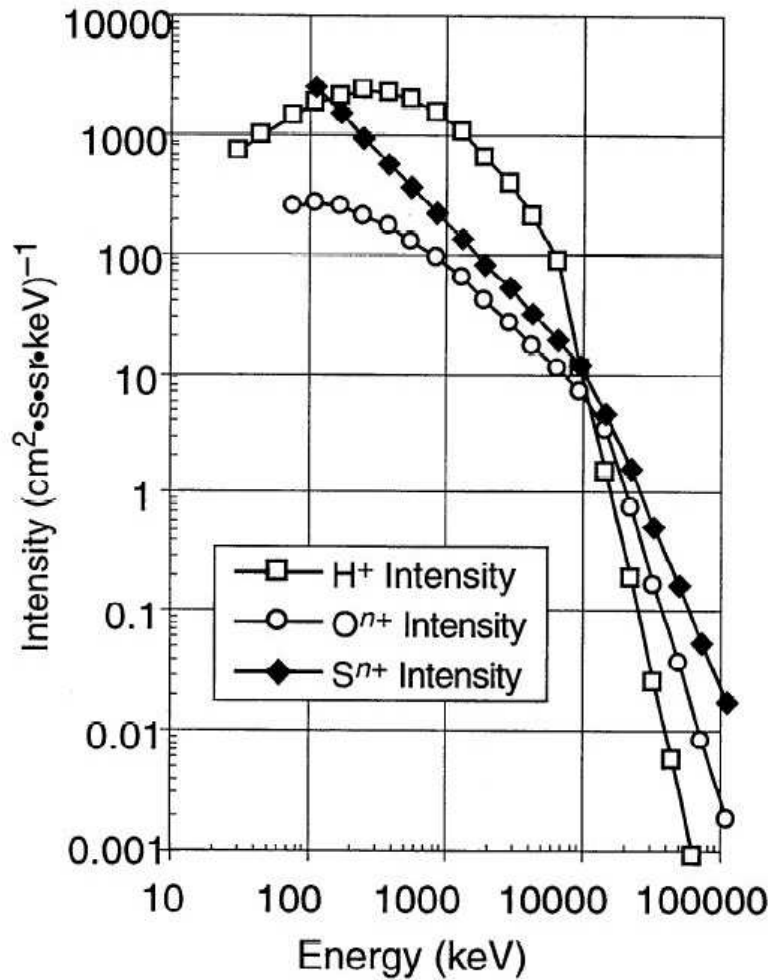


Figure 1.13: Ion intensity spectra derived by the Galileo data (EPD) at $7.48 R_J$. The fits are derived by model distributions based on equation (1.7) (from Mauk et al. (1998)).

this combined model he explained the observed ion energy spectra shapes as measured by the Voyager LECP data in the energy range of 10 - 1000 keV (Kane 1991) for various radial distances from the planet. The author assumed that singly ionized S^+ and O^+ ions are injected by the magnetospheric neutral wind and obtain their initial energy according to the local corotation energy while the protons are monoenergetic and injected from an ionospheric source. By this model they reproduced very well the features of the power law behaviour at high energies and the roll over to the Maxwellian at low energies for various radial distances.

The model of ion stochastic acceleration by Alfvén waves is discussed later on in this thesis as a possible physical explanation to the observed ion energy spectra and especially to the high energy part as derived by the Galileo instrumentation (Figure 1.13, equation 1.7). The application of the model to the data at various distances together with the properties of the Alfvén waves and parameters characterising the ion population are discussed in Chapter 4.

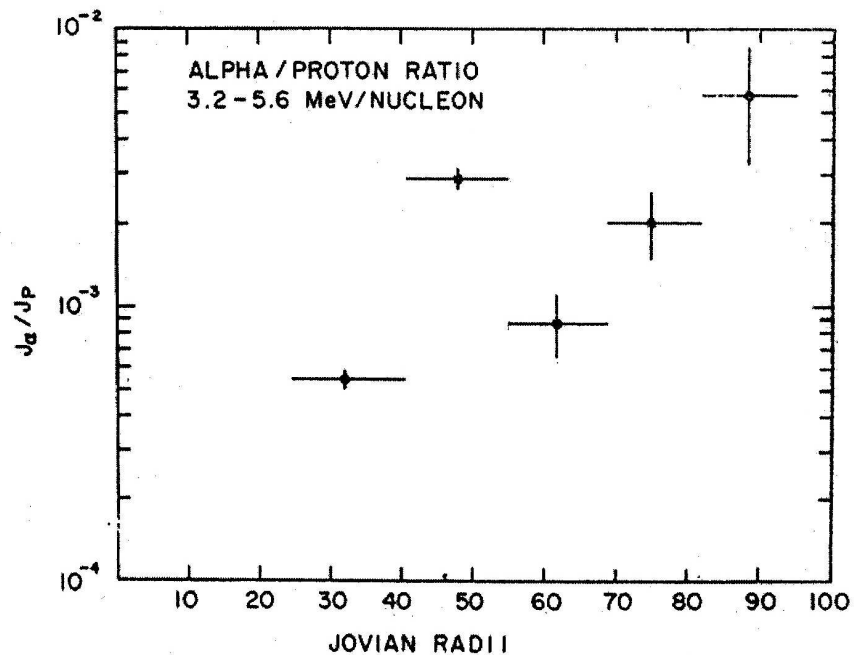


Figure 1.14: p/He flux ratio at the energy interval of 3.2-5.6 MeV/nuc as a function of the radial distance along the Pioneer 10 inbound trajectory (from Trainor et al. (1974)).

1.4 Ion abundances of the Jovian magnetosphere

The study of the ion composition of the magnetosphere of Jupiter contributes to the identification of the various plasma sources and sinks. An overview of the plasma sources and sinks has already been given in a previous section. Moreover the investigation of ion abundances throughout the Jovian magnetosphere at different radial distances and various local time sectors helps to understand better the transport processes and the dynamics in the Jovian system. Comparison of the results of various missions in different energy ranges could lead also to the identification of various particle acceleration mechanisms. An overview of the investigation of the ion abundances as it has been derived through the missions is necessary before presenting the composition results of this thesis.

The ion composition has been normally studied by comparing the particle intensities of two species at a given reference parameter (proxy). The most common proxy chosen is the energy/nucleon (fixed velocity). Most of the current knowledge about the heavy ions in the Jovian magnetosphere has been gained by the energetic particle instruments onboard Voyager, Ulysses, Galileo and Cassini, which were able to detect heavy ions directly. Charge state measurements though were only obtained by few experiments onboard the spacecraft.

The first in situ measurements of energetic ions in the magnetosphere of Jupiter were provided by Pioneer 10 and 11, respectively. However, the measurements were limited in energy and especially in species coverage and no three-dimensional distributions could be obtained. By the experiments onboard Pioneer protons and helium ions could be identified in situ. First determinations of the relative ion abundance ratios of p/He at various

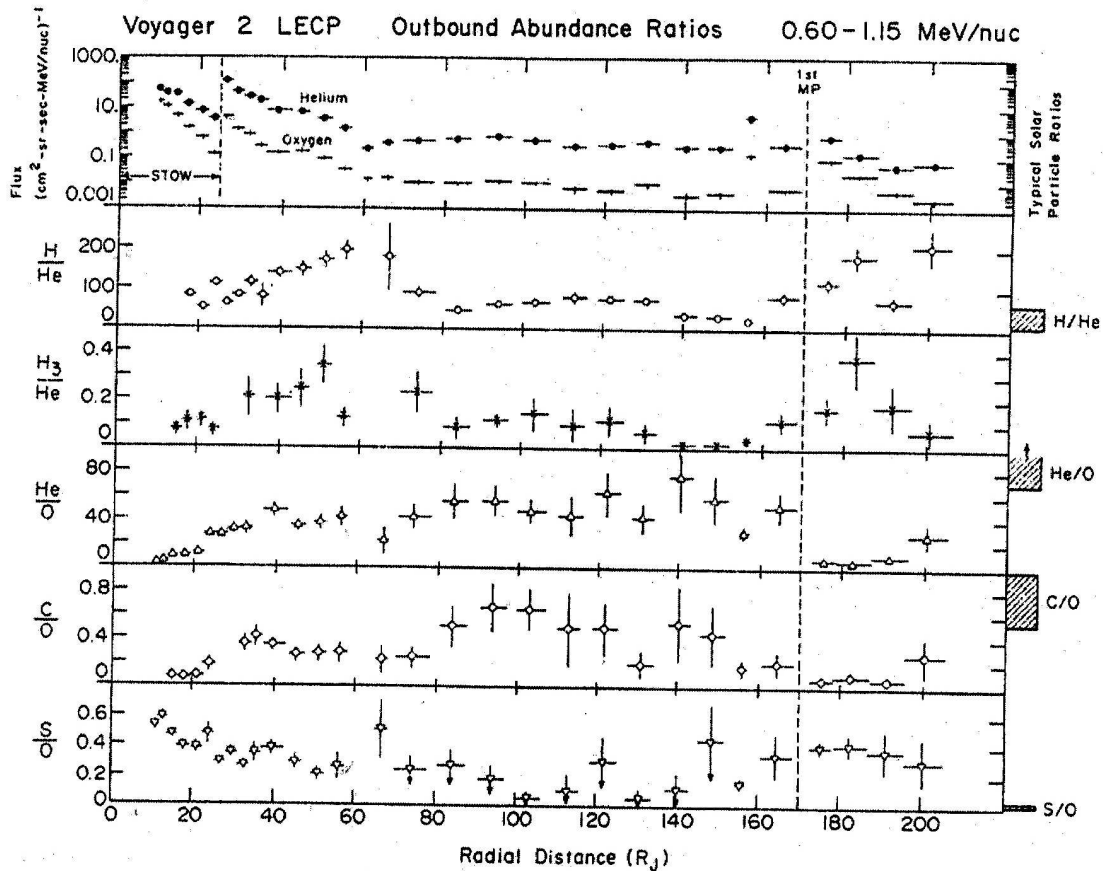


Figure 1.15: Relative ion abundance ratios of p/He (H/He), H_3/He , He/O, C/O and S/O, together with helium and oxygen intensities at the energy range of 0.6 - 1.15 MeV/nuc plotted versus the radial distance during the outbound pass of Voyager 2 (from Hamilton et al. (1981)).

energy/nucleon ranges were obtained during the pass of Pioneer 10 in the pre-noon local time sector. Figure 1.14 shows the He/p flux ratio as a function of radial distance calculated at the energy interval of 3.2-5.6 MeV/nuc along the inbound trajectory of Pioneer 10 (Trainor et al. 1974). The same flux ratio at lower energies of 1 MeV/nuc during the inbound (40-24 R_J and 24-15 R_J) and outbound (13.6-19.2 R_J) pass of the same spacecraft and instrument gave values higher by an order of magnitude (Simpson et al. 1974b), indicative of an energy/nuc dependence of the He/p ratio.

Voyager 1 and 2 instrumentation provided a more detailed mass resolution of energetic ions. Apart from the light elements, heavy ions such as sulfur, oxygen, carbon and sodium were measured (Krimigis et al. 1979a,b, Hamilton et al. 1981). However, the measurements were restricted by the instrument's scan plane which was nearly parallel to Jupiter's equatorial plane. The importance of the ionospheric source was established by the discovery of H_2^+ and H_3^+ molecules (Hamilton et al. 1980). Various relative ion abundance ratios were calculated at a specific energy/nucleon range (0.6 - 1.15 MeV/nuc) along the spacecraft trajectory (Hamilton et al. 1981) shown in Figure 1.15 up to 200 R_J

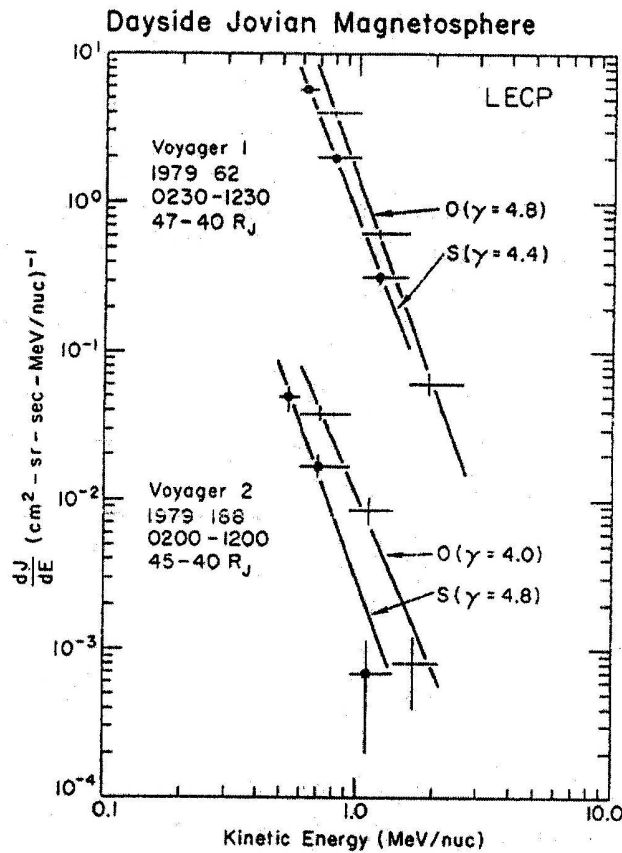


Figure 1.16: Oxygen and sulfur energy spectra during the Voyager 1 and 2 inbound trajectory, compared at the same radial distance (from Hamilton et al. (1981)).

from the planet. Part of these results are quantitatively compared later in this thesis with the abundance ratios derived onboard the Galileo spacecraft (Chapter 3). The ratios of p/He and H₃/p both increase within 60 R_J with increasing the radial distance and remain constant at a lower level beyond that distance up to the magnetopause. He/O and C/O ratios increase with distance indicating the dominance of the solar wind helium and carbon over the iogenic oxygen. The S/O-ratio ranges between 0.3 and 0.4 on average at 20 and 60 R_J . It was noted that it sporadically reached values of 0.6 beyond 60 R_J , associated with dynamical processes affecting the relative ion abundances.

Moreover sulfur and oxygen ion intensities measured onboard the consecutive missions Voyager 1 and 2 revealed discrepancies of a factor of 100. Figure 1.16 shows sulfur and oxygen energy spectra measured during the inbound trajectory of Voyager 1 and 2 at 47-40 R_J and 45-40 R_J respectively. These changes are indicative for large temporal variations. It was also noticed that the slope of the energy/nucleon spectra of various ions differ from each other and it was implied that the abundance ratios at equal energy/nucleon would vary depending on the energy at which they are evaluated (Hamilton et al. 1981). However, measurements of the p/He ratio obtained onboard Voyager 1 and 2 roughly at the same energy range showed a very good agreement (Krimigis 1983). Based on Voy-

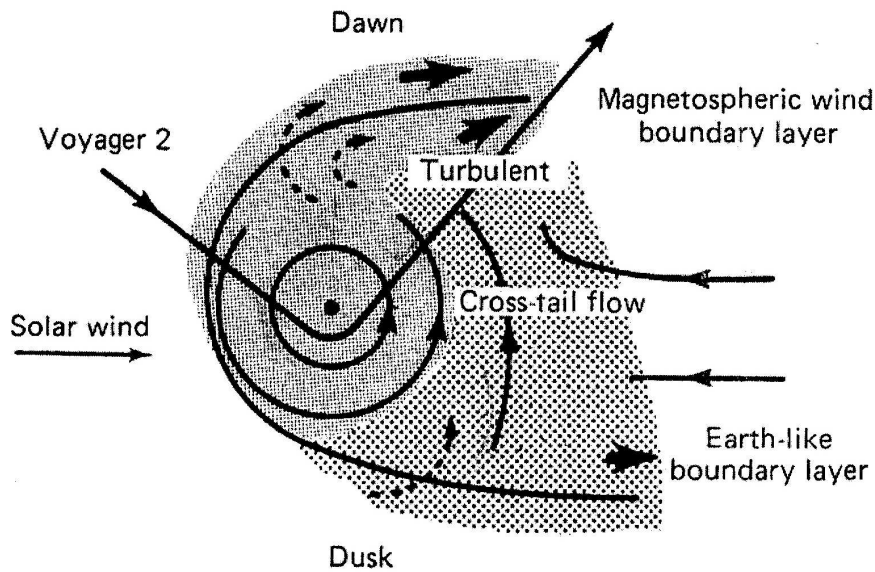


Figure 1.17: Ion composition pattern in accordance with Voyager 2 outbound observations as derived by the corotation-convection model (Section 1.2.2, (Cheng and Krimigis 1989)). The finely dotted region indicates the heavy-rich ion composition, while the sparsely dotted the more solar wind like. The Voyager 2 outbound trajectory is also shown, together with the corotation-convection equipotentials. Dashed arrows indicate the plasma transport (from Cheng and Krimigis (1989)).

ager 1 (Vogt et al. 1979a) and Voyager 2 (Vogt et al. 1979b) measurements the S/O ratio was further investigated at higher energies and closer to the planet. A dominating internal contribution of oxygen and sulfur (with Na also evident in the innermost magnetospheric region ($\leq 5.8 R_J$)) and a typical solar elemental composition at distances beyond $11 R_J$ were found (Vogt et al. 1979a).

The composition profile observed by Voyager 2 outbound was explained by the corotation - convection model by Cheng and Krimigis (1989), as shown in Figure 1.17. The finely dotted region indicates a heavy ion rich composition and the sparsely dotted region a more solar composition. According to the model at 60 to $150 R_J$ on the nightside, solar wind plasma is extracted by drift forces ($\mathbf{E} \times \mathbf{B}$) from the vicinity of the dusk magnetopause and is transported across the tail toward the dawn magnetopause. Simultaneously, the heavy ions from the Jovian plasmasphere are radially transported outward and enter the dawnside. However, latest Cassini results during the Cassini Jupiter flyby at the dusk to midnight Jovian magnetosheath question the validity of this model (Krupp et al. 2004).

Ulysses observations (Lanzerotti et al. 1993) extended these Voyager measurements spatially in the dayside plasma sheet as well as to high Jovian latitudes in the dusk magnetosphere. It was confirmed that H_2^+ and H_3^+ molecules, firstly discovered by Voyager, are accelerated out of the topside Jovian ionosphere. It was concluded that there is a solar wind component throughout the outer and middle magnetosphere, but a significant fraction of protons in the middle magnetosphere is of non-solar origin. Ion abundance ratios

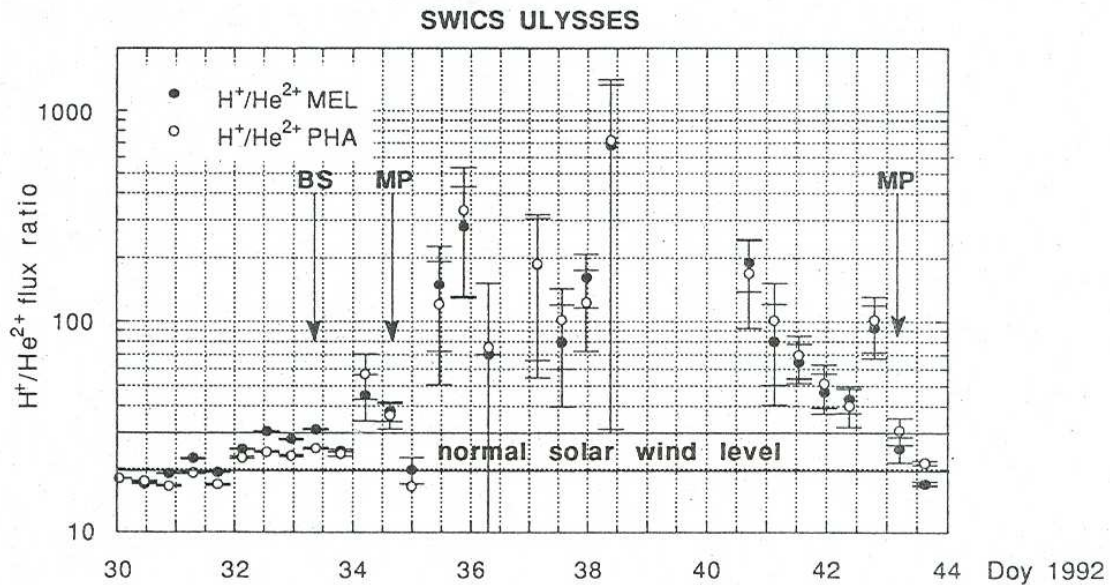


Figure 1.18: p/He^{2+} flux ratio in the Jovian magnetosphere along the Ulysses trajectory. The ratio is determined by two types of data: matrix elements (MEL) and pulse height data (PHA). BS stand for the bow shock and MP for the magnetopause crossings, while the horizontal lines indicate the solar wind level (from Mall et al. (1993)).

of sulfur and oxygen relative to helium ions were obtained for 0.5 -1.4 MeV/nucleon. It was shown that the ratios are decreased in the inner part of the magnetosphere opposite to that reported by Voyager. This behaviour was attributed to the rapid change in latitude (Lanzerotti et al. 1992). Further measurements from Ulysses confirmed the latitudinal dependence of the relative ion abundances (Krupp et al. 1999). Ulysses instrumentation provided also the first charge state measurements of ions in Jupiter's magnetosphere. It was found that at energies between 0.6 to 60 keV/e, Jovian ions, namely O^+ , O^{2+} , S^{2+} and S^{3+} , are more abundant in the inner magnetosphere while ions from the solar wind, like protons and He^{2+} , dominate in the outer region (Geiss et al. 1992). The p/He^{2+} flux ratio at the energy range of 0.6 to 60 keV/e plotted versus the radial distance is shown in Figure 1.18. It steadily increases from the solar wind level of 25 at the magnetopause ($\sim 100 R_J$) to a value of 700 at $\sim 25 R_J$ (closest approach) (Mall et al. 1993). Since the ratio is much higher than in the solar wind it was concluded that in the region from $80 R_J$ inbound to $50 R_J$ outbound most of the protons are of non-solar origin.

Results from Galileo gave new information about the global ion composition at distances from the planet between 6 and $150 R_J$. The Galileo data contain ion measurements from all local times at different radial distances over a time period of almost 8 years (1995-2003). S/O and Na/O ratios were calculated for energies between 0.5 and 1.0 MeV/nucleon during six Galileo flybys at the moon Europa (Maclennan et al. 2001). The results were in agreement with previous determinations by instruments on the Voyager and Ulysses spacecraft. It was shown that the Na/O and S/O ratios close to Europa has the tendency to decrease with increasing energy. Due to the various sources of oxygen, there is the opportunity for more oxygen to be accelerated by magnetospheric processes

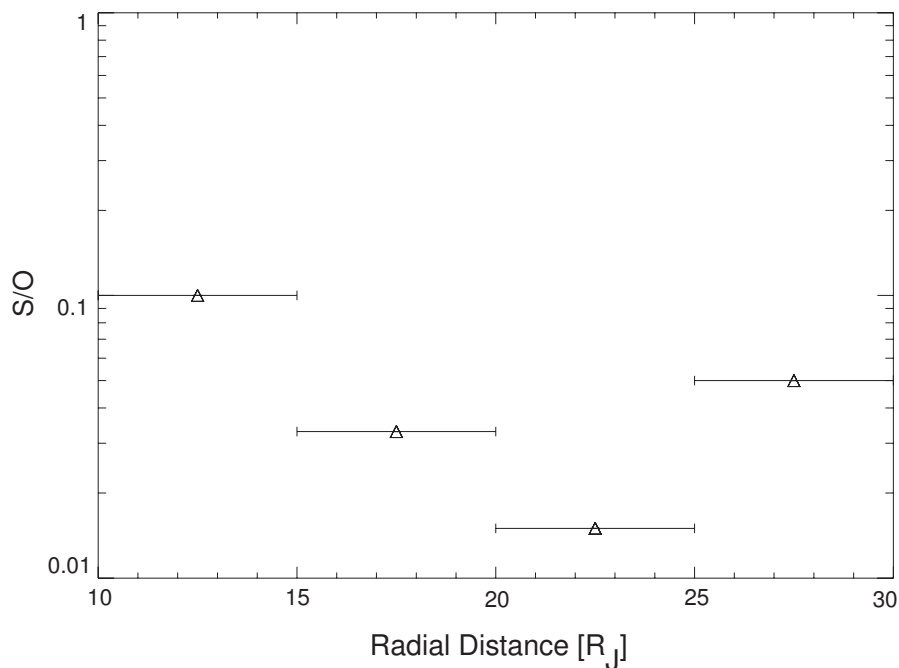


Figure 1.19: S/O abundance ratio at 4.5 to 18.4 MeV/nuc as a function of radial distance for some Galileo orbits combined (adapted from Cohen et al. (2001)).

to all energies in comparison to the fluxes from the solely iogenic origin of sodium and sulfur. Moreover, it was revealed that oxygen, sulfur and sodium fluxes all are independent on local time at least at distances of $10 R_J$ from the planet. Mauk et al. (2004) using the Galileo energetic particle dataset found that the composition of oxygen and sulfur measured at 100 to 10000 keV is changing between 7.5 to $9.5 R_J$ with sulfur to dominate over oxygen ions. The authors suggested that the heavier sulfur ions are more effectively energized than are the oxygen ions to energies larger than 50 keV/nuc.

The Heavy Ion Counter (HIC) instrument onboard Galileo enabled the study of the ion composition at the high energy range of 4.5 to 18.4 MeV/nuc (Cohen et al. 2001). The radial dependence of the intensity, energy spectrum, and composition of sulfur, oxygen and carbon indicated that solar material dominates in that energy range at radial distances between 15 to $30 R_J$ and diffuses without loss towards Jupiter, while the composition near 10 to $15 R_J$ becomes more iogenic. The O/C and S/O ratios were compared with previous results derived by Voyager 2. The comparison showed that the ratios calculated by HIC at higher energies are lower than those derived by Voyager 2 at lower energies and discussed it in terms of ion flux dependence on the magnetic moment. Figure 1.19 shows the S/O abundance ratio (derived from Fig. 5 of Cohen et al. (2001)) as a function of radial distance for some of the Galileo orbits combined. The values are substantially lower compared to those derived by Voyager 2 (Hamilton et al. 1981) at the same radial distance.

Recently, Waldrop (2004) presented a global distribution (6 to $150 R_J$) of the S/p and S/O abundance ratio at 25 keV/nuc in the Jovian equatorial plane, using Galileo data from the first 20 and 15 orbits, respectively. The S/p ratio increases with decreasing

radial distance over two orders of magnitude. The global map of the S/O abundance ratio revealed that the ratio varies throughout the magnetosphere between 0.3 and 0.8 with a minor gradual increase with decreasing radial distance. Moreover a significant increase of the S/O-ratio along the distant apojove segment of Galileo's orbit G2 (262-296 day, 1996) was observed and associated with the occurrence of intense, quasi-periodic radial bursts of accelerated plasma sheet particles (Krupp et al. 1998, Woch et al. 1999).

1.5 Summary and outline

The study of the ion composition by all previous missions to Galileo was mainly limited to a certain radial distance at a specific local time sector, while most of them were obtained at a restrained energy range. Galileo gives the unique opportunity to study the ionic composition of energetic particles on a global scale, in an extended radial distance and in a full local time coverage. The current work presents a detailed study of the ion composition in the Jovian magnetosphere based on energetic particle measurements obtained by Galileo. Global maps of various ion abundance ratios and more specific of S/O, S/He, O/He and p/He are presented, extending the previous studies of Maclennan et al. (2001), Mauk et al. (2003) and especially Waldrop (2004). Time variations and local time asymmetries, only cursorily discussed in the past are investigated in depth. The influence of the magnetospheric dynamics on the composition is studied in detail and associated ion acceleration mechanism are discussed. A comprehensive comparison with previous results for the same local time and radial distance is for first time obtained. Energy dependence effects of the ion abundance ratios are investigated, the importance of the ion energy spectra shape is derived and relevant ion acceleration mechanism are addressed.

More specific chapter 2 describes shortly the Galileo mission and the onboard instrumentation with emphasis given on the instruments used in this work. At the end of this chapter a reliability test of the Galileo energetic particle dataset is obtained, necessary for the data analysis that follows.

Chapter 3 presents the observed ion energy spectra in the magnetosphere of Jupiter followed by a detailed investigation of the ion composition based on data analysis from the Galileo Energetic Particle Detector. Relative ion abundance ratios are studied on a global scale, in an extended energy range and are compared with previous results for the same local time and radial distance. The ion composition is furthermore examined in terms of temporal and local time variations as well as along regions influenced by the magnetospheric dynamics.

Chapter 4 discusses ion acceleration mechanisms associated with the observed ion composition. Especially, the observed ion energy spectra, fundamental for the study of the ion composition, is discussed globally in terms of ion stochastic acceleration and the ion abundance ratios in the magnetotail along regions where reconfiguration events occur are examined locally by two possible acceleration processes.

2 Instrumentation used

2.1 The Galileo mission

The Galileo spacecraft, the first artificial satellite of Jupiter, was designed to study the large gaseous planet, its moons and its magnetosphere. The spacecraft was named after Galileo Galilei, the Italian scientist who discovered, in 1610, Jupiter's major moons, Io, Europa, Ganymede and Callisto.

Launched on October 18, 1989 the Galileo spacecraft made an interplanetary cruise (shown in Figure 2.1) and arrived at the giant planet six years later in December, 1995. Making close encounters to Earth (December 8, 1990 and December 8, 1992) and to Venus (February 10, 1990) it gained the necessary velocity to reach its target. This flight path provided opportunities to the scientists to study the planets, Venus, Earth and Moon as well as the asteroids Gaspra and Ida. Galileo scientists had also the chance to have a direct view of the impact region of comet shoemaker-Levy 9.

The spacecraft's instrumentation was designed to study three aspects of the Jovian system: the planet's atmosphere, the satellites and the magnetosphere. To focus on these three areas the spacecraft consisted of an atmospheric probe (Galileo Probe), a non-spinning section of the orbiter which carried imagers and other remote sensing instruments and the spinning section of the orbiter, including the fields and particles instruments designed for in situ measurements of the magnetosphere. A schematic representation of the Galileo spacecraft and its instrumentation is shown in Figure 2.2.

The Galileo probe was separated from the orbiter in July, 1995 and entered the Jovian upper atmosphere on December 7, 1995. The orbiter went into orbit around Jupiter at the same time, where it completed 35 orbits in nearly 8 years. The orbit of Galileo was especially designed to flyby at all the Galilean moons. The name of each orbit is a combination of the satellite encountered (I = Io, E = Europa, C = Callisto, G = Ganymede) and the number of the orbit. For example G2 describes the second orbit around the planet when Galileo flew by the moon Ganymede. The orbital coverage during these 35 orbits reached by Galileo was between $2.5 R_J$ (perijove of A34) and $150 R_J$ (apojove C9). On September 21, 2003 the Galileo mission ended with a controlled crash into Jupiter after a nearly 14-year odyssey in Jupiter's environment.

Investigations of Jupiter's satellites and of the Jovian magnetosphere in situ or remote were carried out by twelve experiments onboard Galileo. The four remote sensing instruments mounted on the de-spun section of the spacecraft composed the imaging and spectroscopic instrumentation. These are: the *Solid State Imaging Camera (SSI)*, the *Near Infrared Mapping Spectrometer (NIMS)*, the *Photopolarimeter/Radiometer (PPR)* and the *Ultraviolet Spectrometer/Extreme Ultraviolet Spectrometer (UVS/EUV)*.

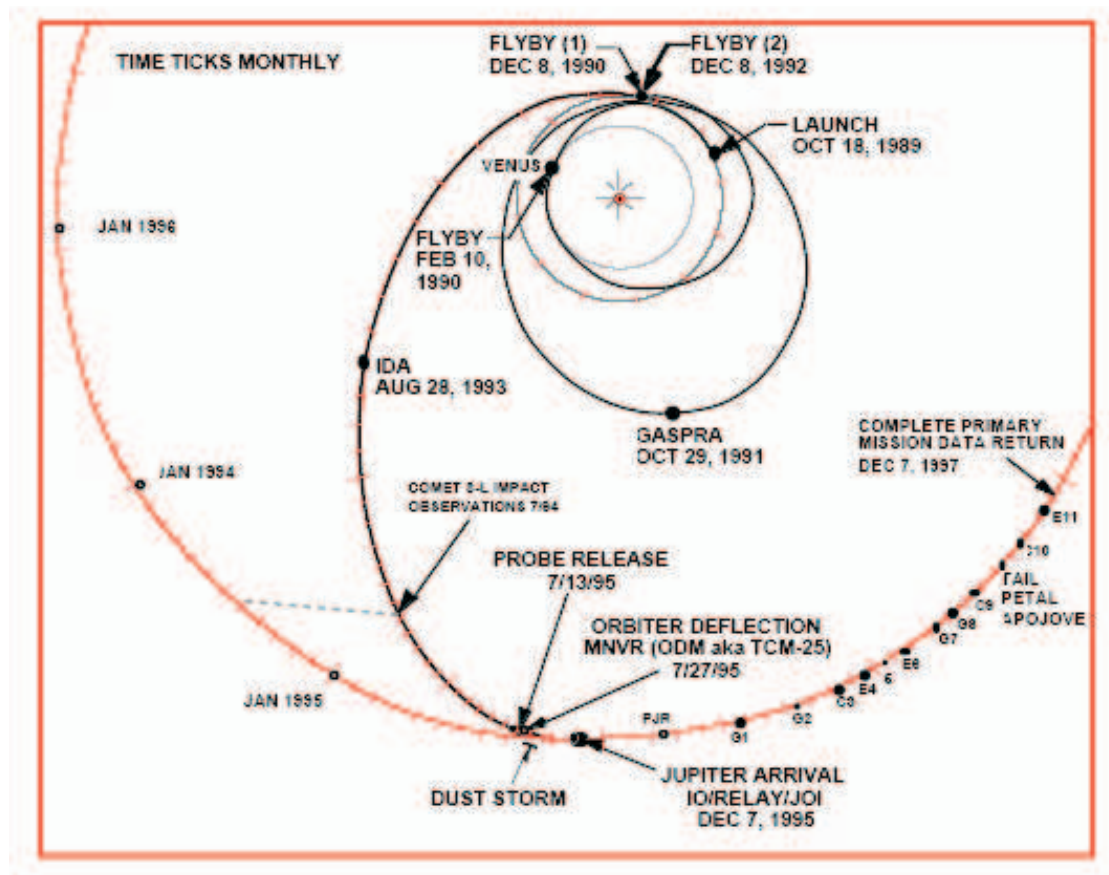


Figure 2.1: The Galileo interplanetary trajectory as seen from above Jupiter's orbital plane. Flybys at Earth and Venus as well as the asteroids Gaspra and Ida are shown.

On the spinning section of the spacecraft there were six instruments for in situ measurements of Jupiter's magnetic field, plasma waves and charged particles environment. In particular, the strength and the direction of the magnetic field were measured by the *Magnetometer (MAG)*; electrostatic and electromagnetic components of plasma waves in three dimensions were recorded by the *Plasma Wave Subsystem (PWS)*; measurements of low-energy plasma by the *Plasma Subsystem (PLS)*; the velocity, mass, charge and flight direction of the dust particles in the Jovian system were measured by the *Dust Detector Subsystem (DDS)*; data on heavy energetic particles in the inner magnetosphere were provided by the *Heavy Ion Counter (HIC)* and measurements of the energetic charged particle environment around Jupiter, which compose the primary basis of this thesis, were obtained by the *Energetic Particles Detector (EPD)*. An extensive description of the EPD instrument is provided in the next chapter.

The main scientific goals of the instruments on the Galileo orbiter are listed here:

1. Investigation of the circulation and dynamics of the Jovian atmosphere;
2. Investigation of the upper Jovian atmosphere and ionosphere;

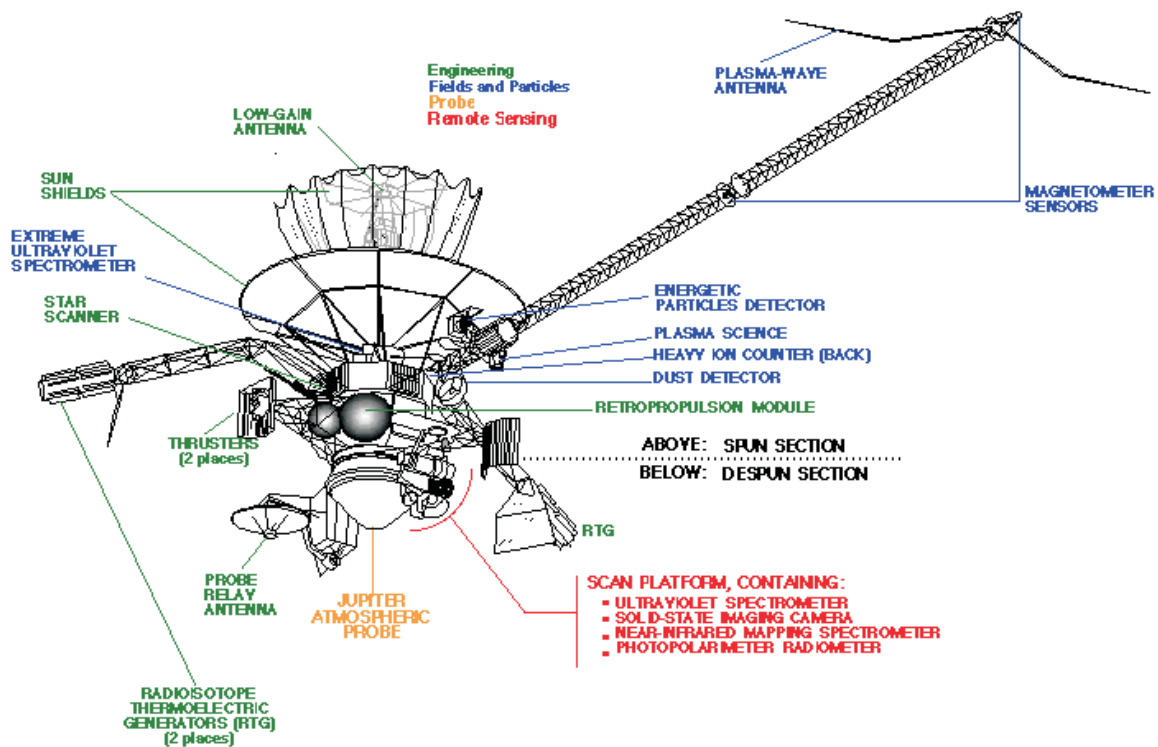


Figure 2.2: A schematic representation of the Galileo spacecraft and its instrumentation (from JPL/NASA).

3. Characterisation of the morphology, geology and physical state of the Galilean satellites;
4. Study of the composition and distribution of surface material on the Galilean satellites;
5. Determination of the gravitational and magnetic fields and dynamic properties of the Galilean satellites;
6. Characterisation of the vector magnetic field;
7. Investigation of the atmospheres, ionospheres and extended gas clouds of the Galilean satellites;
8. Study of the interaction of the Jovian magnetosphere with the Galilean satellites;
9. Characterisation of the energy spectrum, composition, and angular distribution of energetic particles.

2.2 The EPD instrument

The Energetic Particles Detector (EPD) was designed to conduct measurements of the energy, composition, intensity and angular distribution of the charged particles in the en-

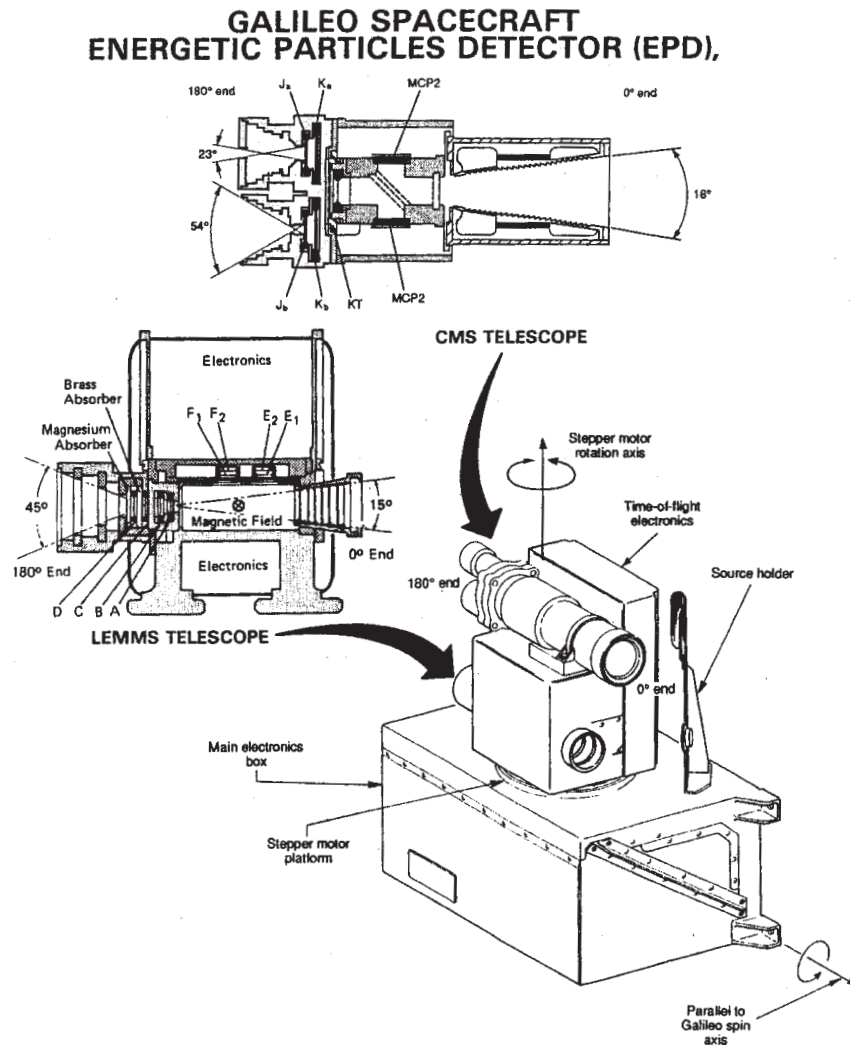


Figure 2.3: A schematic representation of the Galileo Energetic Particles Detector (EPD), showing the telescope heads, LEMMS and CMS (from Williams et al. (1992)).

environment around Jupiter. The Johns Hopkins University Applied Physics Laboratory (JHU/APL), the Max-Planck-Institut für Sonnensystemforschung (MPS) (former Max-Planck-Institut für Aeronomie, MPAe), and The National Oceanic and Atmospheric Administration Space Environment Laboratory (NOAA/SEL) resulted in the construction of the EPD instrument.

Some of the general characteristics of the EPD are given in the Table 2.1. The instrument consists of two double-headed detector systems: The Composition Measurement System (CMS) and the Low Energy Magnetospheric Measurement System (LEMMS) (Williams et al. 1992), shown in a schematic representation in Figure 2.3. EPD is mounted on a platform which rotates through 228° (Figure 2.4). Its rotation combined with the spacecraft spin allowed measurements from all directions in three dimensional space. The energy coverage for the whole system is shown in Figure 2.5.

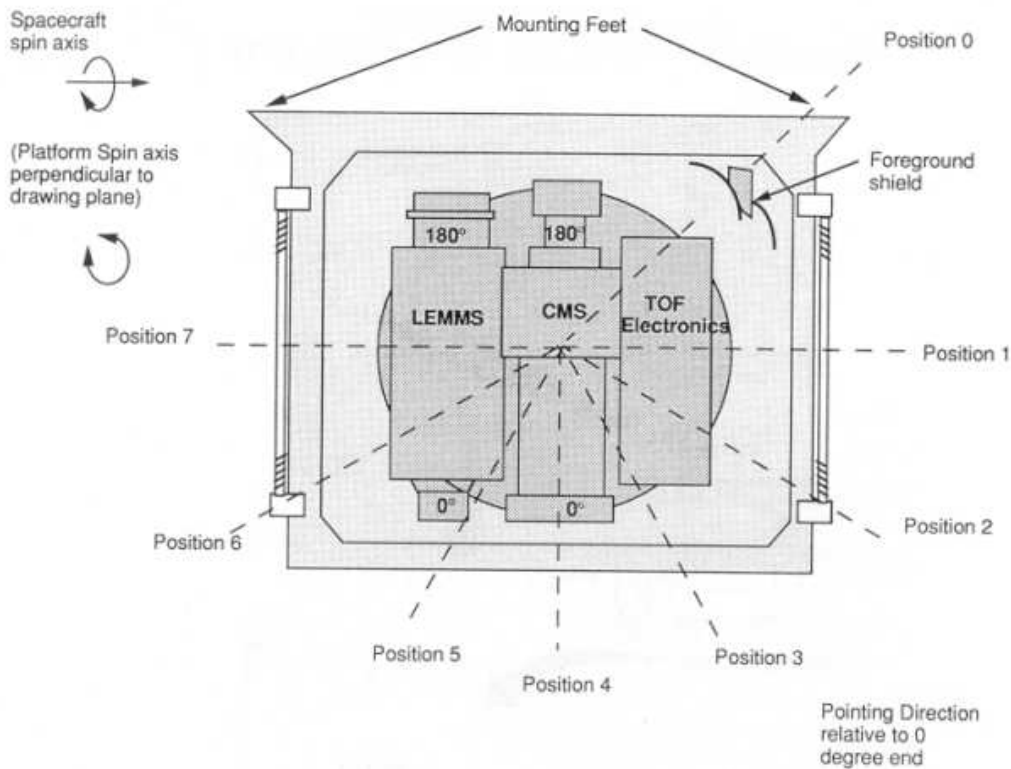


Figure 2.4: A schematic representation of EPD looking down from stepper motor rotation axis showing the EPD viewing positions (from Williams et al. (1992)).

Table 2.1: Galileo Energetic Particle Detector (EPD) general characteristics

Mass	: 10.5 Kg
Power	: 6W electronics; 4W heaters;
Bit rate	: 912 bps
Dimensions	: 19.5 cm × 27 cm × 36.1 cm
Two bi-directional telescopes mounted on the stepper platform	
4 π steradian coverage with 52 to 420 samples every 7 S/C spins (~ 140 s)	
Geometric factors : $6 \times 10^{-3} - 5 \times 10^{-1}$ cm ² ster, dependent on detector head	
Time resolution : 0.33-2,67 s, dependent on rate channel	
64 rate channels plus pulse height analysis	
Systems : magnetic deflection, $\Delta E \times E$, and time-of-flight	

2.2.1 The Composition Measurement System (CMS)

The CMS is designed to measure the ion composition of the Jovian magnetosphere in the energy range from ≈ 10 keV nucl^{-1} to > 10 MeV nucl^{-1} . It consists of two types of energetic particle telescopes, a Time-Of-Flight (TOF) telescope, covering the low energies, with one head and a typical $\Delta E \times E$ telescope, covering the higher energies, at the other

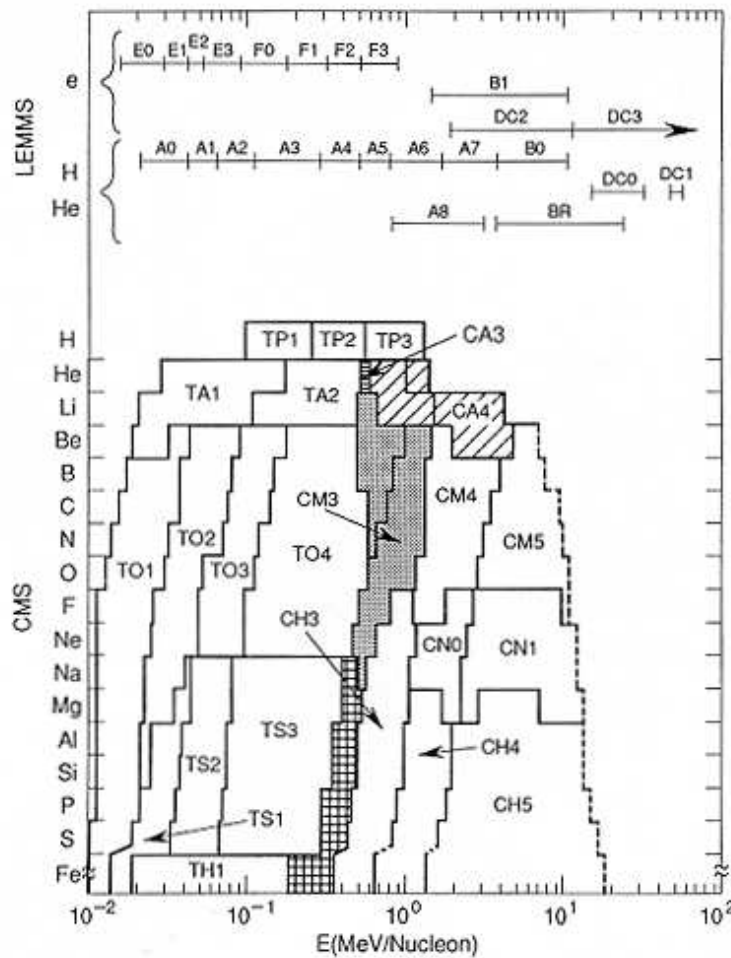


Figure 2.5: Graphical summary of the energy and species channel coverage of the whole EPD system (from Williams et al. (1992)).

(Figure 2.8). Both telescopes are separating between the different species, by determining the ion mass. The ion charge states however could not be measured. The CMS channel bandwidths are listed in Table 2.2 for reference.

CMS Time-of-Flight telescopes

The CMS TOF telescope contains a sweeping magnet followed by a thin solid state detector telescope K_T . The incoming ions pass through this foil and impinge on the K_T detector. Secondary electrons are released from the inner surface of the foil and the front surface of the K_T , detected by the microchannel plates (MCP's), which provide the start and stop pulses. By the start and stop pulses the time-of-flight between the foil and K_T is determined. Separation between the different species is obtained by the measured velocity (through the time of flight) and the ion total energy (measured by the K_T).

Figure 2.6 shows the TOF versus energy space measured by the telescope (sample: data of the Callisto 9 flyby, day 176, year 1997). 13 rate composition channels are defined

Table 2.2: Energy passbands for different ion species from the CMS detector of EPD onboard Galileo (The channel pairs used in the analysis of this thesis are highlighted in bold).

Species	Channel name	Energy Range (MeV/nucleon)	Channel name	Energy Range (MeV/nucleon)
<i>Time of Flight Channels</i>		<i>$\Delta E \times E$ Channels</i>		
Helium	TA1	0.027 - 0.155	CA1	0.190 - 0.490
	TA2	0.155 - 1.000	CA3	0.490 - 0.680
			CA4	0.680 - 1.400
Oxygen	TO1	0.012 - 0.026	CM1	0.160 - 0.550
	TO2	0.026 - 0.051	CM3	0.550 - 1.100
	TO3	0.051 - 0.112	CM4	1.100 - 2.900
	TO4	0.112 - 0.562	CM5	2.900 - 10.700
Sulfur	TS1	0.016 - 0.030	CH1	0.220 - 0.330
	TS2	0.030 - 0.062	CH3	0.330 - 0.670
	TS3	0.062 - 0.310	CH4	0.670 - 1.300
			CH5	1.300 - 15.000
Protons	TP1	0.080 - 0.220		
	TP2	0.220 - 0.540		
	TP3	0.540 - 1.250		

shown as the boxes in the matrix in Figure 2.6 and schematically as TP1, TP2, TP3, TA1, TA2, TO1, TO2, TO3, TO4, TS1, TS2, TS3 in Figure 2.5. Each point in the matrix corresponds to a combination of the measured TOF and energy signals. Only a subset of all measured particles can be processed. By normalizing each individual PHA event with the corresponding rate channel it is possible to derive fluxes and energy spectra for the measured species.

CMS $\Delta E \times E$ telescopes

The two $\Delta E \times E$ telescopes (Figure 2.8) extend the ion composition measurements of the TOF telescope to higher energies, for helium, oxygen and sulfur. Each of the $\Delta E \times E$ telescopes consists of a pair of detectors, a thin ($J_{a,b}$) and a thick ($K_{a,b}$) one. As the ions are passing through the system the ion loss energy ΔE and the remaining energy E are measured by the $J_{a,b}$ and $K_{a,b}$, respectively. By these two measurements, as well as by the thickness of the detector the atomic number Z for energies $\gtrsim 200$ keV/nucleon is calculated by the equation:

$$-\frac{\Delta E}{\Delta x} \propto \frac{Z^2}{v^2} \propto \frac{Z^2}{E} \quad (2.1)$$

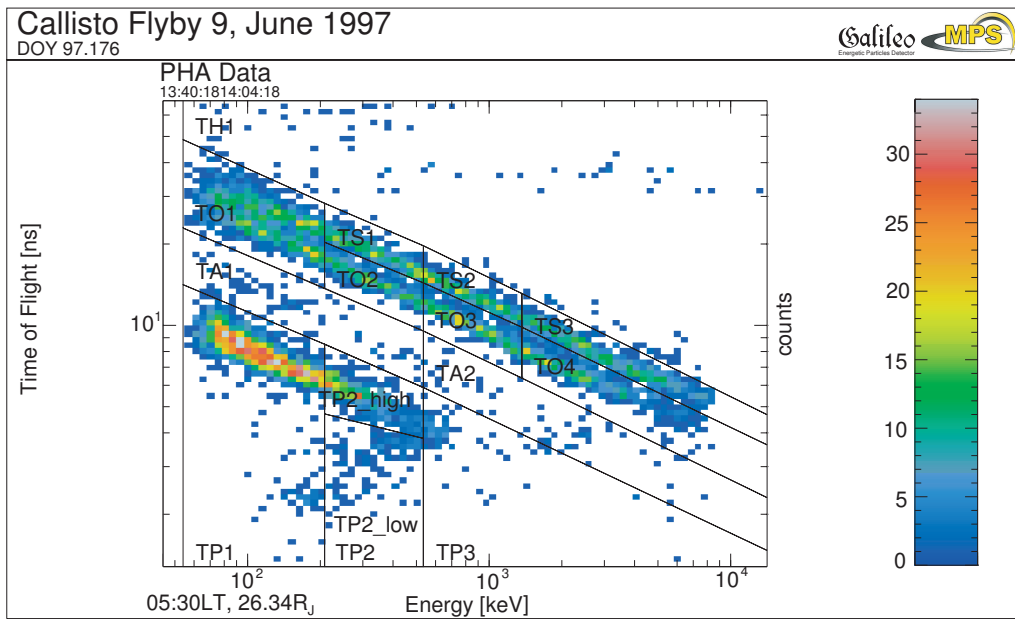


Figure 2.6: TOF versus the energy measured by the K_T detector. The TOF rate channels are separated by the diagonal and vertical lines. The calibrated data, depicted by points correspond to measurements of the Callisto 9 flyby (day 176, year 1997).

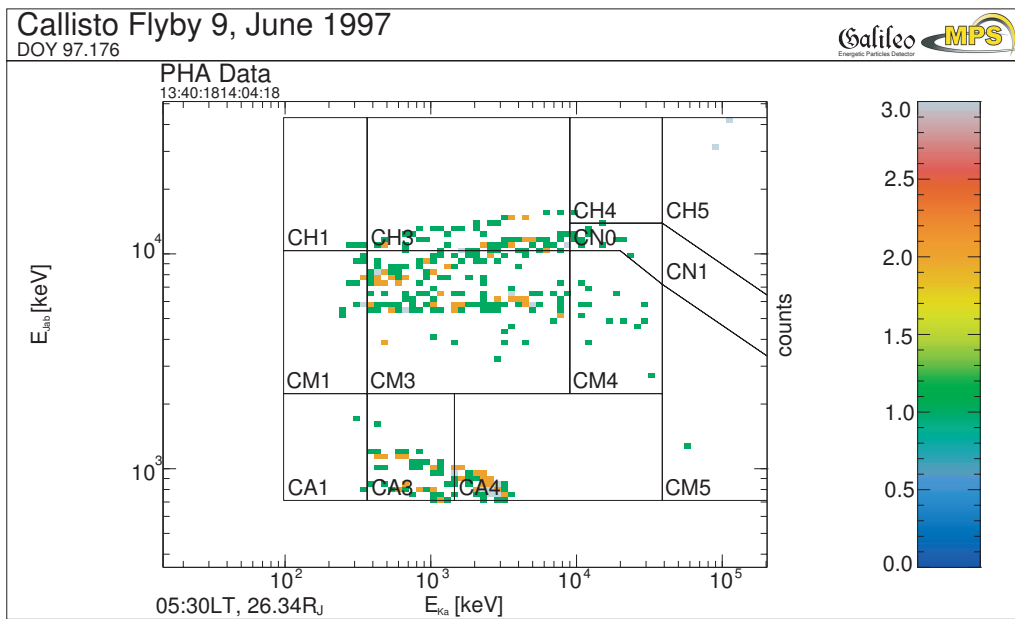


Figure 2.7: ΔE energy loss in the J detector versus the energy measured by detector K. The rate channels are separated by the vertical and horizontal lines. The calibrated data, depicted by points, correspond to measurements of the Callisto 9 flyby (day 176, year 1997).

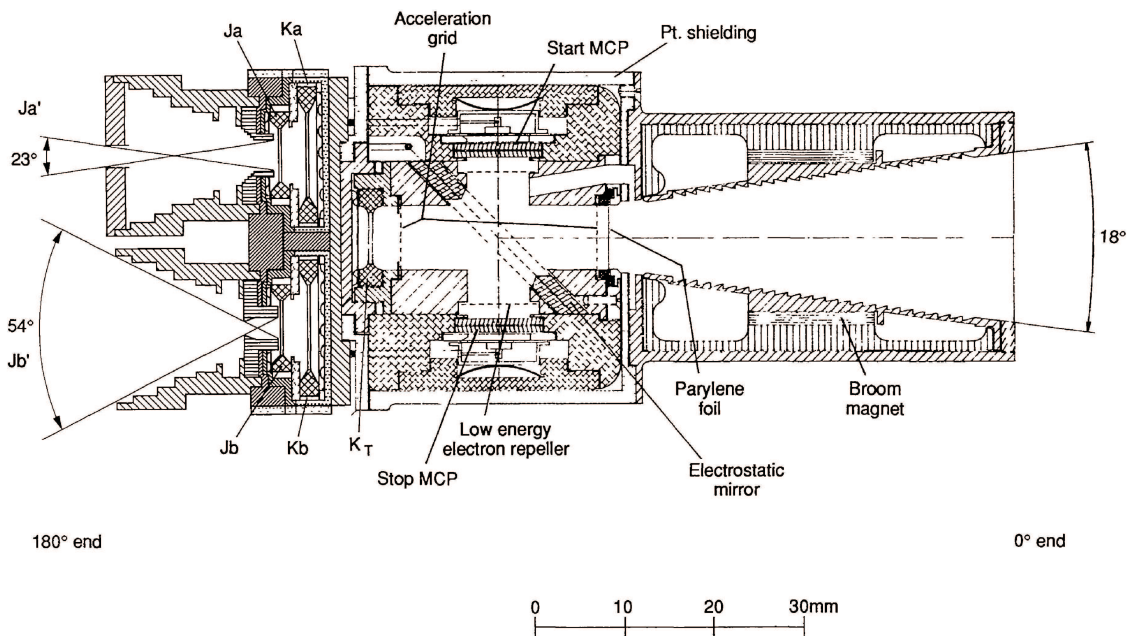


Figure 2.8: Detail of the EPD CMS detector (from Williams et al. (1992)).

In Figure 2.7 the $\Delta E \times E$ space measured by the telescope is shown (sample: data of the Callisto 9 flyby, day 176, year 1997). 10 rate composition channels are clearly defined and shown as boxes in Figure 2.7 and schematically in Figure 2.5 as CA1, CA3, CA4, CM1, CM3, CM4, CM5, CH1, CH3, CH4, CH5, CN0, CN1. The points of the matrix correspond to the energy measured by the J and the K detectors. Like in the TOF PHA matrix only subset of the measured particle is processed, while fluxes and energy spectra for the measured species can be derived by normalization of each individual PHA event.

2.2.2 The Low Energy Magnetosphere Measurement System (LEMMS)

The LEMMS telescopes, shown in Figure 2.9, measure electrons and ions at the energy range of 15 keV to > 11 MeV and 22 keV to ~ 55 MeV respectively. As the electrons are entering the 0° end they pass through a 15° full angle collimator and a series of 11 baffle plates, which define 7 hexagonal entrance channels. The electrons are deflected by the internal magnet and detected by the solid state detectors E and F. These detectors cover the energy range between 15 and 884 keV. Electronic thresholds separate this energy range in 8 channels. The ions are passing through the same collimator, but due to their higher mass they converge toward the detectors A. If their energy is high enough they impact also the detector B. The A detector measures all the ions in the energy range from 22 keV to 12,4 MeV. The C and D detectors, at the 180° end, measure ions with higher energies of $\gtrsim 14.5$ MeV and 51 MeV and electrons at $\gtrsim 2$ MeV and $\gtrsim 11$ MeV. Ion mass and charge states can not be determined by this telescope. The LEMMS channel bandwidths are listed in Table 2.3 and summarized in Figure 2.5.

Table 2.3: Energy passbands for different species from the LEMMS detector of EPD onboard Galileo (The channel pairs used in the analysis of this thesis are highlighted in bold).

Species	Channel name	Energy Range (MeV)
$Z \geq 1$	A0	0.022 - 0.042
$Z \geq 1$	A1	0.042 - 0.065
$Z \geq 1$	A2	0.065 - 0.120
$Z \geq 1$	A3	0.120 - 0.280
$Z \geq 1$	A4	0.280 - 0.515
$Z \geq 1$	A5	0.515 - 0.825
$Z \geq 1$	A6	0.825 - 1.680
$Z \geq 1$	A7	1.680 - 3.200
$Z \geq 2$	A8	3.500 - 12.40
$Z \geq 1$	B0	3.200 - 10.10
electrons	B1	$\sim 1.500 - 10.50$
$Z \geq 2$	B2	16.00 - 100.0
$Z \geq 1$	DC0	14.50 - 33.50
$Z \geq 1$	DC1	51.00 - 59.00
electrons	DC2	≥ 2
electrons	DC3	≥ 11
electrons	E0	0.015 - 0.029
electrons	E1	0.029 - 0.042
electrons	E2	0.042 - 0.055
electrons	E3	0.055 - 0.093
electrons	F0	0.093 - 0.188
electrons	F1	0.174 - 0.304
electrons	F2	0.304 - 0.527
electrons	F3	0.527 - 0.884

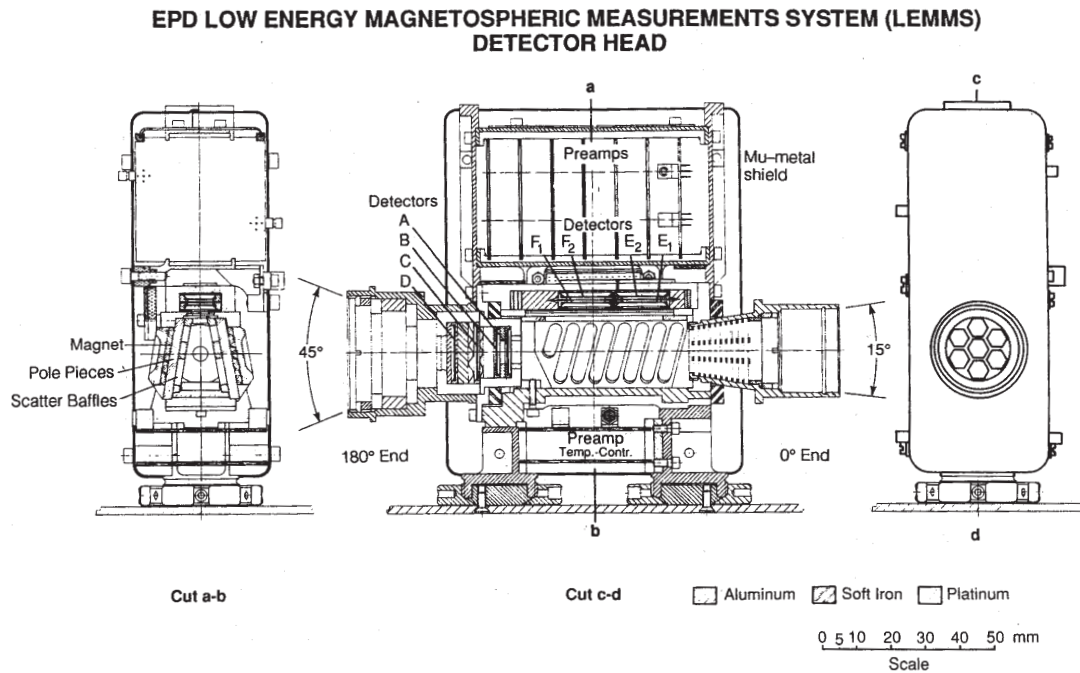


Figure 2.9: Detail of the EPD LEMMS detector (from Williams et al. (1992)).

2.2.3 Record and real time mode

The Galileo spacecraft contained a high and a low gain antenna. The High Gain Antenna which was to transmit at 134 Kilobits per second whereas the Low Gain Antenna was only intended to transmit at about 8 to 16 bits per second (later was increased to 160 bits per second). The High Gain Antenna failed to unfold after its first flyby at Earth, which forced a rearrangement of the measured data, transmitting in two different modes the record and real time mode.

The record mode data is stored on a tape recorder onboard Galileo, which limits the time coverage. It is transmitted by the low gain antenna at 10 bits per second. The time periods selected to be recorded are chosen to be the close Galilean moon flybys and the plasma sheet crossings, as areas of high scientific interest. The spacecraft's rotation is divided in 16, 32 and 64 spin sectors and a resolution of up to 448 data points from all directions in space is obtained by the seven positions of the step motor. The real mode data is available for most of the mission time, providing measurements from 16 different directions in space within 3-12 min. The transmission rate is from 5 to 40 bits per second. A more detailed analysis can be found in Lagg (1998).

For the analysis of this work mostly the real time mode data are used, since they provide a better time, local time and spatial coverage. However, the need to extend the measurements at higher energies required the use of the limited set of the record mode data where both TOF and $\Delta E \times E$ CMS telescopes were active.

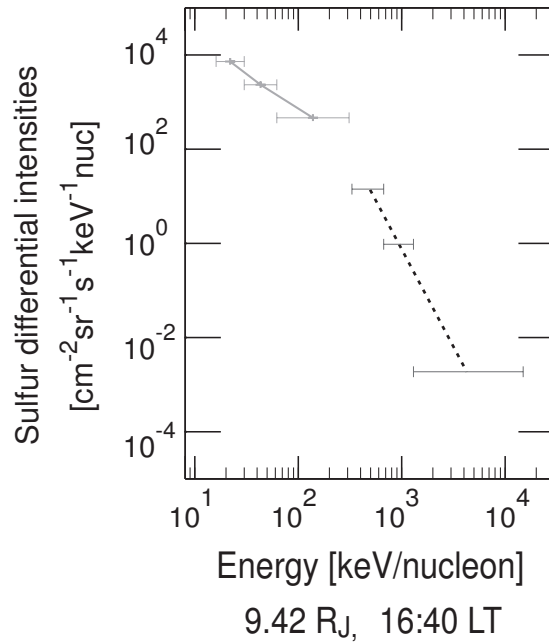


Figure 2.10: Typical energy spectra of sulfur ions in the magnetosphere of Jupiter at $9.42 R_J$ and 16:40 LT measured by the TOF (solid lines) and the $\Delta E \times E$ (dashed line) telescopes of the EPD instrument onboard Galileo.

2.3 Test of the reliability of the dataset

The Galileo EPD instrumentation provided accurate measurements of the ion energy spectra, defining its shape at the power law part of the kappa distribution, introducing a break (kink) in the energy spectral slope (Section 1.3). Figure 2.10 shows a typical sulfur spectra in the Jovian magnetosphere as measured by the CMS telescopes. The solid lines show the power law fits of the TOF energy channels and the dashed lines those of the $\Delta E \times E$ energy channels. The sample is taken at $9.42 R_J$ and 16:40 LT local time. Two power law fits are needed to describe sufficiently the ion energy spectra in the Jovian magnetosphere. The spectral kink appears between the energy range of the two detector systems (TOF and $\Delta E \times E$), which implies that different responses of the telescopes would result in it. In this section the reliability of the EPD instrumentation is tested, proving that the instrument is well calibrated, and the observed spectral shapes are not an instrumental error.

As a first step the calibration of the instrument is checked. By using equation (1.7) the count rates (cps) for the four species H, O, S and He measured by both the TOF and $\Delta E \times E$ detectors of the CMS telescope are fitted. Parametric spectral shapes with 20 free parameters (5 parameters for each species: C, kT, γ_1 , et and γ_2) are used. The fit is compared with the count rates measured by the LEMMS-telescope, which measures the sum of all individual ion species. Figure 2.11 shows the measured count rates (solid lines) and those produced by the model fit (dashed lines). Since all three detectors are working independently the reproducing of the fit is a strong argument that the EPD data set is trustworthy and that the spectral kink between the two detector systems is real and

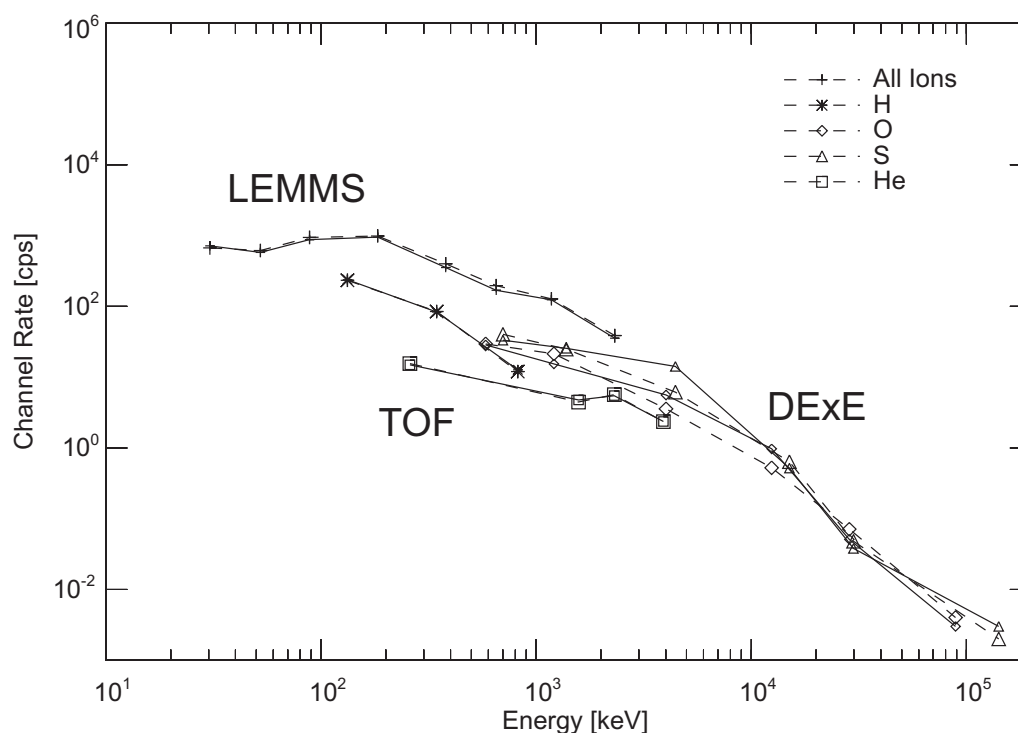


Figure 2.11: Comparison between the rate channels (cps) of the three independent telescopes of the Energetic Particles Detector EPD: TOF and $\Delta E \times E$ and LEMMS (sample on day 310, 1996, at $R=19.12 R_J$). The measured count rates of the telescopes are depicted by solid line, the dashed line indicates the fitted count rates using equation 1.7. Channels description is given in chapter 2. Adapted from Radioti et al. (2005).

present for all species.

A depletion of low energy keV fluxes, leading to the observed hardening of the spectra for lower energies (see Figure 2.10) could be caused by an additional deadlayer on the detectors, e.g., by a bombardment of high energetic particles. To complete this study a possible degradation of the instrument has been checked. Firstly it is assumed that the Jovian spectra of one particle species can be described by a power law distribution $E^{-\gamma}$, where the spectral index γ is obtained by using the high energy channels only. Then one can extrapolate to lower energies and calculate the expected particle flux for the lower energy channels (see Figure 2.12). Comparing the obtained distributions with the count rates of the LEMMS-telescope no consistent picture can be achieved. This is a strong indication that a single power law distribution does not satisfy the Jovian energy spectra for the entire energy range. Instead, an additional power law cut off at higher energies is necessary.

An extra test of the reliability of the EPD dataset is possible by analysing the data from the two Galileo flybys at Earth in a well known magnetosphere. Figure 2.13 gives a clear picture of the Earth energy spectra. The energy spectra can be perfectly described by a power law ($E^{-\gamma}$) as it is expected, taking into account that the energy range of the EPD falls into the power law region of this ion population. Apparently, the helium energy spectra (Figure 2.13) in the magnetosphere of the Earth does not exhibit a break.

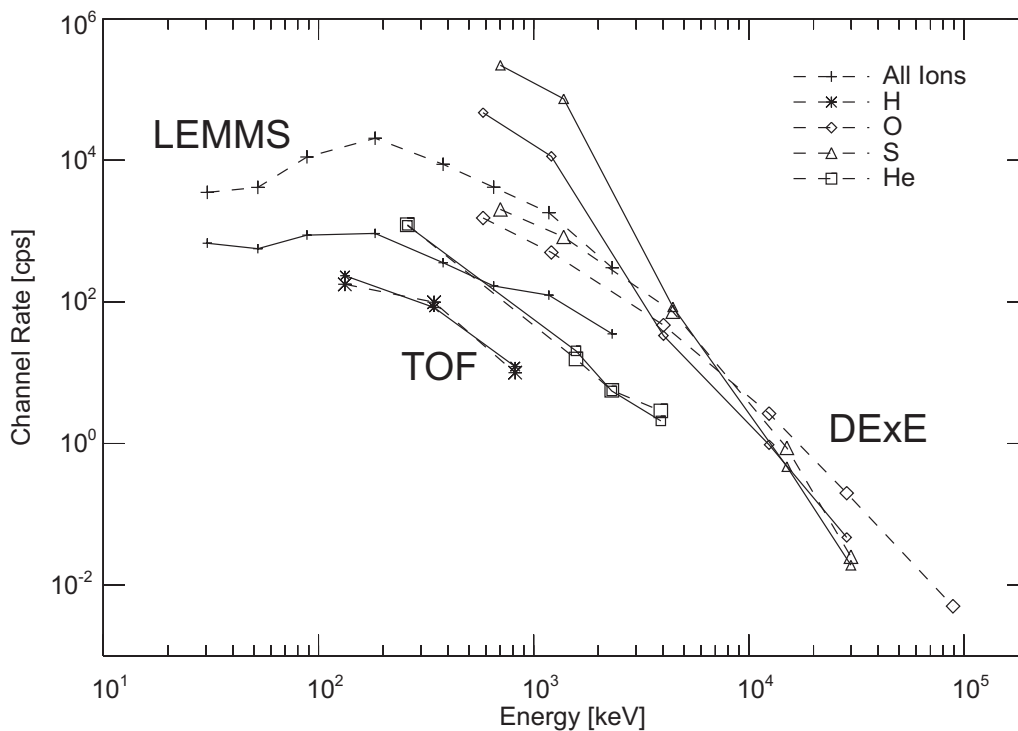


Figure 2.12: The same as Figure 2.11 (sample on day 310, 1996, at $R=19.08 R_J$). It is assumed that the Jovian energy spectra are described by a power law distribution $I \propto E^{-\gamma}$ and not by equation 1.7, where the spectral index γ is obtained from measurements of the $\Delta E \times E$ telescope and applied to the lower energy TOF channels as well. Channels description is given in chapter 2. Adapted from Radioti et al. (2005).

It is concluded that the spectral kink at energies of several 100 keV/nuc measured inside the Jovian magnetosphere is real. The EPD instrument onboard Galileo was well calibrated and instrumental effects known up to date can be excluded. The ion energy spectra shapes as it is shown in the next chapter affects the ion composition introducing a strong energy dependence of the relative ion abundance ratios. To test of reliability of the dataset equation (1.7) is used to describe the ion energy spectra. However it is only a functional form, it is derived empirically and therefore it lacks any physical meaning. The observed shape of the ion energy spectra is discussed in terms of a model of ion stochastic acceleration by Alfvén waves in Chapter 4.

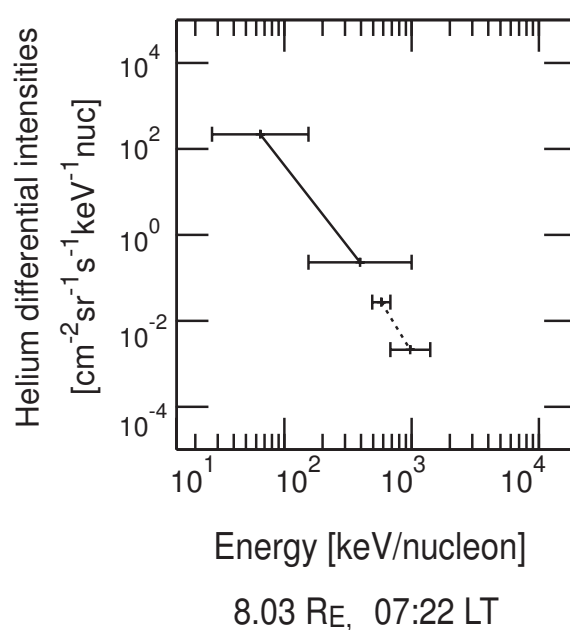


Figure 2.13: Typical energy spectra of helium ions in the magnetosphere of the Earth at $8.03 R_E$. The same format as Figure 2.10. The sample is taken during Galileo's Earth flyby in 1992 on day 343, 16.31 UT.

3 Ion composition in the Jovian magnetosphere as derived by Galileo measurements

This chapter presents a detailed analysis of the ion composition in the Jovian magnetosphere with emphasis on measurements by EPD onboard Galileo. Three different types of ions are investigated: helium as the tracer of the solar wind, sulfur and oxygen as tracers of the internal source Io, and protons with a mixed origin from the solar wind and the Jovian atmosphere/ionosphere. For the first time the relative ion abundances of S/O, S/He, O/He and p/He are calculated on a global scale and for an extended energy range. Local time dependences of these abundance ratios are analysed and temporal versus spatial variations are identified. Moreover, changes in the composition associated with magnetospheric dynamic events are investigated. Finally, a detailed comparison, with previous results, especially from Voyager 2, is presented, establishing for the first time energy dependent effects.

Ion energy spectra are fundamental to the derivation of the ion abundance ratios and contribute significantly to a better understanding of the ion composition. Therefore, a detailed description of the ion energy spectra will be given, prior to the presentation and discussion of the ion composition.

3.1 Ion energy spectra in Jovian magnetosphere

In addition to the energy spectrum samples which are shown in Chapter 2, the current section expands the discussion with more examples shown for various ions, radial distances and local time segments, as measured by the energetic particle instrumentation onboard Galileo. The aim is to establish a general shape of the ion energy spectra in the Jovian magnetosphere.

Figure 3.1 shows typical energy spectra of protons, helium and oxygen ions (from top to bottom) measured during the Earth flyby through the magnetosphere and compared to energy spectra measured inside the Jovian magnetosphere. Since the $\Delta E \times E$ detector has no proton channels, proton measurements are only extended to 1250 keV (see Table 2.2). Sulfur energy spectra and some high energy channels for oxygen at Earth are not shown due to bad statistics for these ions. Nevertheless, it is clear that within the energy range covered by EPD the ion energy spectrum in the terrestrial magnetosphere can be described sufficiently by a single power law (Vasyliūnas 1971), while in the Jovian magnetosphere at least for the heavier species, either two power law fits are needed (Mauk et

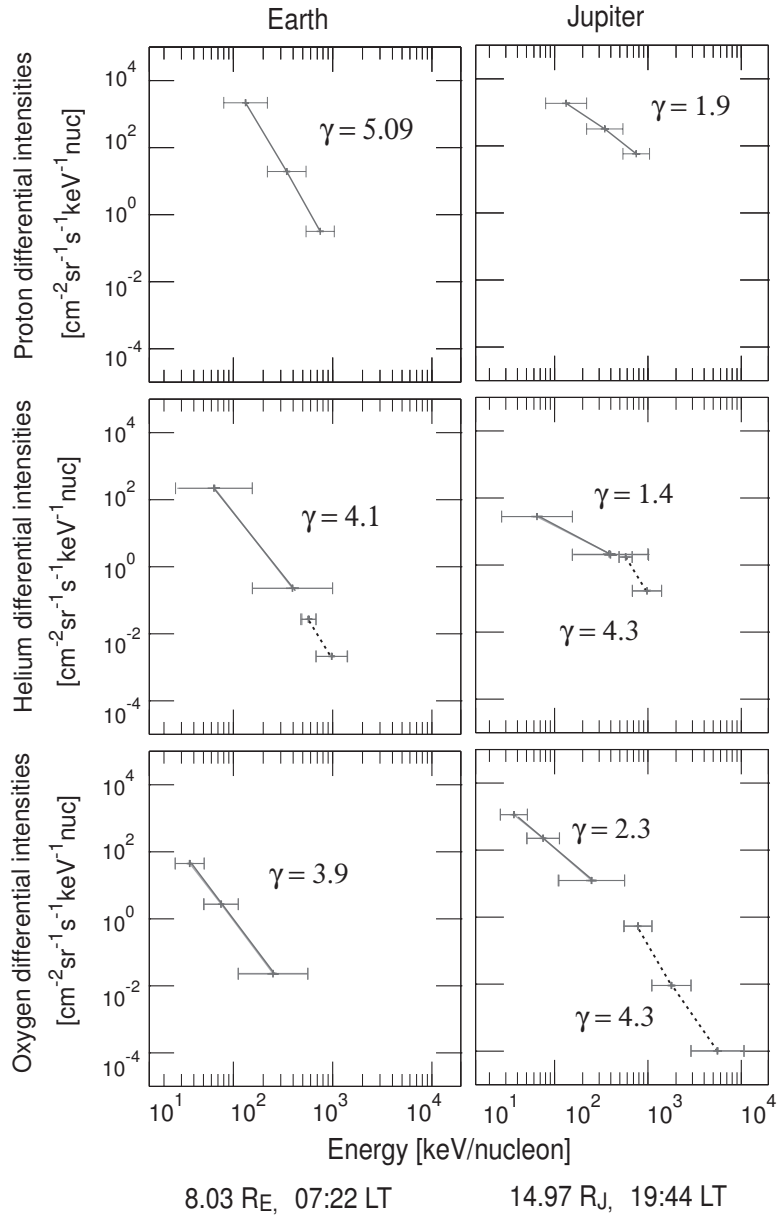


Figure 3.1: Left panels: Typical energy spectra of protons, helium and oxygen ions in the magnetosphere of the Earth at $8.03 R_E$ (sample taken during Galileo’s Earth flyby in 1992 on day 343, 16.31 UT) forming a power law distribution with $\gamma = 4.1$, $\gamma = 3.9$ and $\gamma = 5.09$ respectively. Right panels: Energy spectra of proton, helium and oxygen ions in the Jovian magnetosphere at $14.97 R_J$ (sample taken during Galileo’s orbit C3 in 1997 on day 095, 19:47 UT). The ion spectra can be fitted by two power laws for helium ($\gamma = 1.4$, $\gamma = 4.3$) and oxygen ($\gamma = 2.3$, $\gamma = 4.3$) and one for protons ($\gamma = 1.9$).

al. 1996, 1998) or a different fundamental approximation of the ion energy spectra should be considered.

Figure 3.2 shows typical ion energy spectra of protons as well as helium, oxygen and sulfur ions. The energy spectra have been calculated for different radial distances (9.55

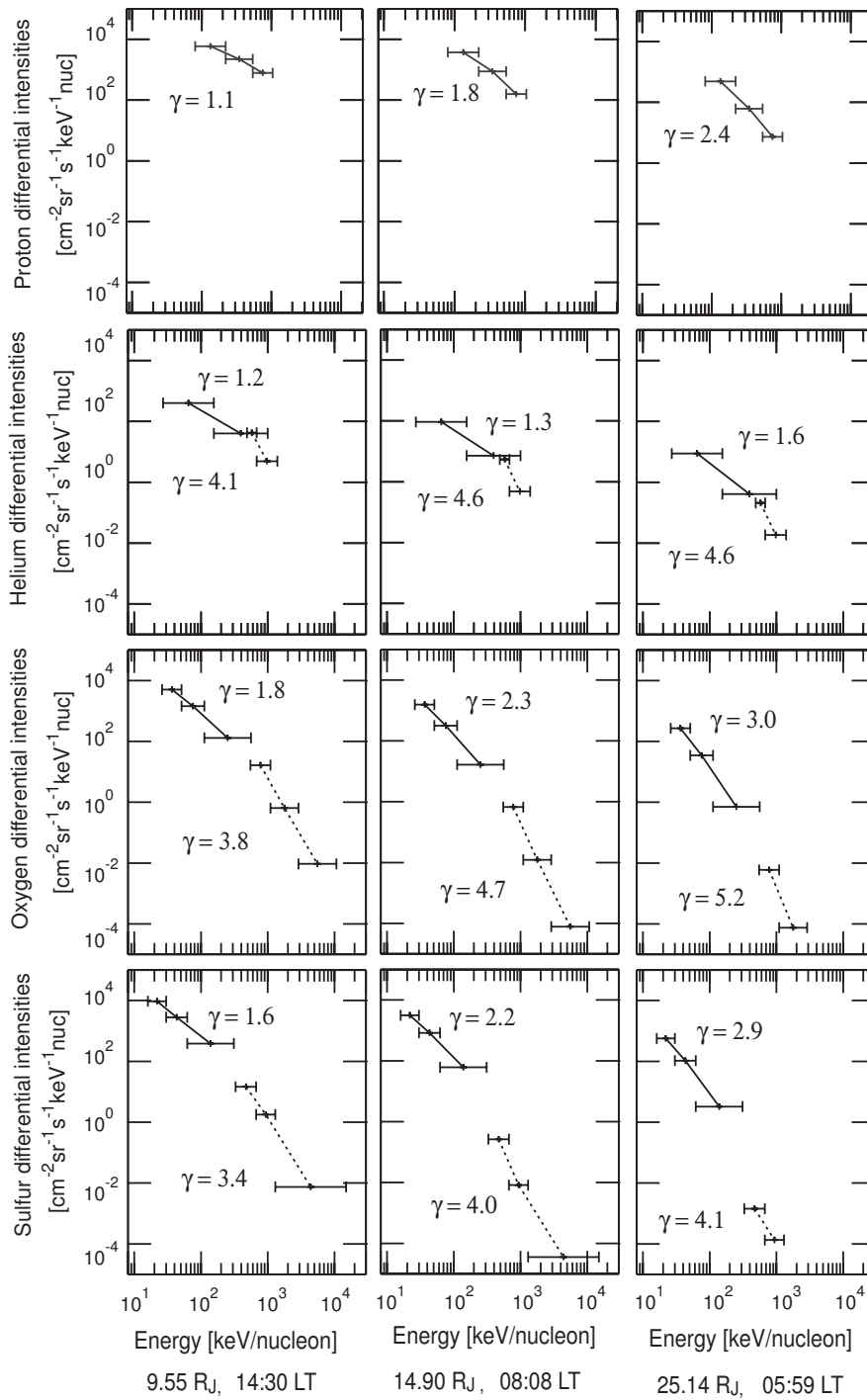


Figure 3.2: Typical energy spectra of proton, helium, oxygen and sulfur ions (top to bottom panels), the same format as figure 3.1. The samples are taken for 3 different radial distances (R_J) and local time (LT) 9.55 R_J (1998.088, 13.03 UT), 14.90 R_J (1997.127, 16.02 UT), 25.14 R_J (1997.126, 14:36 UT) (left to right panels). The heavy and dashed lines represent power law fits.

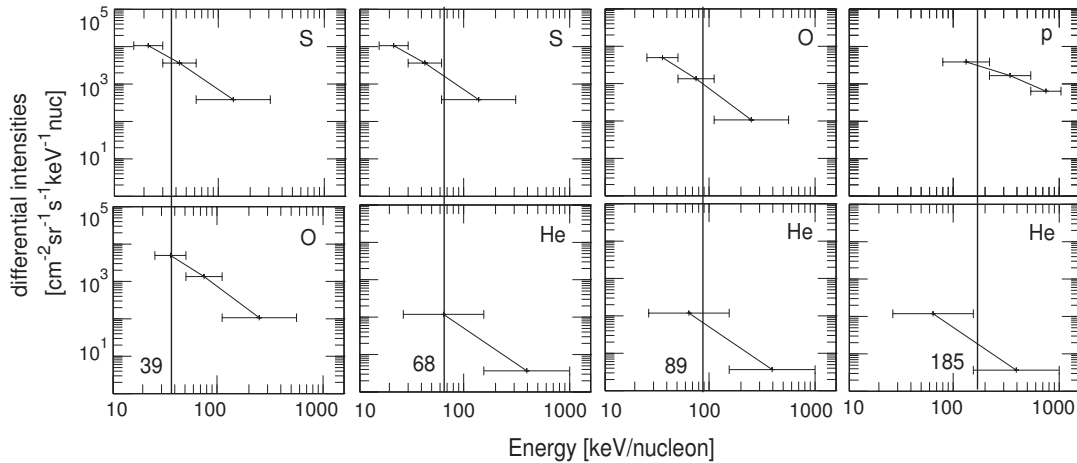


Figure 3.3: Ion energy spectra in pairs, corresponding to the abundance ratios S/O, S/He, O/He and p/He (from left to right) measured by the TOF and power law fits (solid lines). The sample is taken at $11 R_J$ and 10:30 LT during the Galileo orbit G7. The perpendicular lines indicate the energy/nuc that fits best the TOF channels for the given pair and therefore is used for the derivation of the abundance ratio.

R_J , $14.90 R_J$ and $25.14 R_J$) and local times (14:30 LT, 08:08 LT, 05:59 LT). It is again evident that a single power law cannot describe the Jovian ion energy spectra for helium, oxygen and sulfur species. Whereas possibly due to the limited energy range covered, the proton distribution is reasonably well fitted by a single power law. Despite changing intensity levels, the general spectral shape is essentially the same over the studied range of distances and local times. The spectral shapes change from a harder to a softer spectrum forming a kink in the slope at energies between 300 and 800 keV/nuc. The kink is most pronounced for helium. As it will be shown in the next sections, the ion energy spectral shape in the Jovian magnetosphere has a strong impact on the study of the ion composition and its interpretation in terms of acceleration mechanisms and source and loss processes (see the discussion on ion stochastic acceleration by Alfvén waves in Chapter 4).

3.2 Ion abundance ratios

The relative ion abundance ratios are derived by the ratio of the ion intensities for a given pair of species at a fixed energy/nuc, provided that information on the ion intensities of both species is available. Similar analysis performed by previous missions used the same proxy for the study of the ion composition (see Section 1.4). Deriving the relative ion abundance ratios in this work at the same proxy allows a comparative study with previous results. Inconsistencies can be checked and time and spatial variations can be investigated.

The energy/nuc value used for the abundance calculation is chosen to fit best the EPD energy channels for a given ion species pair. Only the low energy (TOF channels) are used, where global information is available. The energy/nuc lies at the central energy of the overlap interval of the energy channels for the given pair. The central energy is derived as the geometric mean of the upper and lower limit of the respective energy

Table 3.1: The energy per nucleon that fits best the EPD TOF energy channels for the various abundance ratios.

Relative ion abundance ratios under study	Energy (keV/nucleon)
S/O	39
S/He	68
O/He	89
p/He	185

channel. Figure 3.3 shows the energy spectra of sulfur, oxygen, helium ions and protons arranged as vertical pairs corresponding to the abundance ratios under study S/O, S/He, O/He and p/He (from left to right). Solid lines show the spectral power law fits of the intensities versus energy/nuc. The chosen energy/nuc values are indicated by the vertical lines and are listed in Table 3.1. It is clear from this figure that the ion abundance ratios depend strongly on the energy/nuc at which they are evaluated if the spectral slopes of the two species differ.

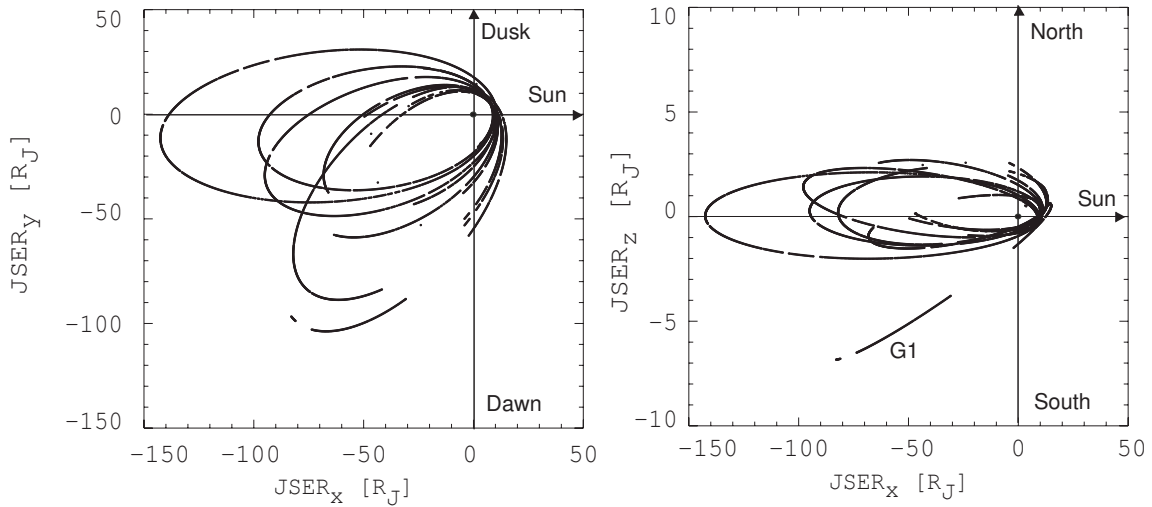


Figure 3.4: The EPD data coverage along the trajectories of the 15 first orbits of Galileo in the x-y plane (left panel) and in the x-z plane (right panel) of Jupiter Solar Ecliptic (JSE) coordinate system. Jupiter is at the origin of the system and the positive x-axis points toward the Sun, the y-axis marks the dawn-dusk meridian positive towards dusk and the z-axis points to the north. Note that the scale of the z-axis is different.

Figure 3.4 shows the segments of the 15 first Galileo orbits where EPD data are available. They are shown in the JSE coordinate system projected into the x-y plane on the left and perpendicular to it on the right. The orbits cover radial distances up to $150 R_J$ in the nightside. The dawn and dusk local time sectors are sufficiently covered in radial distance, while the noon sector, which contains the perijove of the orbits is poorly covered. The overlapping of some orbits provides better statistics within a given segment but also

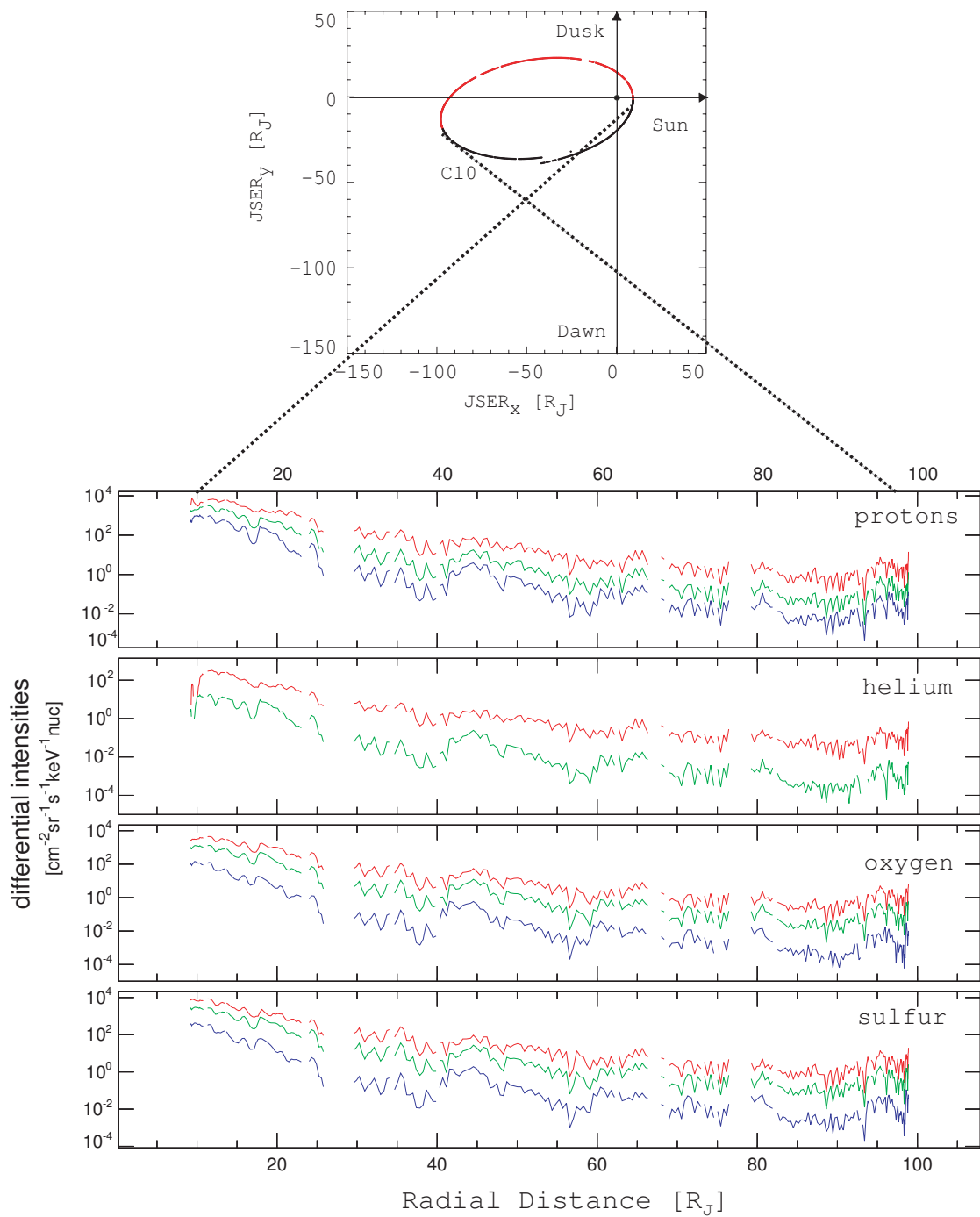


Figure 3.5: Proton, helium, oxygen and sulfur differential intensities (fluxes), measured by the various TOF energy channels as a function of radial distance for a part of the C10 orbit (shown in red in the orbit presentation at the top). The plot covers the time interval 1997.262 to 1997.286. The data are dynamical averaged over 2 min/ R_J .

gives the opportunity to study temporal effects. Most of the time the spacecraft remained in the vicinity of the equatorial plane as shown in the right panel of Figure 3.4, with an

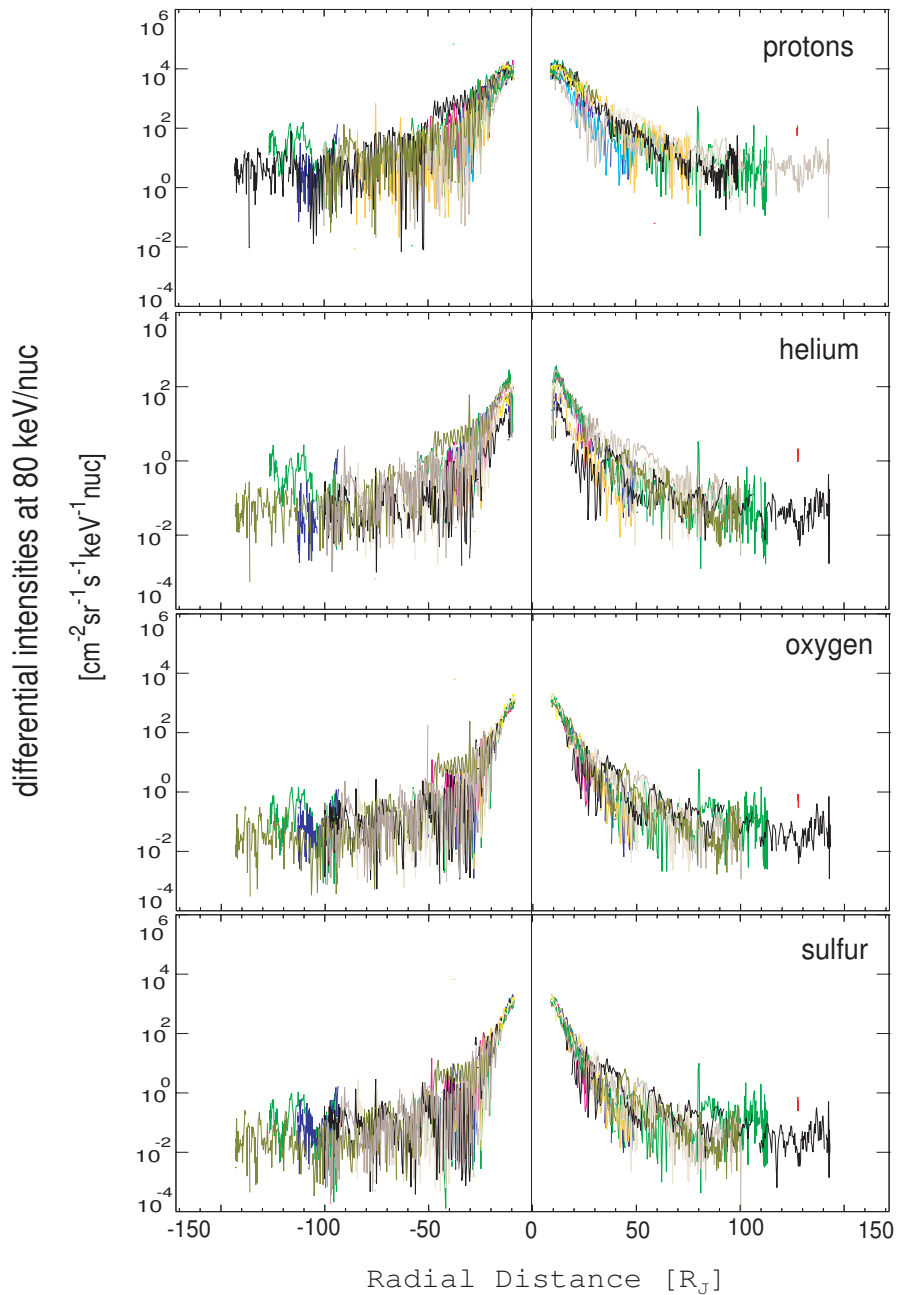


Figure 3.6: Proton, helium, oxygen and sulfur (from top to bottom) differential intensities as a function of radial distance along the inbound (left) and outbound (right) trajectories of the first 15 orbits, at 80 keV/nuc that is at an energy/nuc in the range of values used for the ion abundance calculations (see Table 3.1). The different colours denote the data from the different orbits. The data are dynamical averaged over $2 \text{ min}/R_J$.

obvious exception of the first orbit G1. For the work of this thesis the data of these orbits are analysed and projected into the equatorial x-y plane and no latitudinal effects have been considered.

Before the presentation of the relative ion abundance ratios some examples of the

ion intensities as measured by the Galileo energetic particle instrumentation are shown. Figure 3.5 shows the measured intensities of protons, helium, oxygen and sulfur ions as a function of radial distance from Jupiter along the Galileo C10 orbit (1997.262 - 1997.286) for different energies. The intensities for all species depend on the radial distance and on the energy range. It is obvious that they are decreasing with increasing distance from the planet and they are lower for higher energies. The ion intensities are not only varying with distance and energy but also with time and/or local time. Figure 3.6 shows the variations of the ion intensities of protons, helium, oxygen and sulfur ions as a function of the radial distance, along the inbound and outbound trajectories of the first 15 Galileo orbits. The different colours represent the different orbits. The intensities are calculated at 80 keV/nuc approximately at the average energy/nuc that the ion abundance ratios are calculated (see Table 3.1). Large variations of the ion intensities up to 2 orders of magnitude are present in consecutive Galileo orbits. However, with this plot local time dependences and temporal effects cannot be differentiated.

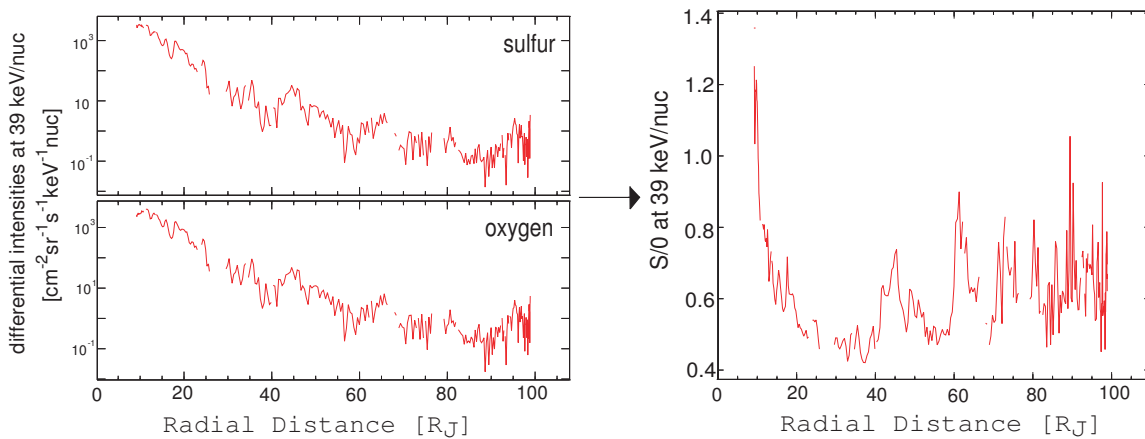


Figure 3.7: Left: Sulfur and oxygen ion intensities at 39 keV/nuc as a function of radial distance along a part of the C10 orbit (1997.262 to 1997.286), marked with red in Figure 3.5. Right: S/O ion abundance ratio derived from the ratio of the sulfur and oxygen ion intensities for the same time interval.

As mentioned already the ion abundance ratios are calculated by the ratio of the ion intensities at a specific energy/nuc of a given pair of species. Figure 3.7 shows an example of the derivation of the S/O ion abundance ratio. In the left panel sulfur and oxygen ion intensities at 39 keV/nuc as a function of distance are presented along a part of the C10 orbit (the same part shown in Figure 3.5). The right panel shows the corresponding S/O ion abundance ratios. S/He, O/He and p/He relative abundance ratios are calculated at 68, 89 and 185 keV/nuc by the same way.

3.2.1 Global maps

S/O abundance ratio

In the following the first global maps of relative ion abundance ratios in Jupiter's magnetosphere will be presented. In a first step the abundance ratios have been calculated for

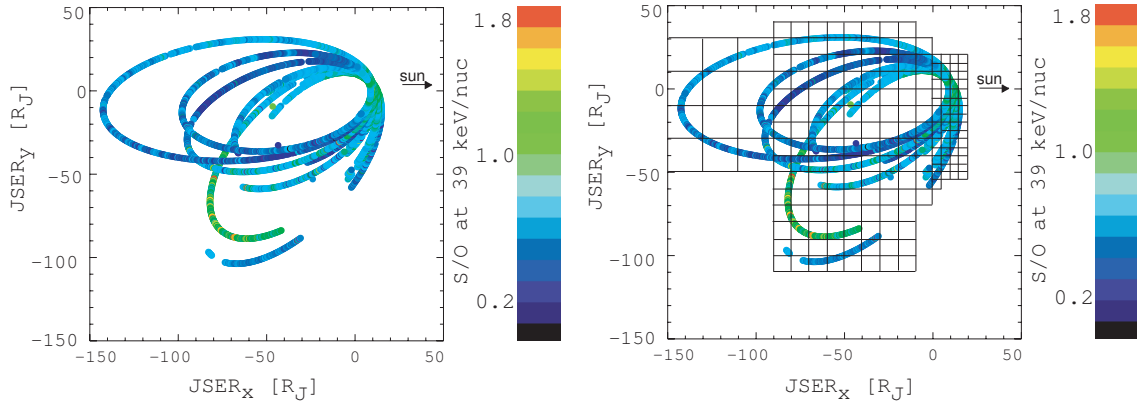


Figure 3.8: Color-coded relative abundance ratios of S/O, calculated at 39 keV/nuc and projected along the first 15 Galileo orbits in the x-y plane of the JSE coordinate. The data are dynamically averaged over $2 \text{ min}/R_J$. Ion abundance ratio values are shown only if reliable information about the ion intensities of both ion species is available. The right panel shows the spatial binning in boxes of 5×5 , 10×10 and $20 \times 20 R_J$, which is adjusted to the data coverage.

each orbit individually (Figure 3.8). Data obtained during the time interval of day 136 to 256, 1997, are excluded from the calculation of all ratios relative to helium, due to instrumental deficiencies affecting the helium channels for this time period. To enhance the statistical significance of the data at larger distances dynamical averaging of $2 \text{ min}/R_J$ has been used. In a second step the data are spatially binned and averaged in 5×5 , 10×10 and $20 \times 20 R_J$, as shown in the right panel of Figure 3.8. By this procedure color-coded global maps of the ion abundance ratios are constructed. These maps will serve to establish the various sources and sinks to investigate the ion distribution at various radial distances to identify specific areas of interest and to compare with results from previous missions.

The results of the spatial binning are shown for various ion ratios in Figure 3.9. The top left panel shows the color-coded global map of the S/O ion abundance ratio calculated at 39 keV/nuc. The ratio ranges between 0.4 and 1.2. Very close to the planet at radial distances of 5 to $10 R_J$ close to the local noon the ratio is around 1. The ratio is decreasing with increasing radial distance through the tail and reaches values around 0.4. Beyond $80 R_J$, in the tail region, the ratio stays comparatively constant, only marginally decreasing with distance. These results are in general accordance with measurements by Voyager 1 and 2 (Krimigis et al. 1979a, Vogt et al. 1979b, Hamilton et al. 1980, 1981), Ulysses (Lanzerotti et al. 1992, Krupp 1994) and Galileo (Cohen et al. 2001, Mauk et al. 1998, MacLennan et al. 2001, Waldrop 2004) at the respective radial distances (see Table 3.2). Small deviations between the ratios derived previously by EPD and these results could be explained by the fact that the previous measurements were only obtained on individual orbits, whereas the values presented here are the averaged ratios of all orbits in a given local segment. The S/O abundance ratio has been additionally compared with the Voyager 2 ratios for the same local time and radial distances. The result of this comparison is described in detail in Section 3.2.5 in association with energy dependent effects.

3 Ion composition in the Jovian magnetosphere as derived by Galileo measurements

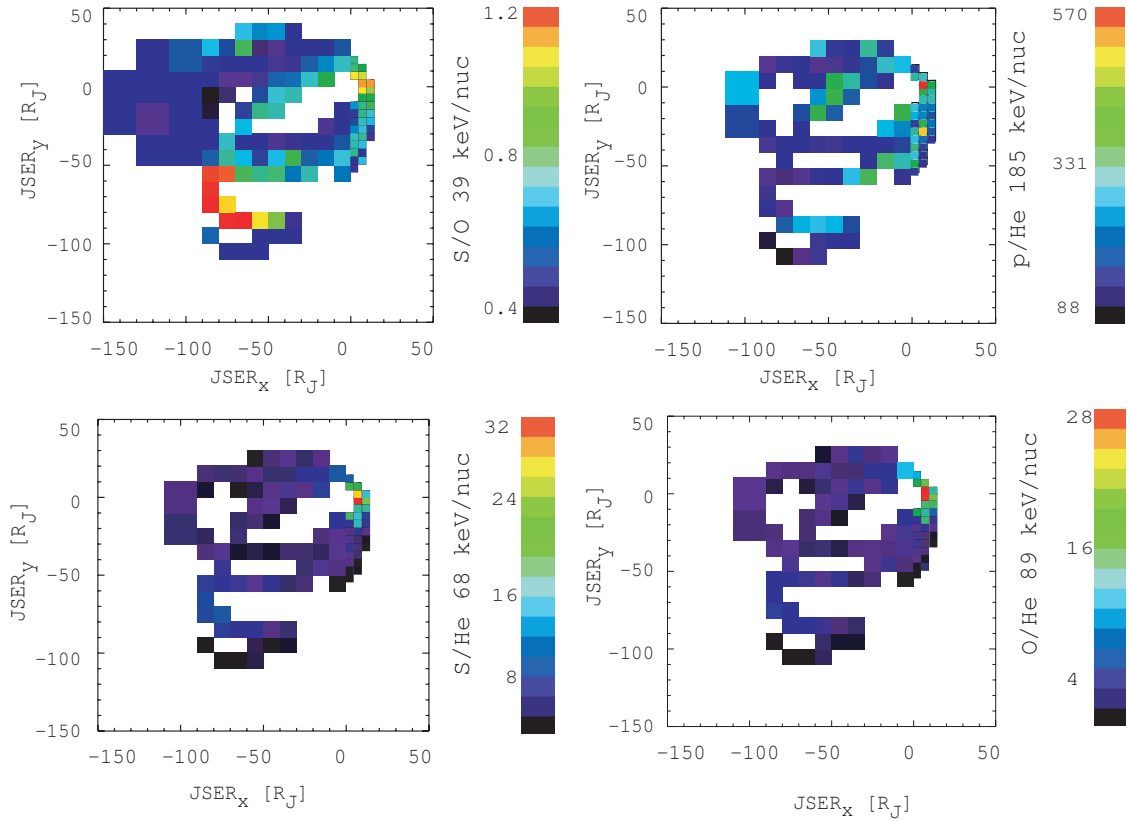


Figure 3.9: Color-coded relative abundance ratios of S/O, S/He, O/He and p/He calculated at 39, 68, 89 and 185 keV/nuc respectively and projected on the x-y plane of the JSE coordinate system. Data from the first 15 orbits are spatially binned in boxes of 5, 10 and 20 R_J .

The S/O ratio values exhibit a pronounced increase of the average ratio up to 1.2 along the predawn sector, compared to the usual 0.5 in the vicinity. This anomaly is probably associated with burst events which are present in that specific region. A more detailed discussion will follow in Section 3.2.3, where the composition at this region is discussed separately. A sporadic increase in the S/O abundance ratio of up to 0.6 beyond 60 R_J , compared to the ambient values in the range of 0.3 to 0.4 is also reported by Hamilton et al. (1981).

Sulfur and oxygen are mainly originating from Io and the S/O ratio of the neutral sources ranges between 0.25 and 0.58 according to Voyager 1 and Cassini measurements (Section 1.2.2). The neutrals are ionised, the newly created ions are emitted from the torus at the energy of several eVs to tens of eVs and they are subject to various transport and acceleration mechanisms until they are detected by the Galileo energetic particle instrumentation. Therefore the values derived here cannot be directly compared to the Io torus composition.

Table 3.2: Ion abundance ratios in the Jovian magnetosphere

	Energy (MeV/nuc)	Location(R_J)	S/O	p/He	S/He	O/He
Pioneer 10 (Trainor et al. 1974)	3.2-5.6	32-88		1666-166		
Pioneer 10 (Simpson et al. 1974b): Figure 16	1	13-40		300-40		
Voyager 1 LECP (Krimigis et al. 1979a): Table 1	0.6-1.6	40-47	0.34 ^a		0.103 ^a	0.3 ^a
	0.6-1.6	47-49	0.35 ^a		1.06 ^a	3.02 ^a
	0.6-1.6	59-67	0.35 ^a		0.047 ^a	0.13 ^a
Voyager 1 CMS (Vogt et al. 1979a): Table 1	7-14	4.9-5.8	0.76±0.09			
Voyager 2 LECP (Krimigis et al. 1979b)	0.5-1.7	30-60		50-300 ^b		
	0.6-0.95	15-60			0.006-0.07 ^b	0.02-0.1 ^b
Voyager 2 LECP (Hamilton et al. 1980)	0.6-0.95	51-56	0.25	60±3	0.0057±0.0005	0.02±0.001
Voyager 2 LECP (Hamilton et al. 1981)	0.6-1.15	20-60		50-200 ^b		
	0.6-1.15	10-60	0.6-0.2 ^b		0.006-0.4 ^b	0.03-0.66 ^b
Voyager 2 CMS (Vogt et al. 1979b)	7.8-10.5	10.1-10.6	0.62 ^{+0.24} _{-0.19}			
	7.8-10.5	10.6-25	0.18±0.07			
Ulysses HI-SCALE (Lanzerotti et al. 1992): Fig. 5	0.5-1.4	12-58	0.3-1 ^a		0.003-0.2 ^a	0.01-0.2 ^a
Ulysses EPAC (Krupp 1994)	0.45-1.6	15-110	0.413 ^a		0.031 ^a	0.075 ^a
Galileo HIC (Cohen et al. 2001): Fig. 5	4.5-18.4	10-30	0.1-0.05			
Galileo EPD (Mauk et al. 1998): Fig. 2	0.5	7.48	0.77			
	1.0	7.48	0.75			
Galileo EPD (MacLennan et al. 2001)	0.5-0.7	9.1-9.6	0.67±0.06			
	0.7-1.0	9.1-9.6	0.71±0.05			
	1.0-1.4	9.1-9.6	0.58±0.15			
Galileo EPD (Waldrop 2004)	0.025	5-150	0.3-0.8 ^c			
Galileo EPD (this work)	0.039	5-150	0.4-1.2 ^d			
	0.039	10-65	0.9-0.6 ^e			
	0.185	5-150		88-570 ^d		
	0.185	15-50		172-243 ^e		
	0.8	15-50		146-215 ^e		
	0.068	5-150			0.4-33.6 ^d	
	0.068	15-65			10.24-1.07 ^e	
	0.8	15-65			1.2-0.56 ^e	
	0.089	5-150				0.52-27.6 ^d
	0.089	15-65				7.88-1.0 ^e
	0.8	15-65				1.34-0.52 ^e

^ainbound trajectory^boutbound trajectory^csingle orbits^dbinned average^eclose to the outbound trajectory of Voy 2

S/He, O/He and p/He abundance ratios

Global maps of S/He and O/He abundance ratios calculated at 68 and 89 keV/nuc respectively are shown in the bottom panels of Figure 3.9. On the dayside of the magnetosphere at close distance to the planet the S/He and O/He ratios reach their highest values of 32 and 28, respectively. All ion fluxes decrease significantly towards the night side and/or with distance from the planet. However, as seen from the decreasing abundance ratios sulfur and oxygen ion fluxes decrease stronger than helium ion fluxes. These results agree within one order of magnitude with previous results compared at respective radial distances (see Table 3.2). Differences of the ratios between the various missions can be attributed to spatial and temporal variations (see Section 3.2.4) or could be a result of an energy dependence (see Section 3.2.5).

The derived globally p/He abundance ratio calculated at 185 keV/nuc is shown in the top right panel of Figure 3.9. The ratio ranges from ~ 90 to ~ 600 . In the midnight sector, in a region between 30 to 50 R_J , the values are significantly higher compared to those at larger distances. The same abundance ratio measured onboard the previous missions exhibit a wide range of values which agree well with the average ratio calculated by Galileo EPD. The p/He abundance ratio does not show a clear trend, consistent with the mixed origin of protons composing external (the solar wind) and internal (the Jovian atmosphere/ionosphere) sources and the loss of low energy protons (80 to 220 keV) near the moon Europa.

3.2.2 Local time asymmetries

The trajectory of Galileo in the Jovian system enabled a comparative study of the ion composition at different local times. Figure 3.10 shows the color-coded global map of the S/O abundance ratio at 39 keV/nuc. The x-y plane is divided into 8 different local time sectors: Predawn (01:30-04:30 LT), Dawn (04:30-07:30 LT), Prenoon (07:30-10:30 LT), Noon (10:30-13:30 LT), Predusk (13:30-16:30 LT), Dusk (16:30-19:30 LT), Pre-midnight (19:30-22:30 LT) and Midnight (22:30-01:30 LT). The Noon and the Pre-dusk sectors provide very limited data coverage only up to very few R_J and therefore are not considered for the comparative study.

The abundance ratios for each of the remaining 6 local time sectors are averaged over radial intervals of 3 R_J . Figures 3.11, 3.12, 3.13 and 3.14 show the S/O, S/He, O/He and p/He abundance ratios calculated for those local time sectors versus radial distance.

Generally, the ion abundances do not exhibit major variations with local time. An obvious exception is the predawn sector. The results of Maclennan et al. (2001) that oxygen and sulfur fluxes are independent on local time at least at distances of 10 R_J are confirmed by this work. The S/O, O/He and S/He ion abundance ratios along the predawn sector exhibit a pronounced increase at radial distances of 70 to 120 R_J . This feature is associated with global reconfiguration processes in the Jovian magnetotail (Section 1.2.2) and will be discussed in more detail in Section 3.2.3.

The p/He ratio (Figure 3.14) exhibits a different pattern in terms of local time variations. The large error bars in the ratio in all local time sectors imply large deviations of the averaged values. Moreover, it does not show a clear increase along the predawn sector like the other relative abundance ratios.

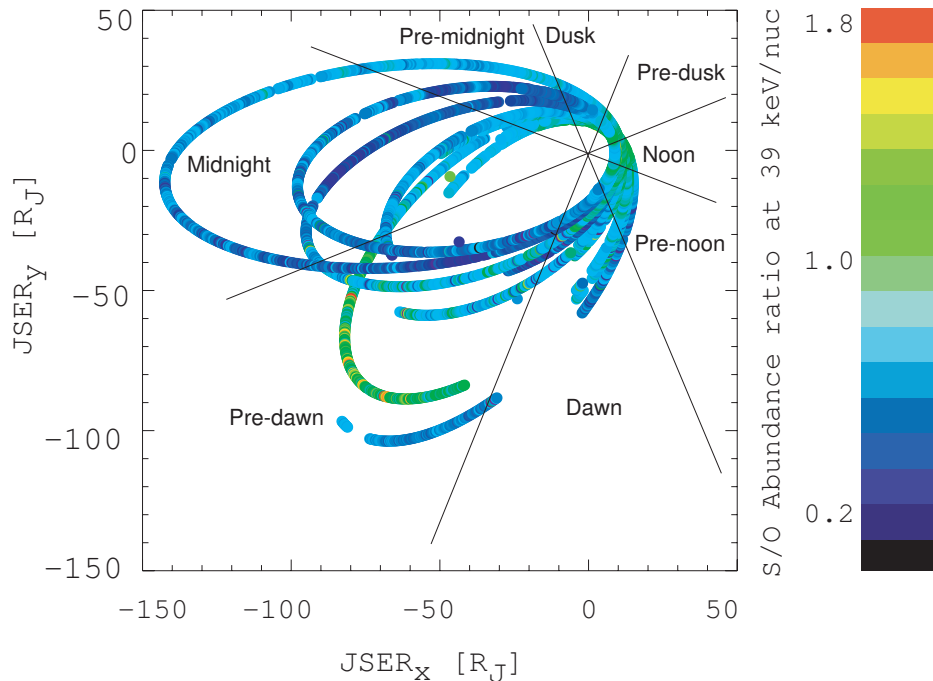


Figure 3.10: Color-coded relative S/O abundance ratios, calculated at 39 keV/nuc and projected along the first 15 Galileo orbits in the x-y plane of the JSE coordinate. The format is the same as in Figure 3.8. 8 local time sectors are separated by the solid lines: Predawn (01:30-04:30 LT), Dawn (04:30-07:30 LT), Preenoon (07:30-10:30 LT), Noon (10:30-13:30 LT), Predusk (13:30-16:30 LT), Dusk (16:30-19:30 LT), Premidnight (19:30-22:30 LT) and Midnight (22:30-01:30 LT)

The local time pattern as derived by the Galileo observations extends and modifies the composition pattern derived by Cheng and Krimigis (1989). Based on the corotation-convection model these authors suggested that in the predawn sector the composition of heavy ions is enhanced from close to the planet up to relatively large distances (see Figure 1.17). This pattern was confirmed by observations along the Voyager 2 outbound trajectory, which observed enhanced heavy ion composition close to the planet but also beyond $60 R_J$. Based on the Galileo coverage of 4 local time sectors (dawn, predawn, premidnight and dusk) it can be assumed that the ion composition close to the planet within $\sim 30 R_J$ is symmetrical. A heavy ion composition comparable to that observed close to the planet is also found in the predawn sector but only between 70 to $120 R_J$ and related to reconfiguration events.

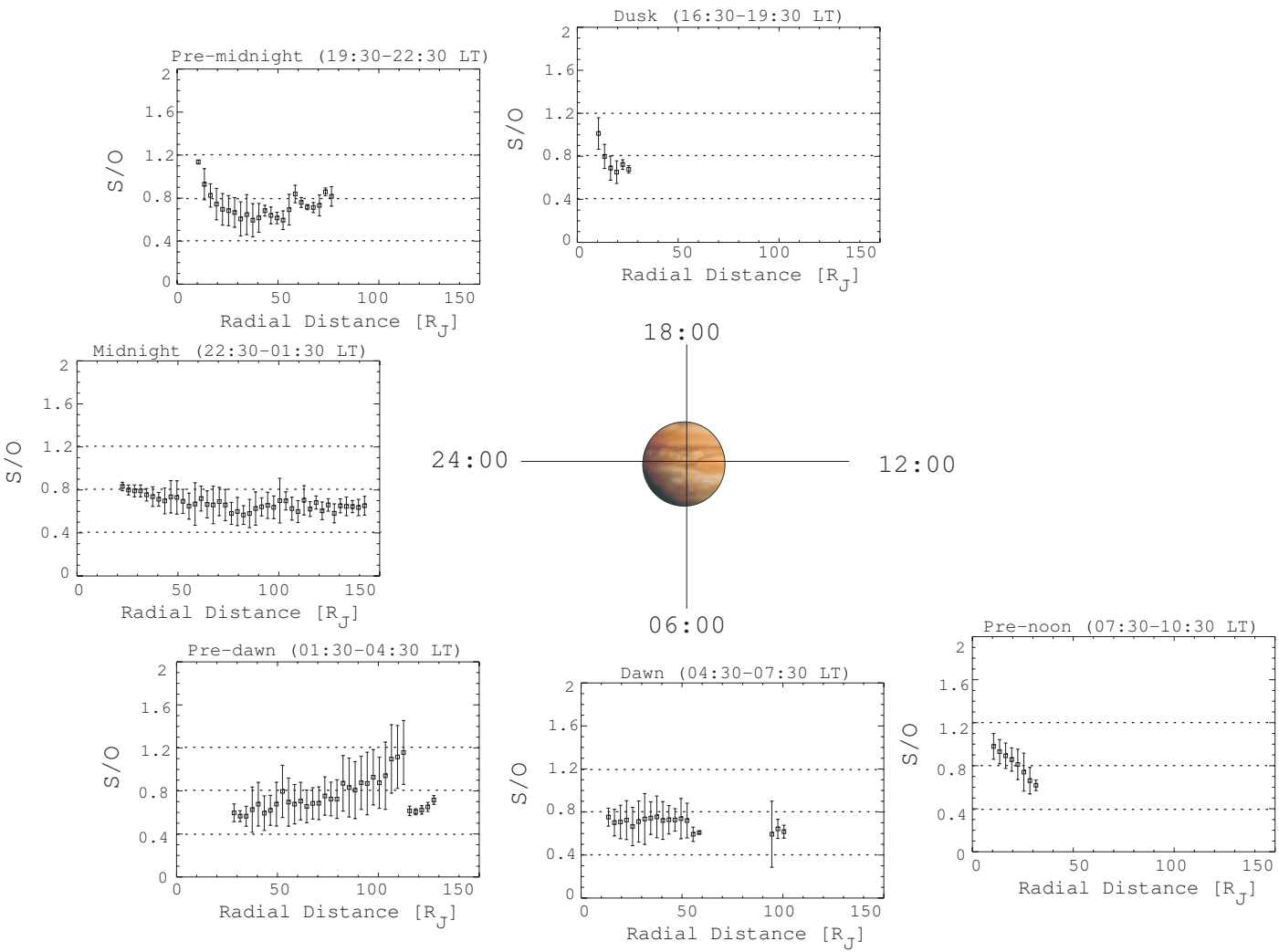


Figure 3.11: S/O ion abundance ratio, calculated at 39 keV/nuc averaged over the 6 different local time sectors (see Figure 3.10 and over $3 R_J$ and plotted versus radial distance. The error bars correspond to the standard deviation of the mean value in a given distant interval. The ratio for the 6 local time sectors is placed in a schematic representation with Jupiter in the center and sun to the right.

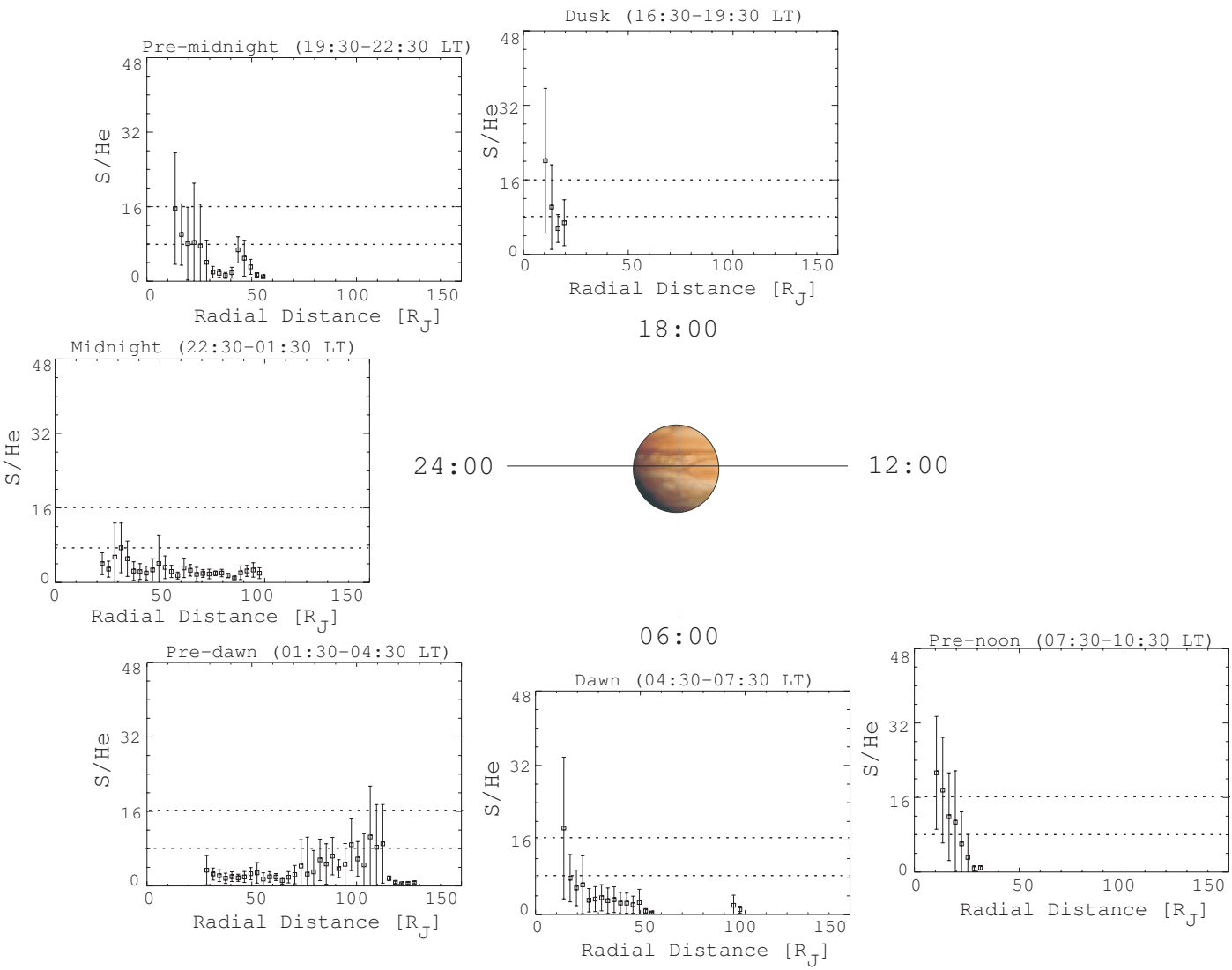


Figure 3.12: S/He ion abundance ratio, calculated at 68 keV/nuc averaged within 6 different local time sectors and over $3 R_J$ and plotted versus radial distance. The format is the same as Figure 3.11.

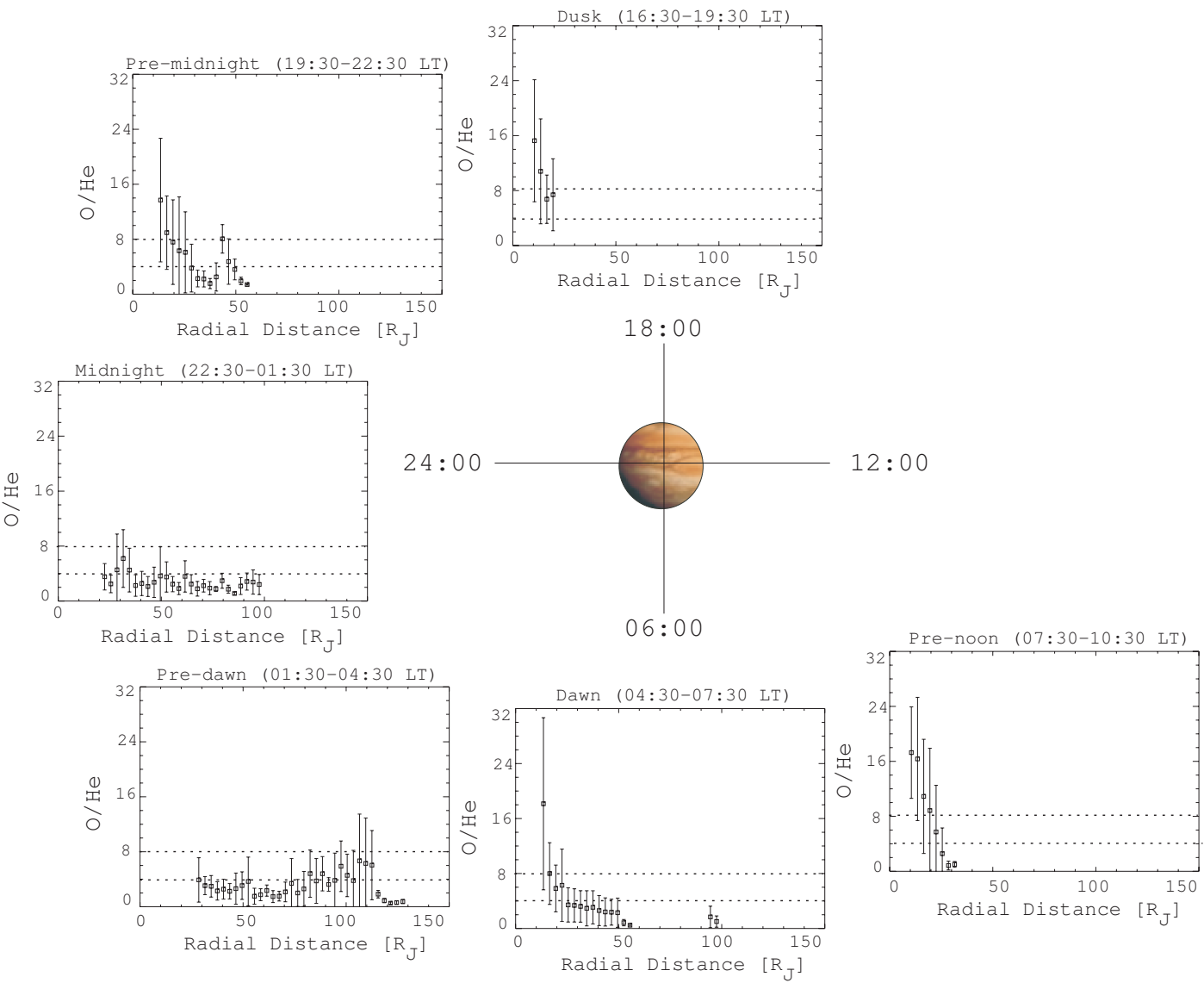


Figure 3.13: O/He ion abundance ratio, calculated at 89 keV/nuc averaged within 6 different local time sectors and over $3 R_J$ and plotted versus radial distance. The format is the same as Figure 3.11.

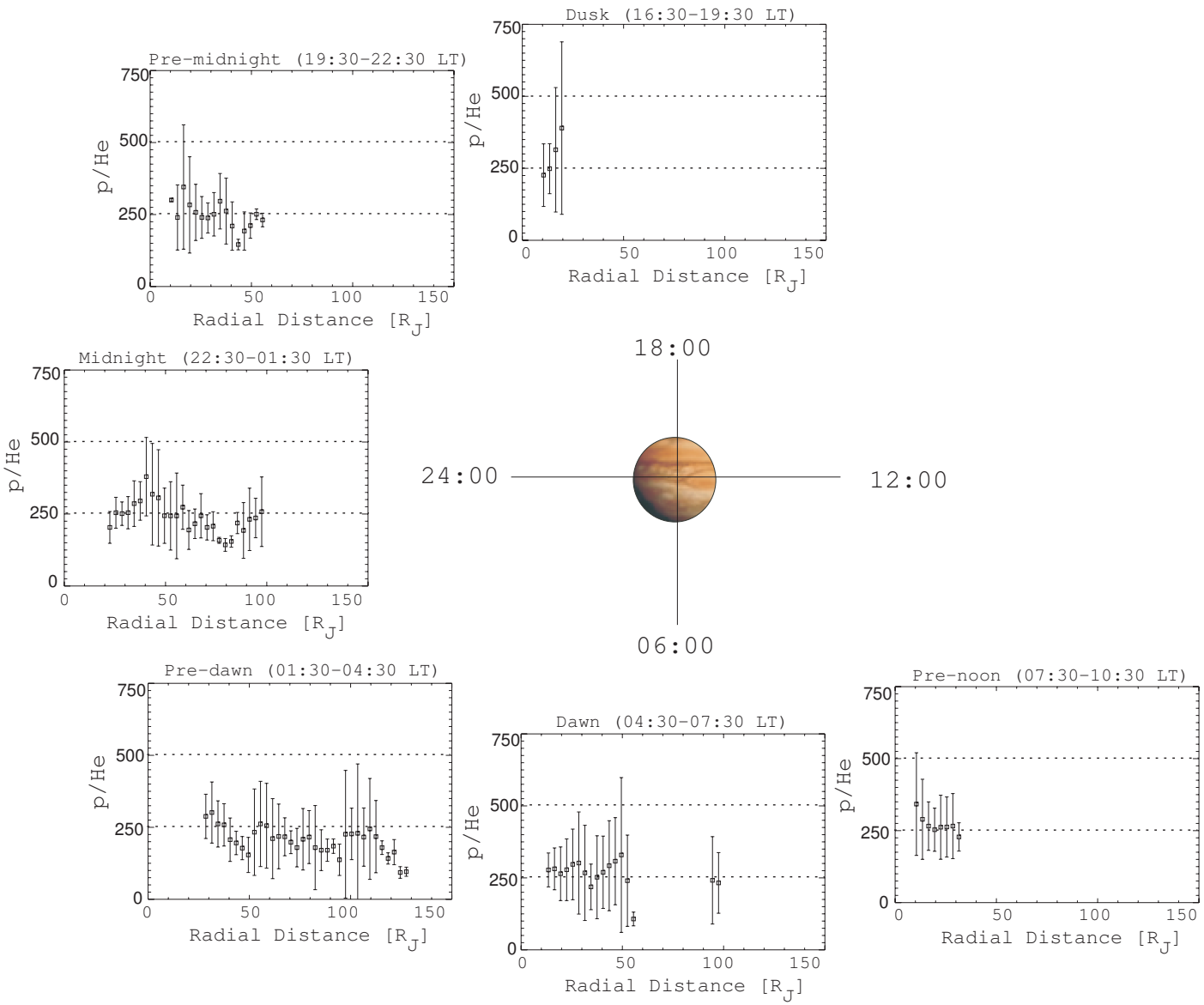


Figure 3.14: p/He ion abundance ratio, calculated at 185 keV/nuc averaged within 6 different local time sectors and over $3 R_J$ and plotted versus radial distance. The format is the same as Figure 3.11.

3.2.3 Ion composition during reconfiguration events

As mentioned in the previous section along the predawn sector of the magnetosphere an increase of the S/O, S/He and O/He relative ion abundance ratios is observed. In the present section it is shown that the profound enhancement of the heavy ion composition is associated with reconfiguration processes taking place in the Jovian magnetotail.

Figure 3.15 shows an example of the S/O ion abundance ratio for the time interval from 1996, day 265 to day 280, where energetic particle flow bursts are prominent (see Figure 1.8 and Krupp et al. (1998)). The red line indicates the level of the average ratio at the same local time and comparable radial distances taken from the orbits in the vicinity. In the same figure variations of the ion directional flow anisotropy and the south/north components of the magnetic field data are shown for the same interval. The changes in

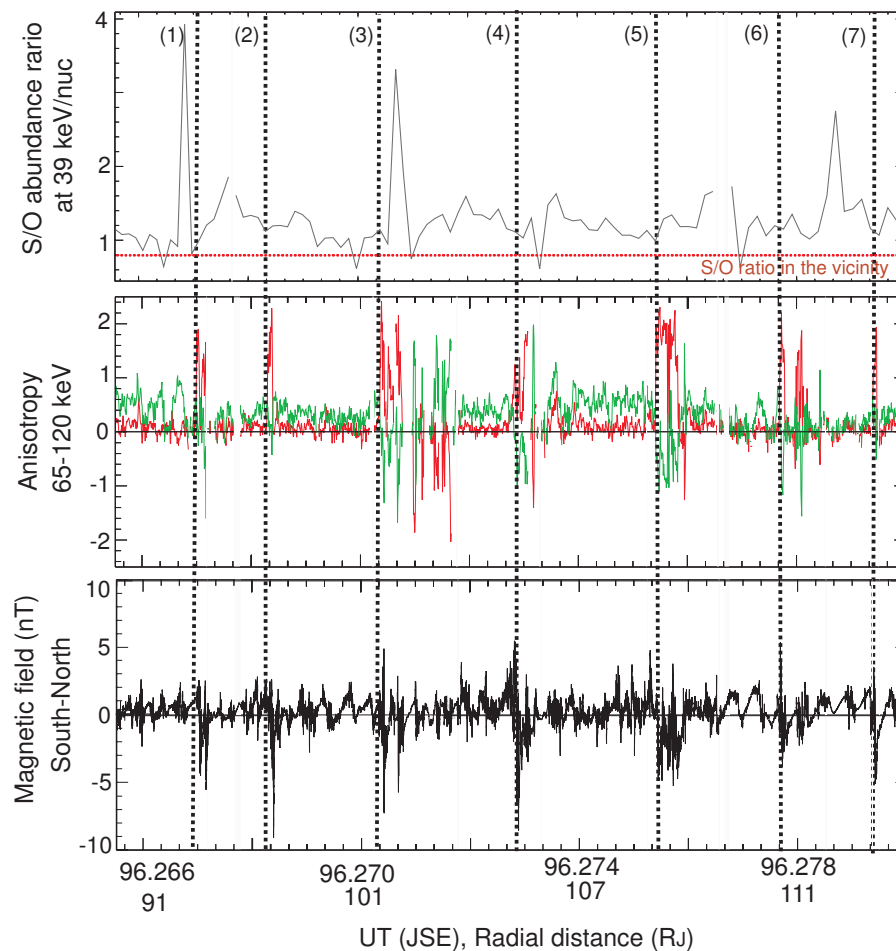


Figure 3.15: S/O ion abundance ratio (top) calculated at 39 keV/nuc as a function of time and radial distance for the time interval 1996, day 265-280. The red line indicates the level of the S/O ratio in the vicinity. Further shown are the first order anisotropies (middle) in the radial (red line) and corotational (green line) direction and the south-north component of the magnetic field (bottom) in high-resolution plotted for the same time interval. Vertical dashed lines indicate the onset of the disturbances. The lower two panels are taken from Kronberg et al. (2005).

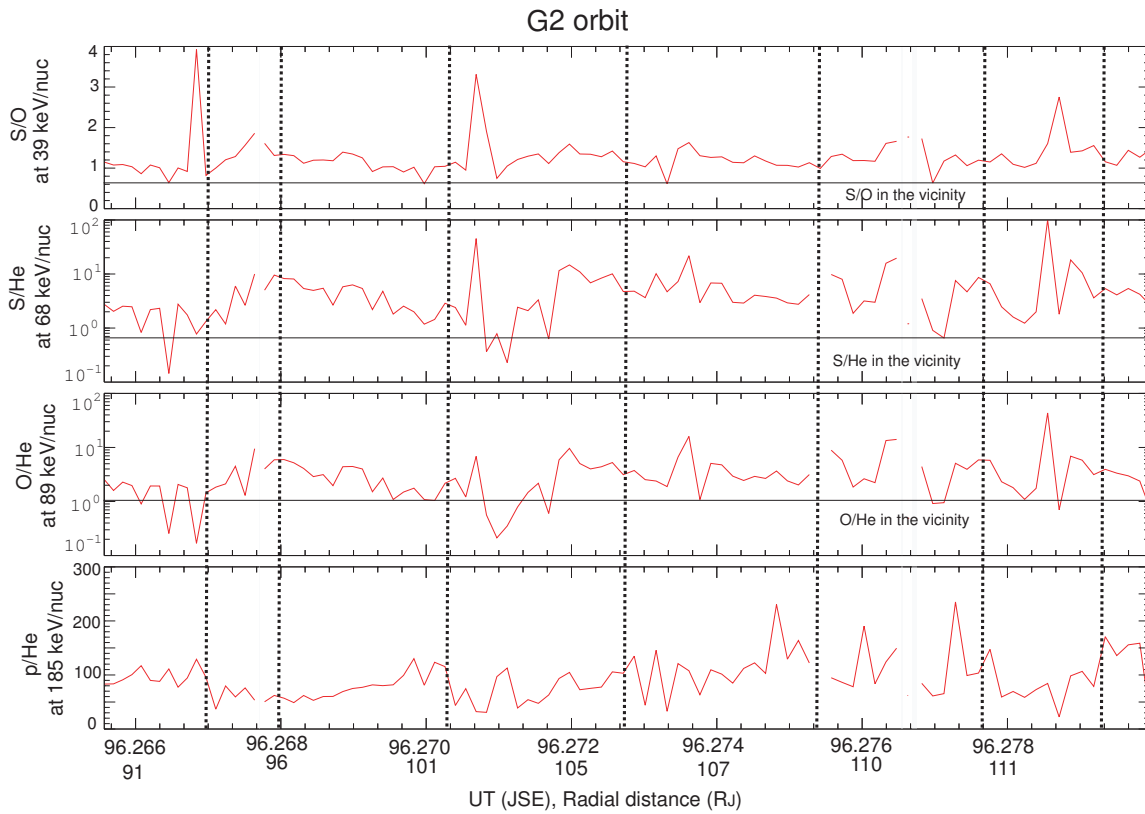


Figure 3.16: S/O, S/He, O/He and p/He ion abundance ratios (from top to bottom) calculated at 39, 68, 89 and 185 keV/nuc as a function of radial distance for the time interval 1996, day 265 to day 280. The horizontal lines indicate the level of the ratio in the vicinity and the vertical dashed lines the onset of the reconfiguration events.

the directional anisotropy (inward/outward) associated with changes in the polarity of the magnetic field component (from southward to northward) are indicative of burst events (Woch et al. 1998, 1999, Kronberg et al. 2005). The vertical dashed lines indicate the onset of these disturbances. It is evident that along this time interval the S/O relative abundance ratio is on average 1.2, much higher than the ratio of 0.6 observed in the vicinity. Moreover, a few individual spike-like enhancements in the ratio up to 4 coincide closely with the onset of the disturbances.

Figure 3.16 shows the S/O, S/He, O/He and p/He ion abundance ratios as a function of time and radial distance for the same time interval. Vertical dashed lines indicate the onset of the reconfiguration events and the horizontal line the ratio in the vicinity. It is obvious that not only the S/O but also the S/He and O/He ratio are enhanced up to one order of magnitude compared to the ratio in the vicinity, while p/He does not exhibit a clear behaviour.

To extend this study the ion composition is investigated for further time periods with bursts events. These events appear predominantly in the predawn sector along different Galileo orbits such as G2, E6 and G8 (1996 days: 262-296, 1997 days: 078-086, 1997 days: 152-168) (Kronberg et al. 2005). Figure 3.17 shows the relative ion abundance ra-

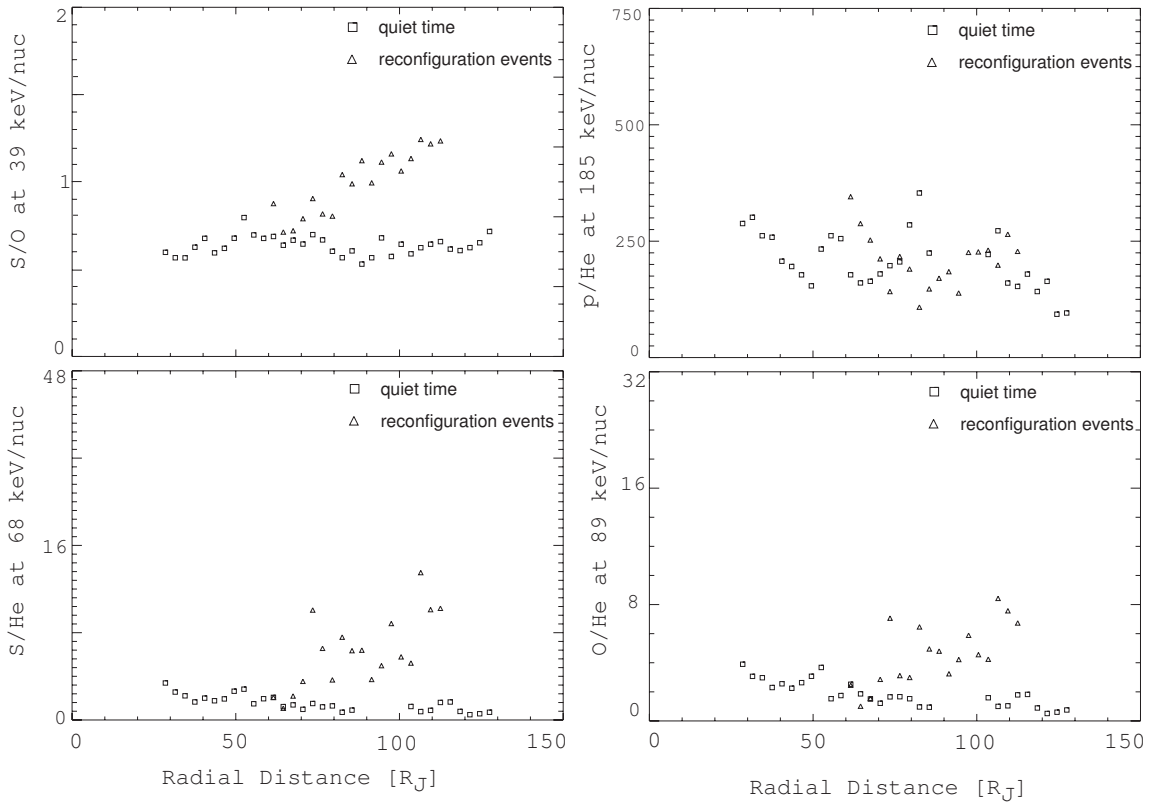


Figure 3.17: S/O, p/He, S/He and O/He abundance ratios at 39, 185, 68 and 89 keV/nuc, respectively, for the predawn sector (01:30-04:30 LT) averaged over $3 R_J$ and plotted vs the radial distance. The ratio along the reconfiguration events (triangles) (1996 days: 262-296, 1997 days: 078-086, 1997 days: 152-168) is plotted together with the ratio during the quiet time (squares).

tios of S/O, S/He, O/He and p/He for time periods with reconfiguration events (triangles) compared to the ratios observed in the quiet times in the same local time sector and at comparable distances (squares). The S/O, S/He and O/He ratios during the bursts time intervals exhibit clear enhancement. The enhancements are most pronounced for larger distances, reaching values of up to $\sim 70\%$, $\sim 330\%$ and $\sim 200\%$, respectively. The p/He ratio does not exhibit a similar clear increase. The present observations corroborate the increase of the S/O, S/He and O/He ion abundance ratios evident in the global abundances maps in the predawn sector (Section 3.2.2). It is demonstrated that the increase is associated with reconfiguration events taking place in the same region. In order to interpret the ion composition changes along the burst events in the predawn sector mass and charge dependent ion acceleration mechanisms are discussed in Chapter 4.

It should be noted that burst events appear also in the midnight sector of the magnetosphere along parts of the C9 and C10 Galileo orbits (Kronberg et al. 2005). Figure 3.18 shows S/O, S/He, O/He and p/He as a function of time and radial distance for a part of the C10 orbit, where reconfiguration events occur. It is obvious that no enhancements of the S/O, S/He, O/He and p/He compared to the vicinity are observed. The absence of com-

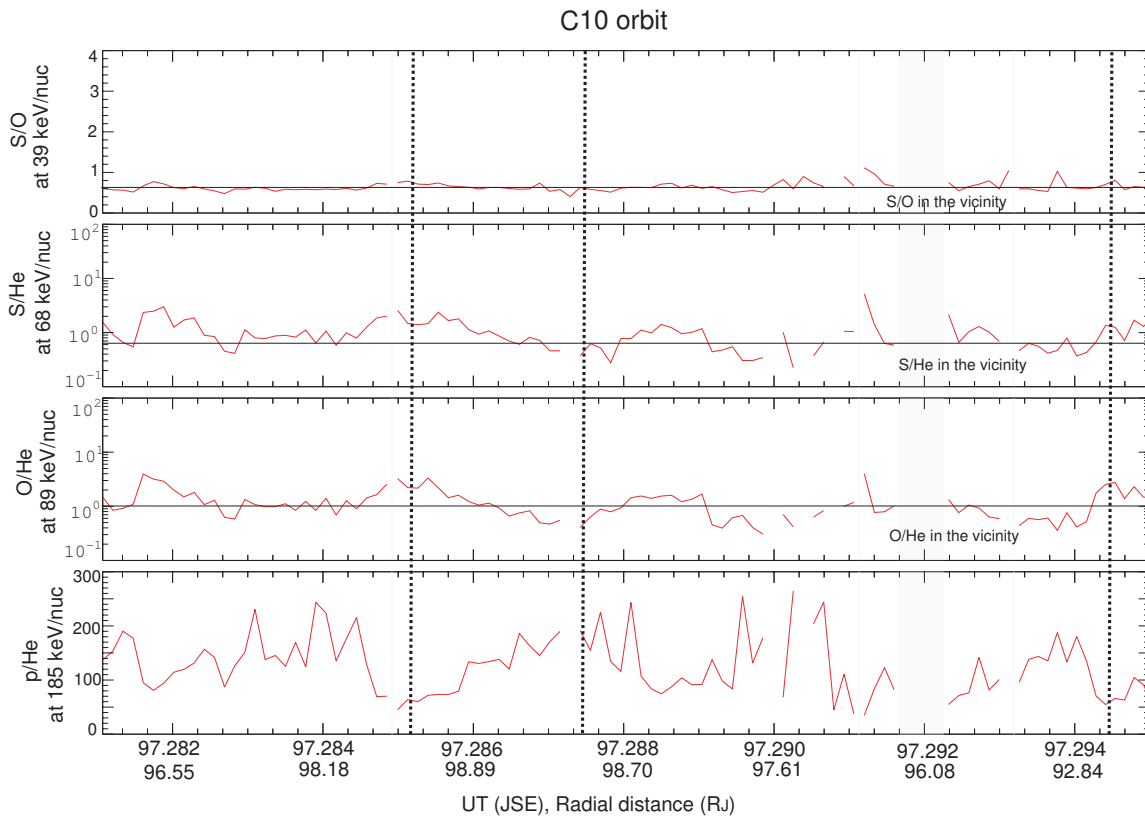


Figure 3.18: S/O, S/He, O/He and p/He ion abundance ratios (from top to bottom) calculated at 39, 68, 89 and 185 keV/nuc as a function of radial distance for the time interval 1997, day 281-295. The format is the same as in Figure 3.16

position changes along bursts events in the midnight sector is also discussed in Chapter 4.

Based on the present study it is concluded that composition changes along the predawn sector of the magnetosphere are associated with dynamical events taking place in the same region. The reconfiguration events in the magnetotail apart from being characterized by strong radial flow anisotropies, changes in the energy spectra of energetic particles and polarity changes in the magnetic field north-south component, are also accompanied by substantial enhancements of the heavy ion composition.

3.2.4 Temporal variations

The first 15 consecutive orbits of Galileo provide the unique opportunity to investigate temporal effects in the Jovian magnetosphere. Orbits that cover roughly the same local time and radial distance can reveal variations in time scales of several weeks. Figure 3.20 shows the ion abundance ratios of S/O, S/He, O/He and p/He, respectively for parts of the Galileo orbits E6 (solid line) and G8 (dotted line). The selected periods are shown in Figure 3.19 by red lines. These two Galileo orbits are chosen because they provide good data coverage in roughly the same local time sectors at comparable radial distances.

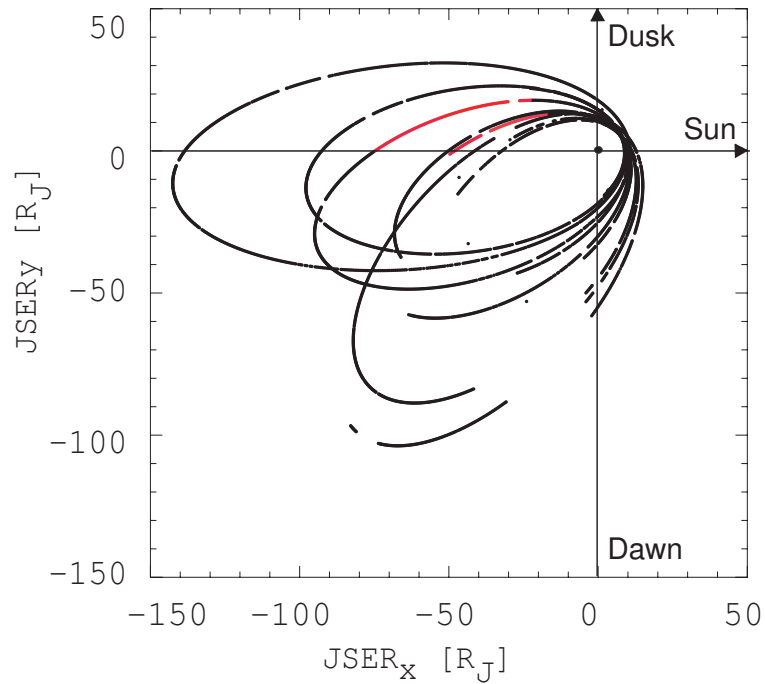


Figure 3.19: The same format as the left panel of Figure 3.4. Parts of the Galileo orbits E6 (1997, 052-057 days) and G8 (1997, 129-135 days) used for the investigation of temporal variations are indicated in red.

The ratios derived for the two different time intervals exhibit large variations. More specific, the S/O ratio for the two orbits differ by up to 0.4, heavy ions relative to helium exhibit variations up to one order of magnitude, while p/He exhibits less variations. The ratio values of the other 13 orbits in the same local time and radial distance range in-between. It should be noted that during the chosen time periods and up to $60 R_J$ special magnetospheric dynamic events like bursts which could be responsible for composition changes (see Section 3.2.3) are not observed. Large differences of sulfur and oxygen intensities up to one order of magnitude have been also reported for Voyager 1 (at $40-47 R_J$) and Voyager 2 (at $40-45 R_J$) measurements (Hamilton et al. 1981). However, the authors could not delineate whether they are due to temporal or local time variations. Additionally, comparison of the p/He ratio between the Voyager 1 and 2 missions at roughly the same energy range showed very good agreement (Krimigis 1983). From the present Galileo observations it is inferred that large temporal variations, which are most pronounced for S/O, S/He and O/He and less prominent for p/He, occur in the Jovian magnetosphere on time scales of weeks.

Figure 3.21 shows the sulfur and oxygen, as well as the proton and helium intensities in pairs corresponding to the abundance ratios of S/O and p/He as a function of radial distance for the same time intervals. All species intensities vary for the two orbits. Sulfur and oxygen intensities do not show large orbit to orbit differences up to $30 R_J$, however pronounced differences thereafter do exist. It is obvious that the ion intensities exhibit strong temporal variability, which affects of course the relative ion abundance ratios.

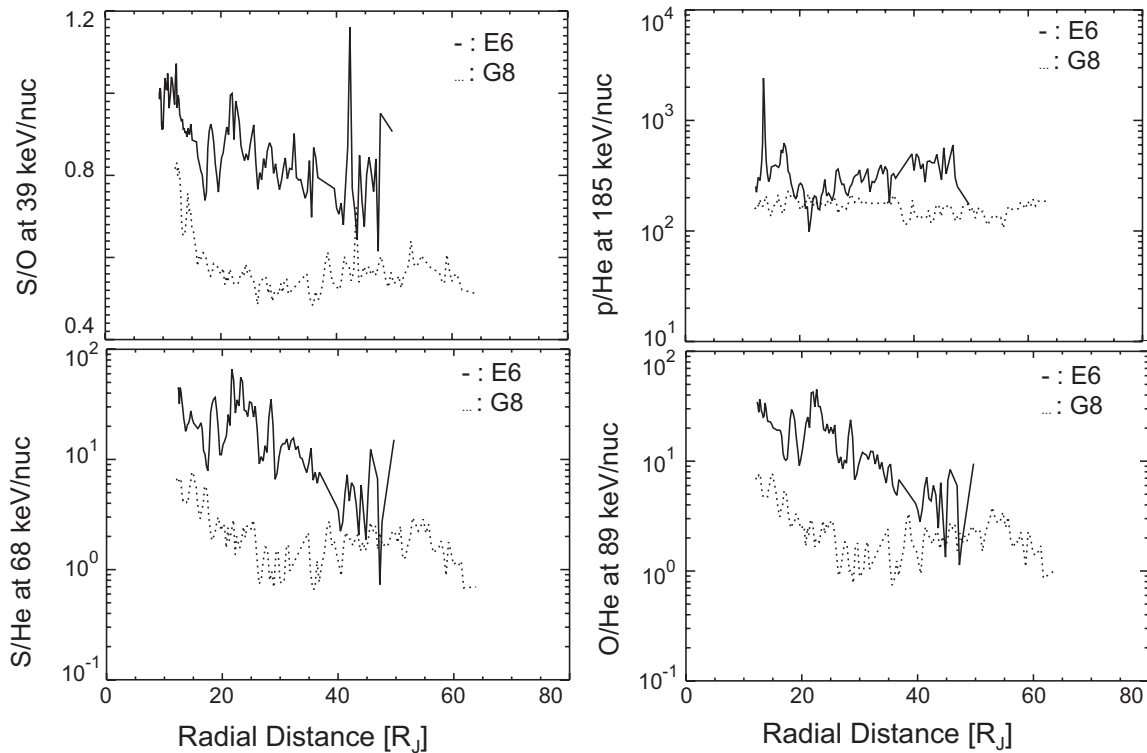


Figure 3.20: S/O, p/He, S/He and O/He abundance ratios averaged over 2 min/ R_J and calculated at 39, 68, 89 and 185 keV/nuc, respectively, in the dusk-midnight sectors of the Galileo orbits E6 (1997, 052-057 days) (solid line) and G8 (1997, 129-135 days) (dotted line).

Since Io is the major source of oxygen and sulfur the high temporal variability of the S/O ratio could be attributed to the variable emissions of the S/O neutral source ratio, which ranges between 0.25 and 0.58 (see Section 1.2.2). These ratio values can not be directly compared to abundance ratios as measured by the energetic particle instrumentation onboard Galileo. The Io torus neutrals are ionised, the newly created ions are then emitted at low energy (several eVs to tens of eVs) and they are transported and accelerated to keV. Even though between the neutral emissions and the energetic particle detection some steps are included the high temporal variability of the S/O neutral sources emissions could be a reason of the temporal variations of the ion abundance ratios at the energies of several keV/nuc. The high temporal variability of S/He and O/He ratio is not surprising since the heavy ions have an internal source compared to the external origin of helium. p/He less pronounced temporal variations could imply that also protons are to a large extent of solar origin. Apart from the origin of the species the observed temporal variability of the ion abundance ratios can be attributed to other reasons. The sulfur and oxygen intensities show strong orbit to orbit variations and also helium ions and protons show variations that are coherently observed in the same distance range. This suggests that time-varying acceleration processes could also contribute to the variation of the relative ion abundance ratios. 3-days modulations observed in the ion intensities and ion energy spectra, associated to the reconfiguration events in the magnetotail (Woch et al. 1998) are an evidence of time-varying processes taking place in the Jovian magnetosphere.

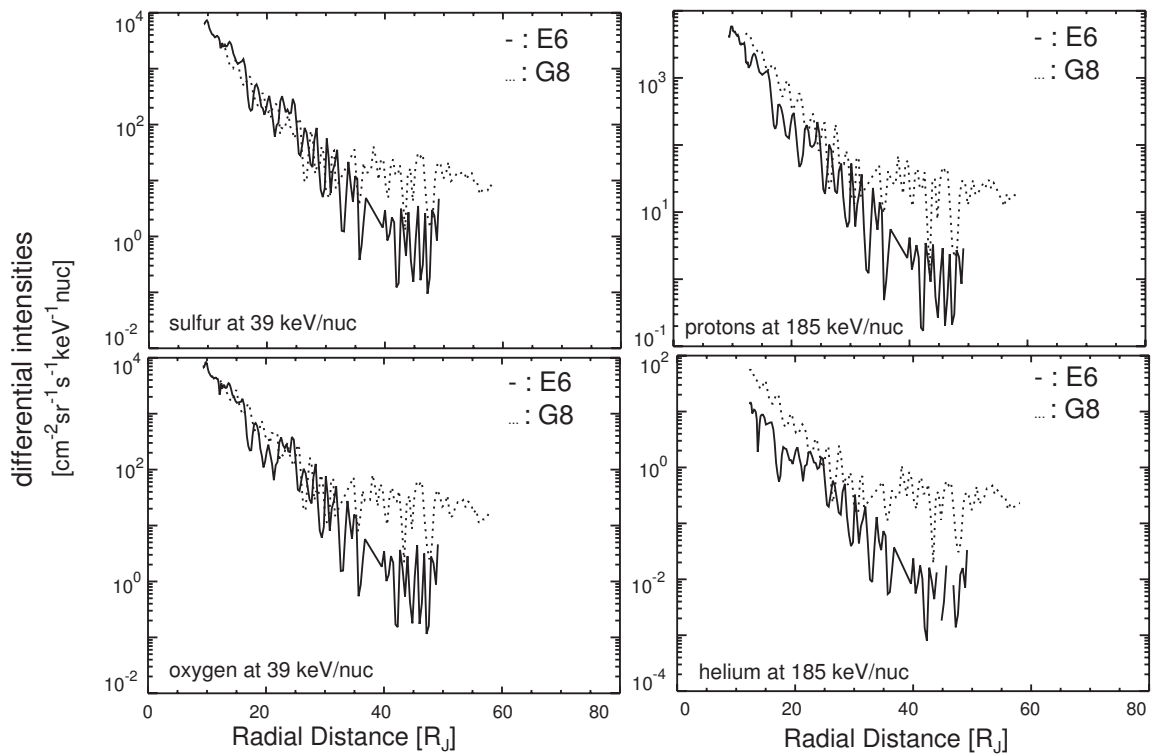


Figure 3.21: Sulfur and oxygen intensities at 39 keV/nuc (left side) and proton and helium intensities (right side) at 185 keV/nuc as a function of radial distance in the dusk-midnight sectors of the Galileo orbits E6 (1997, 052-057 days) (solid line) and G8 (1997, 129-135 days) (dotted line).

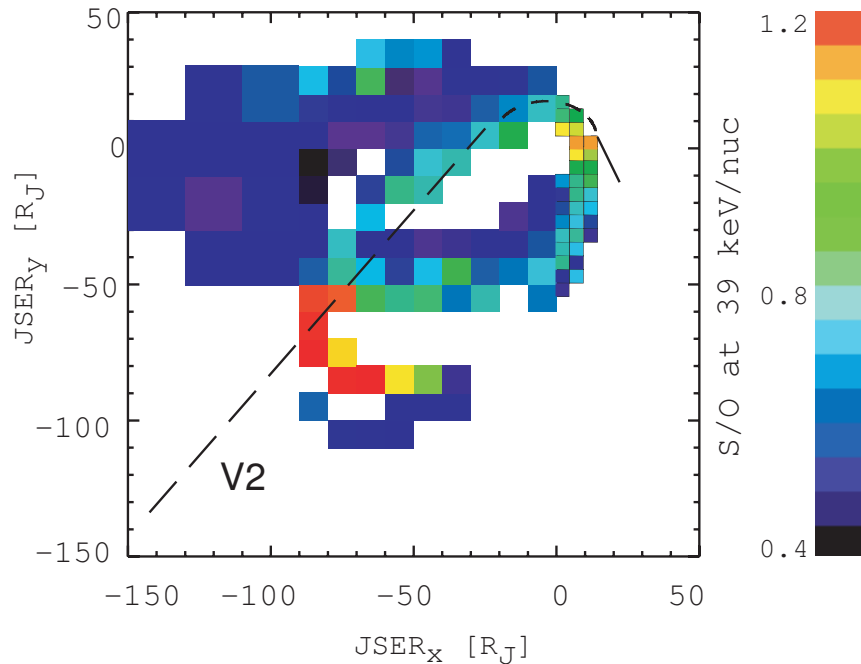


Figure 3.22: Color-coded global map of S/O calculated at 39 keV/nuc (from Figure 3.9) together with the Voyager 2 trajectory (dashed line). Bins cut by this trajectory are used for the comparison of Galileo with the Voyager 2 results.

3.2.5 Comparison with Voyager 2 results

In this section the ion abundance ratios measured onboard Galileo (1996 - 1998) are compared with those recorded onboard Voyager 2 (1979). The reason that the Voyager 2 mission is chosen among the other missions for comparison is that its outbound trajectory is covered by the first 15 Galileo orbits and its LECP instrument is appropriate for a comparative study of the relative ion abundance ratios of S/O, S/He, O/He and p/He.

To perform a thorough comparison of the abundance ratios for the two different experiments in terms of local time and radial distance the trajectory of Voyager 2 is drawn on top of the color-coded global map in Figure 3.22. The Voyager 2 trajectory is indicated by the dashed line. For comparison only the values from the binned boxes that overlap the Voyager 2 outbound trajectory are used. Additionally to the energy/nuc that fits best the Galileo energy channels (see Table 3.1) the ion abundance ratios are calculated at 800 keV/nuc so as to be within the Voyager 2 energy range (600 to 1150 keV/nuc). Figure 3.23 shows the ion energy spectra of sulfur, oxygen, helium and protons measured by EPD in pairs corresponding to the abundance ratios under study. The vertical lines indicate two different energies at which the ion abundance ratios are calculated for comparison and the grey area the Voyager 2 energy range. The 800 keV/nuc is almost at the lowest energy limit of the TOF energy channels and also within the Voyager 2 energy range. However, the Voyager 2 energy range includes the energy/nuc at which the energy spectra slope changes (see Section 3.1).

It should be noted that the EPD $\Delta E \times E$ (high energy) channels are seldomly available.

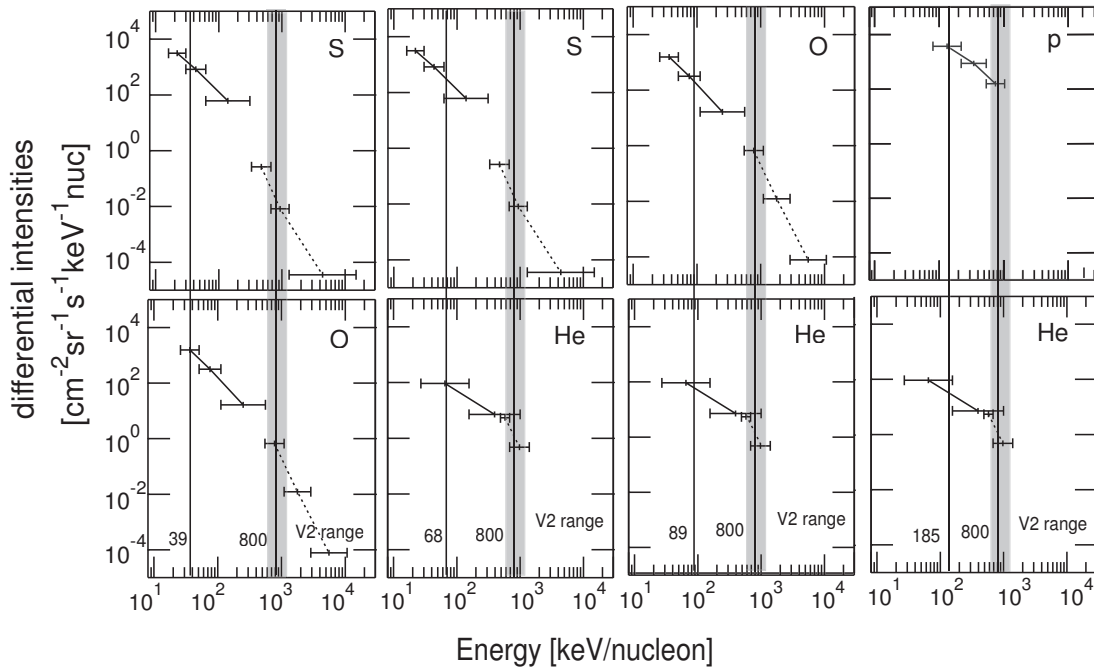


Figure 3.23: Ion energy spectra of sulfur, oxygen, helium and protons in pairs, corresponding to the abundance ratios under study S/O, S/He, O/He and p/He (from left to right) measured by the TOF (solid lines) and the $\Delta E \times E$ (dashed line) telescopes of the EPD instrument onboard Galileo. The sample is taken at $14.90 R_J$ and 08:08 LT. The vertical lines indicate the energy/nuc that fits best the TOF channels and the 800 keV/nuc, which correspond to the Voyager 2 energy range (shown by the grey area).

Therefore the comparison at 800 keV/nuc mainly relies upon an extrapolation of the EPD low energy channels to 800 keV/nuc. An example is shown in Figure 3.24. Ion energy spectra measured along the Voyager 2 outbound trajectory ($51\text{-}57 R_J$, $\sim 02:00$ LT) are compared with those measured onboard Galileo for the same local time and radial distance but in a different energy range. The comparison indicates that the ion energy spectra measured by Voyager 2 are softer (larger γ) than those measured by Galileo implying large discrepancies in the derived relative ion abundances. The softer spectra observed by Voyager 2 is in accordance with the softening in the spectra measured by the high energy channels of EPD presented in the Section 3.1.

The result of the comparison of the two missions for the S/O, S/He, O/He and p/He abundance ratios is shown in Figures 3.25, 3.26, 3.27 and 3.28 respectively. The triangles represent the abundance ratios measured onboard Galileo along the Voyager 2 orbital trajectory (of Figure 3.23) and the squares those measured onboard Voyager 2 in the energy interval of 600 - 1150 keV/nuc (Hamilton et al. 1981). The error bars of the ratios correspond to the standard deviation of the mean value in a given box, while those for the radial distance are given by the size of the box. The comparison of the ion abundance ratios is shown both for the EPD "best fit" energy/nuc (left panel) and for 800 keV/nuc (right panel).

The S/O ion abundance ratio measured onboard Galileo at both energy/nuc is higher

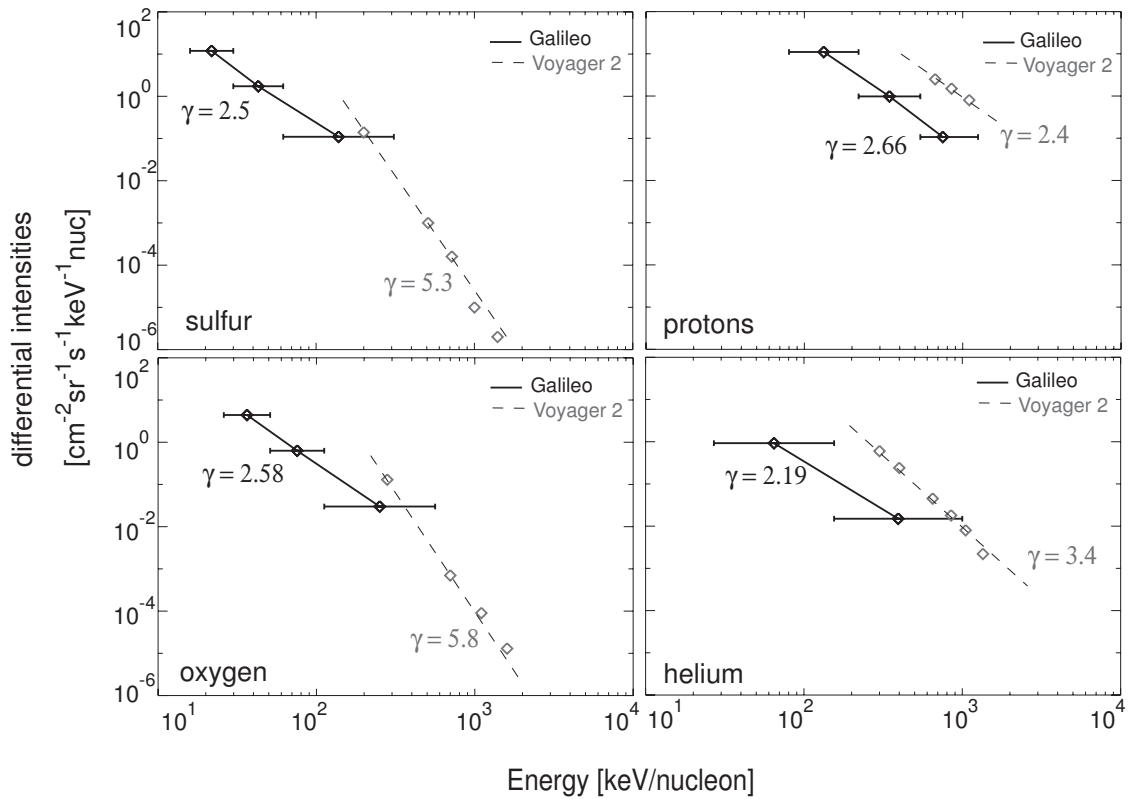


Figure 3.24: Ion energy spectra of sulfur, oxygen, helium and protons measured along the Galileo orbit C10 (at 52.82 R_J and 02.47 LT) and the outbound trajectory of Voyager 2 (at 51-57 R_J and 02:00 LT). Along that part of the C10 orbit, only measurements from the low energy channels are available; the Voyager 2 data are taken from Hamilton et al. (1981).

by a factor of 2 compared to those measured by Voyager 2. Thus, there is no indication for an energy dependence. This behaviour is expected since the slopes of the sulfur and oxygen energy spectra are parallel in good approximation. The S/He and O/He ion abundance ratios measured by Galileo are consistently higher than those of Voyager 2. The discrepancies are up to two orders of magnitude for the comparison at different energy/nuc and it is reduced to one order of magnitude for 800 keV/nuc. The p/He ratios measured by the two different experiments agree quite well especially when they are compared at the same energy/nuc. These observations confirm that the S/He, O/He and p/He ion abundance ratios exhibit a strong energy dependence resulting from the fact that the ion energy spectral slopes of oxygen, sulfur and protons are not parallel to the helium slope. In the following the comparison is done only at the same energy/nuc.

The Voyager 2 results are also compared with data from one individual Galileo orbit. For this comparison the Galileo G8 orbit is chosen, because along this orbit the ratio values are closer to Voyager 2. Figure 3.29 shows the relative ion abundance ratios derived along a part of the G8 (shown in Figure 3.19) and those obtained onboard Voyager 2. For this Galileo orbit the S/O, S/He and O/He ratios from Galileo are closer to the Voyager 2 results, compared to the average Galileo abundance ratios shown before. However, still

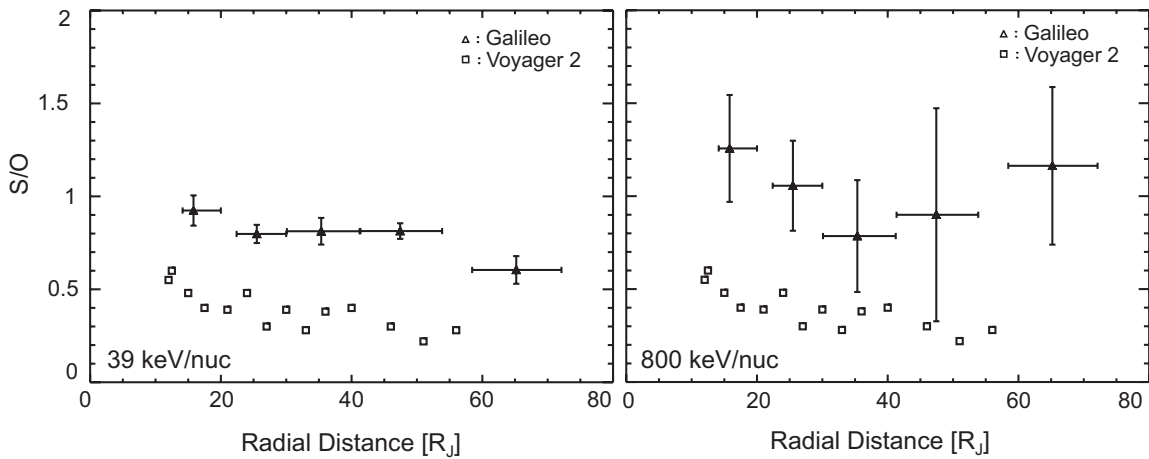


Figure 3.25: S/O abundance ratios measured by EPD onboard Galileo (triangles) at 39 keV/nuc (left panel) and extrapolated to 800 keV/nuc (right panel) along the Voyager 2 trajectory, compared with those measured by LECP onboard Voyager 2 (squares) at 600-1150 keV/nuc. The Voyager 2 data are taken from Hamilton et al. (1981) (Figure 1.15 of this thesis). The error bars of the ratios correspond to the standard deviation of the mean value in a given grid element, while those for the radial distance are given by the size of the grid element (adapted from Radioti et al. (2005)).

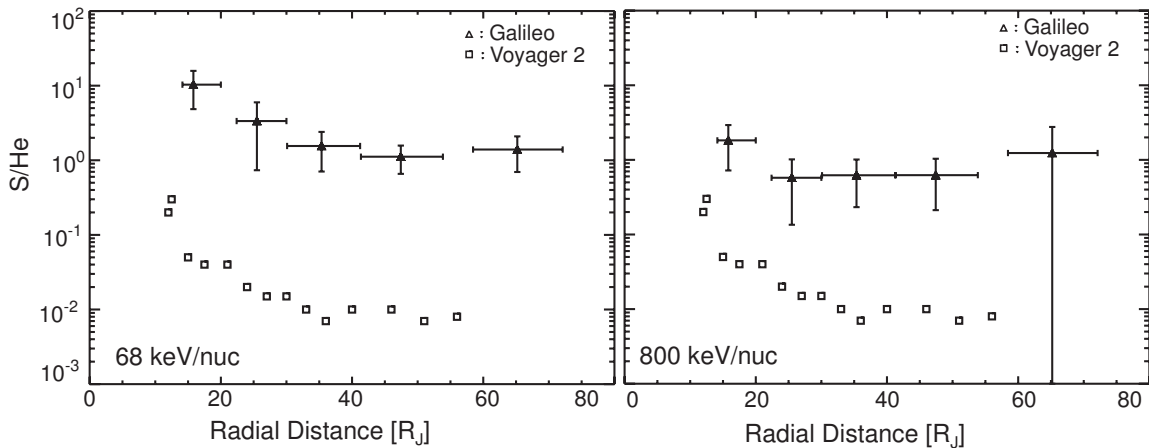


Figure 3.26: S/He abundance ratios (triangles) at 68 keV/nuc and at 800 keV/nuc (same format as Figure 3.26, adapted from Radioti et al. (2005)).

significant difference remains. The p/He ratio on this specific orbit again exhibits a very good agreement with Voyager 2.

Thus, the discrepancy of the ion abundance ratios especially those of S/He and O/He, measured by the two different missions 17 to 19 years apart, can possibly be attributed to temporal variations. It was already shown that temporal variations in the ion abundance ratios of up to one order of magnitude are present over time scales of several weeks (see Figure 3.20). It would not be surprise if additional variations on secular time scales of

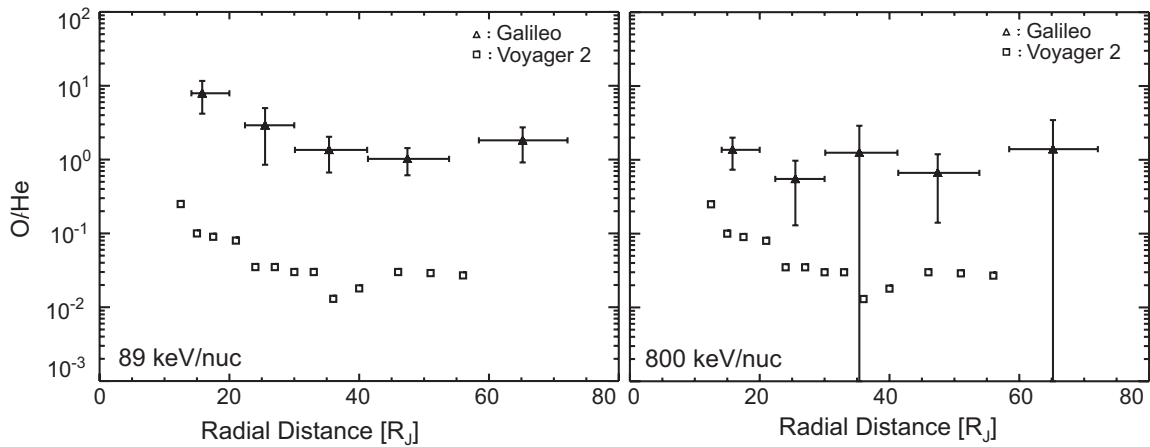


Figure 3.27: O/He abundance ratios (triangles) at 89 keV/nuc and at 800 keV/nuc (same format as Figure 3.26, adapted from Radioti et al. (2005)).

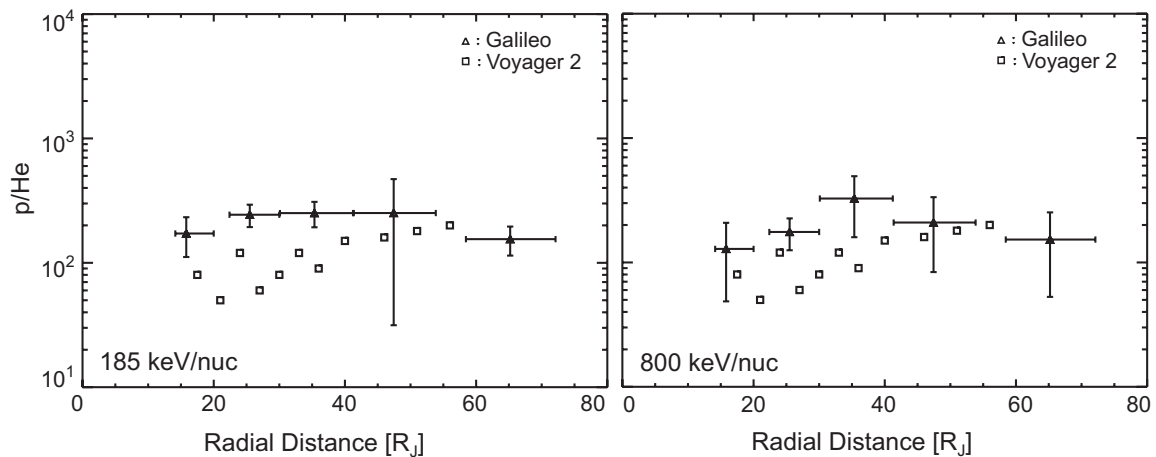


Figure 3.28: p/He abundance ratios (triangles) at 185 keV/nuc and at 800 keV/nuc (same format as Figure 3.26 and Figure 3.28, adapted from Radioti et al. (2005)).

several years exist, which together could fully account for the observed differences.

Figure 3.30 shows the oxygen and helium intensities at 800 keV/nuc, extrapolated from the Galileo measurements, as a function of time along the inbound and outbound trajectories of the first 15 Galileo orbits (grey crosses). In the same figure the oxygen and helium intensities measured on the Voyager 2 outbound trajectory are presented (black crosses). These values are the same as those used for the calculation of the ion abundance ratios in the energy range of 600-1150 keV/nuc. For comparison the Voyager ratios are plotted on top of both the inbound and outbound trajectories of the Galileo orbits. The ion intensities measured by Galileo exhibit large variations of up to 4 orders of magnitude. It is obvious that the oxygen fluxes measured onboard Voyager 2 are at the lower limit of the Galileo variations while the helium fluxes are at the higher limit. Thus the Voyager 2 several days measurements are well within the range observed during the Galileo 2 years

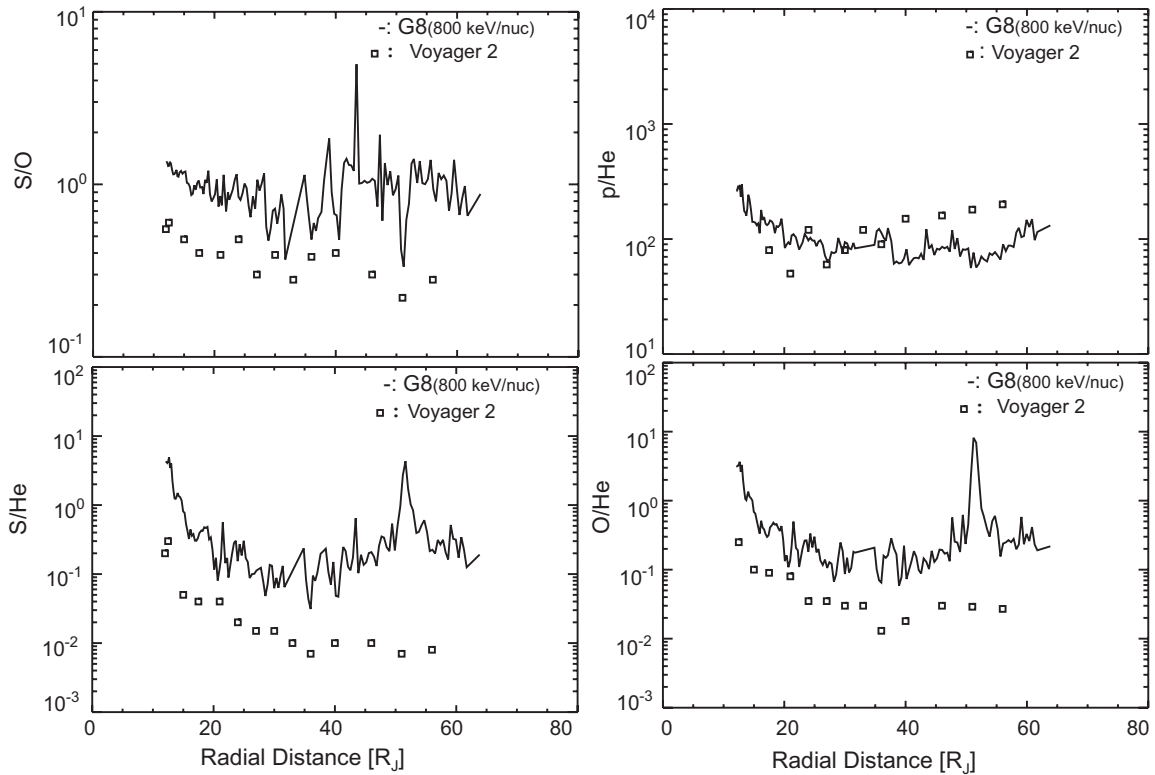


Figure 3.29: S/He, O/He and p/He (from top to bottom) abundance ratios from Galileo EPD along the dusk-midnight sector of the orbit G8 (1997, 129-135 days) (solid line). The data are extrapolated to 800 keV/nuc and plotted together with the Voyager 2 ratios (squares) for comparison. The Voyager 2 data are taken from Hamilton et al. (1981) (Figure 1.15 of this thesis).

coverage, furthering the notion that the Voyager 2 time was not an exceptional pass of extraordinary magnetospheric conditions.

However, large temporal variations in the ion intensities on week to year scales do exist explaining the large differences of up to one order of magnitude in the S/He and O/He ion abundance ratios compared at the same energy range for the two different experiments 17 to 19 years apart. Moreover, oxygen and sulfur ion intensities measured by the Voyager 1 and 2 missions showed discrepancies of a factor of 100 (see Section 1.4). The relatively small difference of the S/O ion abundance ratio of ~ 0.4 could be attributed to the temporal variability of the Io torus emissions (S/O neutral sources ranges between 0.25 to 0.58, see section 1.2.2) or temporal varying acceleration mechanisms, as mentioned in Section 3.2.4. The p/He ratio seems to vary less with time. It is shown that it exhibits only marginal temporal variations on scales of weeks for consecutive Galileo orbits (Section 3.2.4). p/He ratio measured by Voyager 1 and 2 missions roughly at the same energy range showed very good agreement. The present observation confirms the consistency of the p/He ratio on time scales of several years furthering the notion that protons and helium ions of several hundreds keV/nuc energy originate mainly from the solar wind, which constitute a fairly constant source on these time scales.

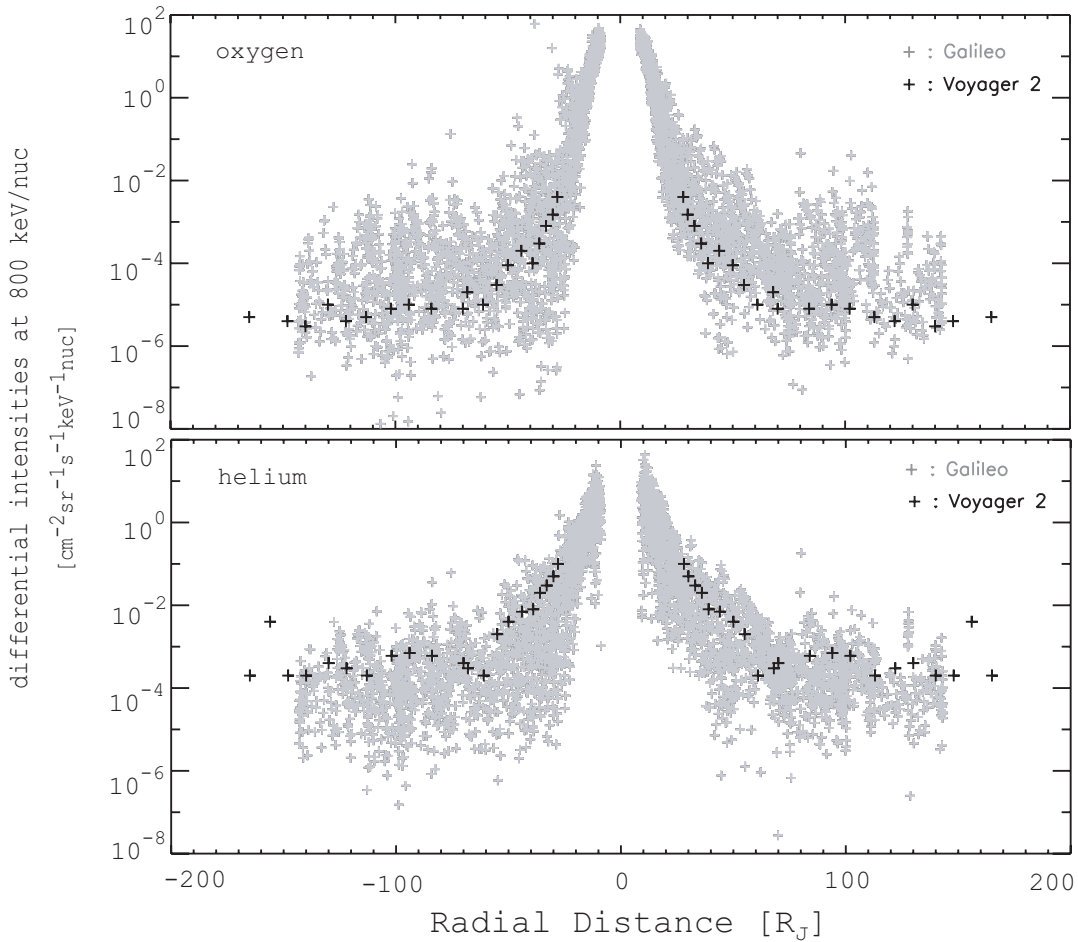


Figure 3.30: Oxygen and helium intensities extrapolated to 800 keV/nuc (grey crosses) as a function of radial distance along the inbound and outbound trajectories of the first 15 Galileo orbits. The data are dynamically averaged over 2 min/ R_J . The oxygen and helium intensities, at 600-1150 keV/nuc, (used also for the calculation of the ion abundance ratios) along the Voyager 2 outbound trajectory are shown for comparison (black crosses). The Voyager 2 data are taken from Hamilton et al. (1981) (Figure 1.15 of this thesis).

This is the first time that the ion composition has been compared for two different missions for the same local time and radial distance. Based on the present study it is concluded that the discrepancies of the ion abundance ratios between the two experiments can be attributed to strong energy dependence and/or temporal variations. The energy dependence of the ion abundance ratios is an essential issue indicating that ions are accelerated by a mechanism which affect different energy/nuc ranges differently, composing ion distributions that vary with energy. Additionally, the observed energy spectra break complicates the study of the energetic particle composition at various energies. In order to understand better the energy distribution of particles in the Jovian magnetosphere the observed ion energy spectra shapes are discussed in terms of ion stochastic acceleration by Alfvén waves in the next chapter.

3.3 Summary

The energetic particle composition of the magnetosphere of Jupiter is studied for the first time on a global scale based on the first 15 orbits of Galileo. The relative ion abundances of S/O, S/He, O/He and p/He are calculated, global maps are constructed and projected onto the equatorial plane. The S/O ratio ranges between 0.4 and 1.2. Though close to the S/O ratio of neutral sources (0.25 to 0.58) released from Io these values cannot directly be attributed to this source. Sulfur and oxygen are emitted from the Io torus at energies of a few eV. They are transported over large distances and accelerated to several 10s to 100s keV before they are detected by the Galileo spacecraft instrumentation. Moreover, the maps of sulfur, oxygen and protons relative to helium show that helium dominates over oxygen and sulfur at larger distances, while there is no clear trend for protons with respect to helium. This is consistent with the mixed origin of protons from the solar wind, Jovian atmosphere/ionosphere and the Europa gas torus.

A comparative study of the ion composition for different local time sectors is obtained for the first time. It is concluded that only minor local time asymmetries of the relative ion abundance ratios exist, with an exception of the predawn sector. Along this sector the S/O, S/He and O/He ratios are very much enhanced. The specific composition in this region is associated with reconfiguration processes taking place in the magnetotail. Based on the present study it is shown that apart from strong radial flow anisotropies, changes in the energy spectra of the energetic particles and polarity changes in the magnetic field north-south component, substantial enhancements of the heavy ion composition are characteristics of the reconfiguration events. In the next chapter ion acceleration mechanisms associated with the dynamics in the magnetotail are discussed to explain the observed ion composition.

The coverage of the first 15 consecutive orbits of Galileo provides a unique opportunity to investigate temporal variations. It is shown that pronounced variations of the S/O, S/He and O/He ratios on times scales of several weeks do exist. They can be attributed to the variability of the S/O neutral source emissions from Io, to the additional minor sources of oxygen and to the oxygen and sulfur internal origin compared to the external helium. The less variable with time p/He implies that protons originate to a large extent from the solar wind. However, apart from the ion origin, time-varying acceleration processes could also contribute to the time variability of the relative ion abundance ratios.

The global coverage of the Galileo trajectories enables a quantitative comparison with results of previous flyby missions for the same radial distance and local time. The Galileo results are specifically compared with those derived by the Voyager 2 mission not only for the same radial distance and local time but also for the same energy range. The large discrepancies derived from the comparison are attributed to temporal variations of the two missions 17 to 19 years apart and to the observed energy spectral shapes, which as it is shown introduces energy dependent effects on the ion composition. The next chapter discusses the ion energy spectra in the Jovian magnetosphere in terms of ion stochastic acceleration by Alfvén waves.

4 Ion acceleration mechanisms

This chapter discusses ion acceleration mechanisms related to the observed ion composition in a global scale but also locally for specific regions. Particularly, in the first section the observed ion energy spectra responsible for the energy dependence of the relative ion abundance ratios is discussed in terms of ion stochastic acceleration by Alfvén waves. In the second section the ion composition enhancements along time periods where reconfiguration events occur are investigated locally by two acceleration processes.

4.1 Ion stochastic acceleration by Alfvén waves

Energetic particle measurements onboard Galileo showed that ion energy spectra in the Jovian magnetosphere, in contrast to the magnetosphere of the Earth, cannot sufficiently be described by a kappa distribution (see Section 1.3). From the measurements it became clear that an additional cut-off at high energies of several 100 keV is needed. Additionally, any instrumental effects known up today that could be responsible for the production of the observed spectral shapes are excluded (see Section 2.3). Equation 1.7 is used to describe the ion energy spectra in the Jovian magnetosphere (Mauk et al. 1998). However, it is a functional form chosen to provide a good approximation of the measured ion fluxes vs. energy. It is derived empirically and lacks any physical meaning. In the current section the measured ion energy spectral shapes are discussed in terms of a model of ion stochastic acceleration by Alfvén waves initially introduced by Barbosa (1979).

The model describes a steady state process in which the ions are interacting with intense Alfvén waves propagating along the magnetic field. The effect of the turbulence is to scatter the particles in pitch angle fast enough to violate the first adiabatic invariant and isotropize the angular distribution. On a longer time scale the isotropic distribution is scattered in energy by stochastic acceleration.

A derivation of the equation describing the kinetic evolution of the distribution function due to interaction of ions with a spectrum of Alfvén waves propagating along the magnetic field was given by Barbosa (1979). A steady state ion distribution $N(E)$ as a function of energy per nucleon E is given by:

$$\frac{\partial N(E)}{\partial t} = D \frac{\partial}{\partial E} [E^{(\zeta+2)/2} \frac{\partial}{\partial E} (\frac{N}{\sqrt{E}})] - \frac{N}{\tau_{loss}(E)}, \quad (4.1)$$

where $N(E)$ is the total number density of the ionic species, ζ is the wave spectral index and $\tau_{loss}(E)$ is an energy dependent loss term, which determines the loss time.

Table 4.1: Initial parameters.

radial distance (R_J)	Alfvén velocity V_A (km/sec)	mean magnetic field B (nT)	$\frac{\Delta B}{B}$	correlation times T_0 (sec)
10	200	400	0.1	100-300
15	180	90	0.05	100-300
25	150	50	0.01	100-300

The diffusion coefficient D is given by:

$$D = \left(\frac{A}{Z}\right)^{\zeta-2} 2\pi\Omega_{cp} \frac{\delta B^2}{B^2} \frac{\zeta-1}{\zeta^2(\zeta+2)} \frac{E_A}{E_{mp}^{(\zeta-1)/2}}, \quad (4.2)$$

where A/Z is the mass-to-charge ratio of the ion, Ω_{cp} is the proton cyclotron frequency, $E_A = \frac{1}{2}M_p V_A^2$ is the Alfvén energy, $E_{mp} = E_A(\Omega_{cp}/\omega_0)^2$ is the maximum energy a proton can achieve by this process. It is assumed that a power-law spectrum of Alfvén waves $P(\omega) \propto \omega^{-\zeta}$ is propagating parallel to the magnetic field with spectral index ζ and $\delta B^2 = \int_{\omega_0}^{\infty} d\omega P(\omega)$ above a characteristic frequency (low-frequency cutoff) $\omega_0 = 2\pi/T_0$, where T_0 is the correlation time of the Alfvén wave turbulence.

The particles are considered to escape from the turbulent region in the manner of spatial diffusion through the Alfvén wave turbulence. Jokipii (1971) has described such a process in terms of spatial diffusion with an effective mean free path:

$$\lambda = \frac{4uE_A}{3DE^{\frac{\zeta-1}{2}}}. \quad (4.3)$$

The diffusive loss time for a region of spatial dimension L is then given:

$$\tau_{loss}(E) = \frac{3L^2}{4\lambda u} = \frac{9DL^2}{16V_A^2} E^{\frac{\zeta-3}{2}} = \tau_0 E^{\frac{\zeta-3}{2}}, \quad (4.4)$$

The boundary conditions are taken at an injection (threshold) energy $E_0 \approx E_A$. The solution of (4.1) then is

$$N(E) = N_0 \left(\frac{E}{E_0}\right)^p \frac{K_\nu(lE^q)}{K_\nu(lE_0^q)}, \quad (4.5)$$

where $N_0 = N(E_0)$ is the initial density, $K_\nu(x) \sim \left(\frac{\pi}{2x}\right)^{\frac{1}{2}} e^{-x}$ is the modified Bessel function, $l = \frac{2}{3-\zeta}(D\tau_0)^{-1/2}$, $p = \frac{2-\zeta}{4}$ and $q = \frac{3-\zeta}{2}$ are additional parameters.

The ion particle flux I is given by:

$$I = \frac{N(E)\sqrt{2E}}{4\pi}. \quad (4.6)$$

The theoretical spectrum as derived by the equation (4.6) can be directly compared to the ion energy spectra observations (Figure 3.2). The ion energy spectra are studied for three radial distances 10, 15 and 25 R_J , where both the low and high EPD energy

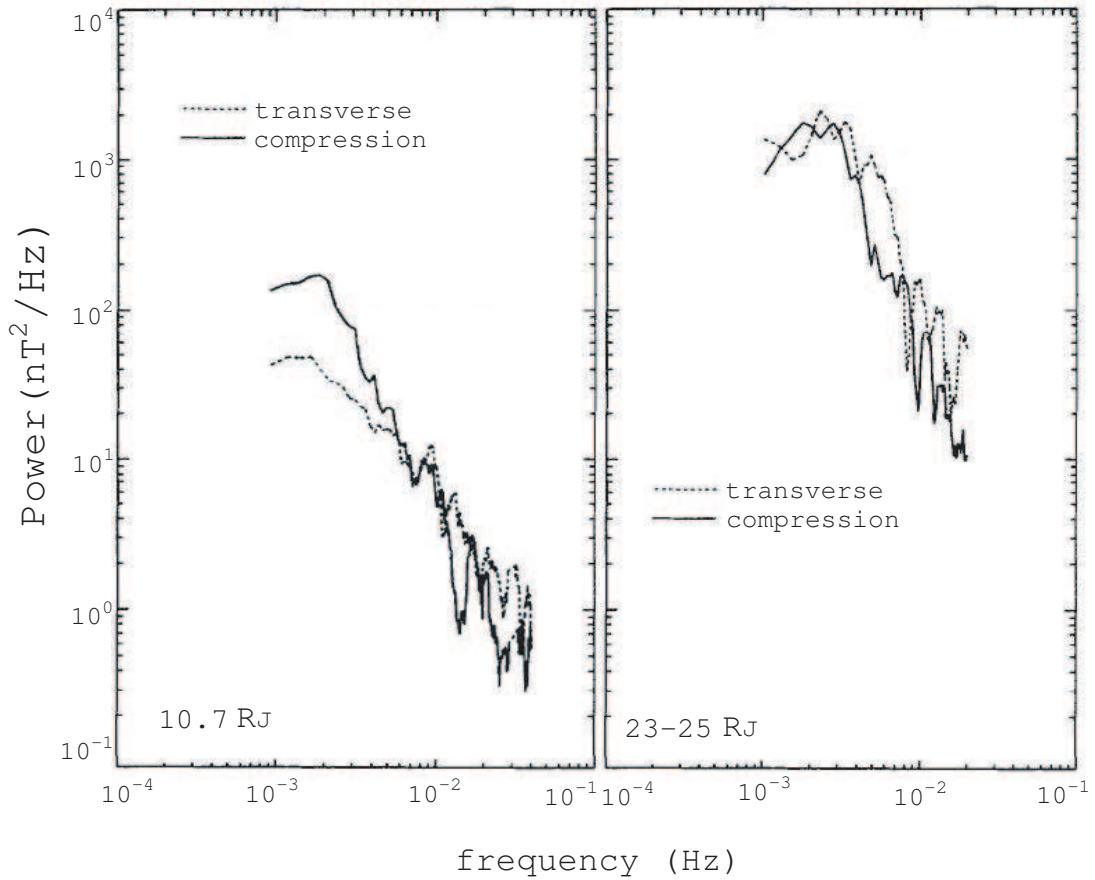


Figure 4.1: Power spectral density of the magnetic field seen on the G2 Galileo pass at radial distance of $10.7 R_J$ (left) and at the inner edge of the magnetodisk on the G2 inbound pass at radial distances 23 to $25 R_J$ (right) (from Russell et al. (2000)).

channels provide a good coverage. To derive the theoretical spectrum some initial parameters should be defined. Those that characterise the ion population are the mass A and the charge Z . The ion charge state Z is considered 1 for protons and is assumed to range between 1.2 - 1.8 for helium, 1.5 - 2.5 for oxygen and 2.5 - 3.5 for sulfur, which is consistent with the most probable charge states for the Jovian ion population (Geiss et al. 1992).

Figure 4.1 shows power spectral density of the magnetic field at radial distance of $10.7 R_J$ (left panel) and at 23 to $25 R_J$ (right panel), measured on board Galileo and are used as input parameters for the model. Initial parameters common for all species are summarised in Table 4.1 for each of the three radial distances 10, 15 and $25 R_J$. The Alfvén velocity V_A is determined by Barbosa et al. (1981), the mean magnetic field B is measured by the magnetometer onboard Galileo, the ΔB is estimated by the wave spectra observations (Russell et al. 2000) on the order of ~ 4 nT, forcing $\frac{\Delta B}{B}$ to vary with distance between 0.1 and 0.01. The correlation time T_0 is estimated to vary between 100 and 300

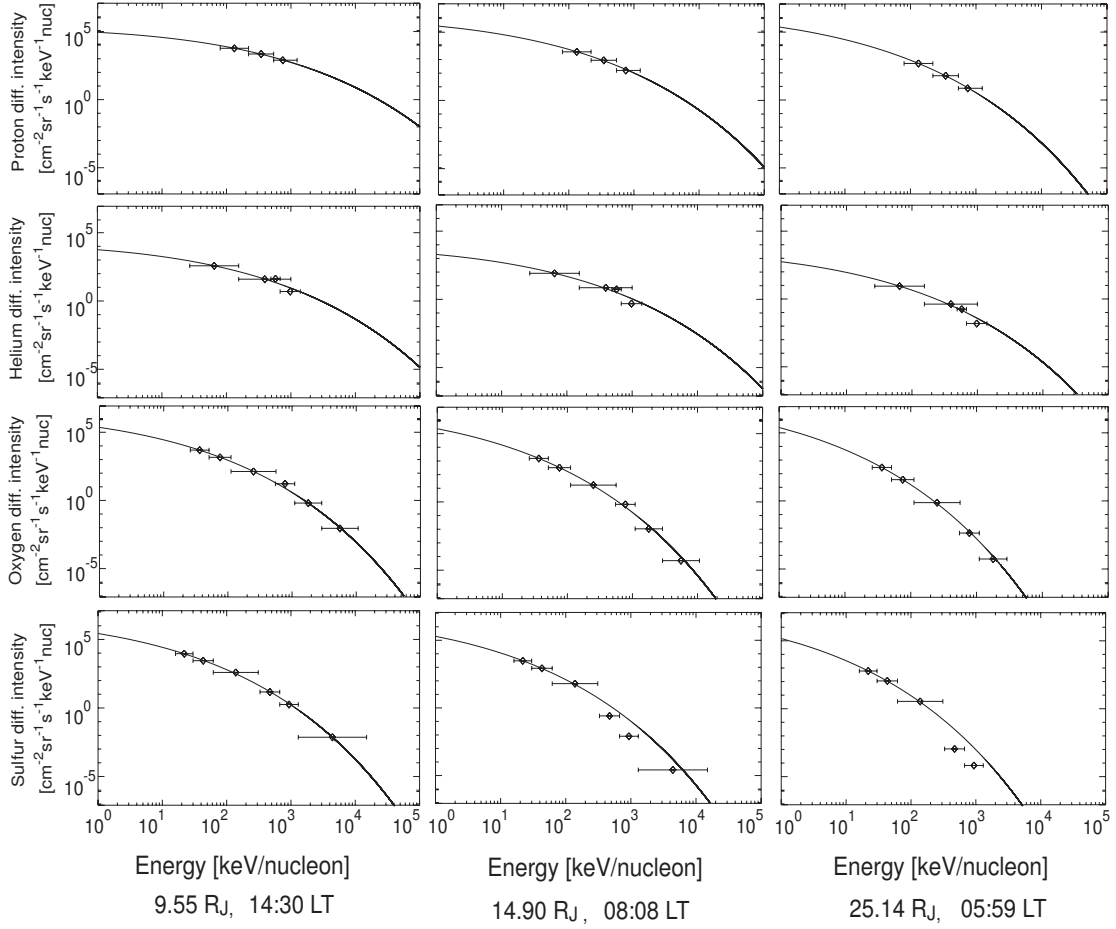


Figure 4.2: Theoretical ion energy spectra (curves) calculated for protons, helium, oxygen and sulfur (top to bottom panels) for three radial distances and local times. The triangles represent the measured ion energy spectra by Galileo EPD at $9.55 R_J$ (1998.088, 13:33 UT), $14.90 R_J$ (1997.127, 16:02 UT) and $25.14 R_J$ (1997.126, 14:36 UT) (left to right panels).

sec corresponding to the wave spectra flattening at $f_0 \sim 5 \times 10^{-3}$ Hz (Figure 4.1). The wave spectral index is a free parameter, its value will be determined by the model and compared with the observed wave power spectra of Figure 4.1. As a free parameter it is restricted to vary between $1 < \zeta < 3$ which is the regime that favours low-energy particle acceleration. ζ should be common for all species since it is a property of the Alfvén waves.

With these initial parameters the model is fitted to the data. The result is shown in Figure 4.2. The ion energy spectra for the four species and for three different radial distances are shown. The triangles show the measured values, while the curves the model fit. By fitting the model to all data points $\zeta = 2.65$ is determined as the best value. Two higher-energy data points of sulfur at distances $15 R_J$ and $25 R_J$, as shown in figure 4.2, are slightly declined from the theoretical curve. A smaller value of the wave spectral index of 2.55 would fit better the two sulfur data points, but would not be consistent with the rest.

Table 4.2: Parameters describing the ion population as derived by the application of the model for radial distance $10 R_J$, $15 R_J$ and $25 R_J$.

Species	initial density N_0 (cm^{-3})	length of the acceleration region L (R_J)	mean free path λ for 100 eV/nuc
$T_0 = 100 - 300$ sec			
<i>at $10 R_J$</i>			
Protons	$2.3 \cdot 10^6$	$9.5 \cdot 10^4 - 5.8 \cdot 10^5$	0.49 L
Helium	$1.7 \cdot 10^5$	$4 \cdot 10^4 - 2.5 \cdot 10^5$	0.58 L
Oxygen	$1.1 \cdot 10^7$	$1.3 \cdot 10^4 - 8 \cdot 10^4$	0.91 L
Sulfur	$1.4 \cdot 10^7$	$10^4 - 6 \cdot 10^4$	0.98 L
<i>at $15 R_J$</i>			
Protons	$1.1 \cdot 10^7$	$950 - 5.8 \cdot 10^3$	0.62 L
Helium	$7.6 \cdot 10^4$	$513 - 3.2 \cdot 10^3$	0.59 L
Oxygen	$2 \cdot 10^7$	150 - 913	1.02 L
Sulfur	$1.7 \cdot 10^7$	123 - 757	1.04 L
<i>at $25 R_J$</i>			
Protons	$2 \cdot 10^7$	108 - 661	0.69 L
Helium	$3.8 \cdot 10^4$	65 - 380	0.61 L
Oxygen	$5.8 \cdot 10^7$	22 - 109	1.1 L
Sulfur	$3.4 \cdot 10^7$	14 - 86	1.1 L

Previous studies of ion stochastic acceleration by Alfvén waves applied to protons, sulfur and oxygen ions in the Jovian magnetosphere (Barbosa et al. 1981, 1984, Barbosa 1994) used a wave spectral index of 2, which fitted the Pioneer and Voyager data. However, wave power spectra measured by the magnetometer instrumentation onboard the Galileo spacecraft near the equatorial plane for radial distances of $10.7 R_J$ and $23 - 25 R_J$ over a frequency range of $5 \times 10^{-3} \leq f \leq 4 \times 10^{-2}$ Hz, have shown that the wave spectral index is ranging between 2.3 and 2.7 (see Figure 4.1) in good accordance with the present results.

Apart from the wave spectral index other parameters are determined by the fit such as the particle's initial density N_0 and the length of the acceleration region along the flux tube L . These results are shown in Table 4.2.

All the expressions and values are only valid if the particle is considered collisionless with respect to Coulomb interactions with other particles along the acceleration region L . This requires that the scattering mean free path λ should satisfy: $\lambda \gtrsim L$. We calculate the mean free path (from equation (4.3)) for particles of 100 eV/nuc, considering that the acceleration starts at the energies of few hundreds eV and we compare it with the length of the acceleration region (see last column of the Table 4.2). The mean free path lies in a reasonable range compared to the length of the acceleration region ($0.5L < \lambda < 1.1L$) furthering the notion that the chosen initial parameters hold.

The length of the acceleration region is a parameter sensitive to the correlation time T_0 ,

$\frac{\Delta B}{B}$ and the ion mass per charge ratio A/Z . With the selected initial parameters for T_0 , $\frac{\Delta B}{B}$ and A/Z the length of the acceleration region L is varying between a few tens of R_J (for the heavy ions at $25 R_J$) up to several hundreds thousands of R_J (for the light elements at $10 R_J$) as shown in Table 4.2. These values could only be reduced to reasonable values between several R_J respectively several tens of R_J only if the wave spectra observations were consistent with $\frac{\Delta B}{B} \sim 0.5$ (Barbosa et al. 1981, 1984) or/and $T_0 \ll 100$ sec (Barbosa et al. 1981). However, such values seem not to be consistent with observations. Thus with the input parameters (according to the wave spectra observations) used above, the reproduction of the ion distributions at the three radial distances require a length of acceleration region, which is unrealistic for the Jovian magnetosphere.

It is concluded that even though the theoretical energy spectra curves fit very well to the data points, the large scale length required for the acceleration makes the above model insufficient to explain the observed ion energy spectra. The used model is unable to explain ion abundance variations at different regions. However, the process of ion stochastic acceleration by Alfvén waves might become applicable under some modifications or/and additions. One shortcoming of the present model is that only diffusion in energy is considered. A combined model of radial diffusion and ion stochastic acceleration by Alfvén waves has been used to explain the Voyager ion energy spectra at various distances (Barbosa 1994). An equivalent combined model could possibly explain the energy spectra break observed by Galileo for various distances. However, due to the limited knowledge concerning the exact shape of the ion energy spectra at various local times and at distances further away than $25 R_J$, such a model could not be thoroughly tested by observations at present.

4.2 Ion acceleration during the reconfiguration events

In this section the ion composition during periods where reconfiguration events occur is studied. These events are described in the introductory Section 1.2.2. Energetic particle measurements during these events are presented in Section 3.2.3. Prominent enhancements of S/O, S/He and O/He relative ion abundance ratios during the disturbed period are seen while no change for the p/He ratio is observed (see Figure 3.16). In this section two candidate mechanisms to explain the observed ion abundance ratios are investigated, associating the magnetotail dynamics with the ion composition. The first mechanism considers ion acceleration in the tail current sheet where ions are accelerated by the time-stationary dusk to dawn convection electric field in the current sheet. According to the second one, ion acceleration takes place during small scale variations of the south-north component of the magnetic field during the reconfiguration events, where an impulsive electric field induced during the disturbance plays a substantial role in the acceleration.

4.2.1 Acceleration in the current sheet

Non-adiabatic interaction of ions with the current sheet has been considered an important mechanism of particle energization in the magnetotail of the Earth (Speiser 1965) (see Section 1.3) and it has been used to explain ion composition enhancements during magnetic storms at Earth (Nosé et al. 2001). In the current section this non-adiabatic ion

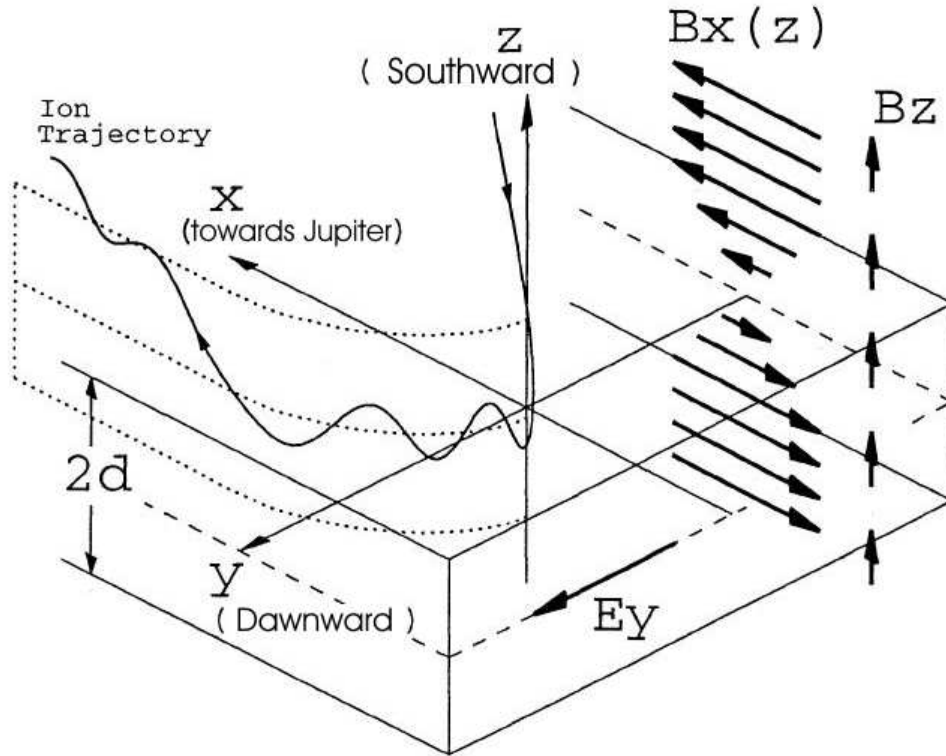


Figure 4.3: Schematic illustration of the current sheet model (Speiser 1965) for the case of Jupiter. Adapted from Speiser (1965).

acceleration process is evaluated as a possible mechanism to explain the observed ion abundance ratios of S/O, S/He, O/He and p/He during time periods where reconfiguration events occur. The particle acceleration by the time-stationary dusk to dawn electric field is studied for two cases: (a) for a thick current sheet during quiet times and (b) for a thinner current sheet just before reconnection occurs.

A description of the model applied to the magnetosphere of the Earth is presented in Section 1.3. The magnetic field is given by $\mathbf{B} = B_x \hat{x} + B_z \hat{z}$, where B_x is assumed to be constant at $|z| > d$ and to decrease linearly ($B_x \propto z$) at $|z| \leq d$, where d is the current sheet half thickness, while the B_z component of the magnetic field is considered constant and for the case of Jupiter is directed northward. The electric field E_y in the Jovian topology is directed from dusk to dawn. Figure 4.3 shows a schematic representation of the current sheet model for the case of Jupiter, where also a particle's trajectory is shown.

As it has been described in Section 1.3, when the particle's gyroradius becomes comparable or greater than the minimum curvature of the magnetic field lines then the first adiabatic invariant is no longer conserved in the vicinity of the current sheet. This requirement is fulfilled for the case of thermal ions at the magnetotail region ($\sim 80 R_J$). For example the gyroradius of O^{+2} of 100 eV/nuc in a magnetic field of $B = 4$ nT is estimated to be $r_g = 0.12 R_J$, which is larger than the $0.07 R_J$ estimated for the minimum curvature radius in that region (Goertz 1976).

In such field configuration the equation of motion for an ion with mass m and charge

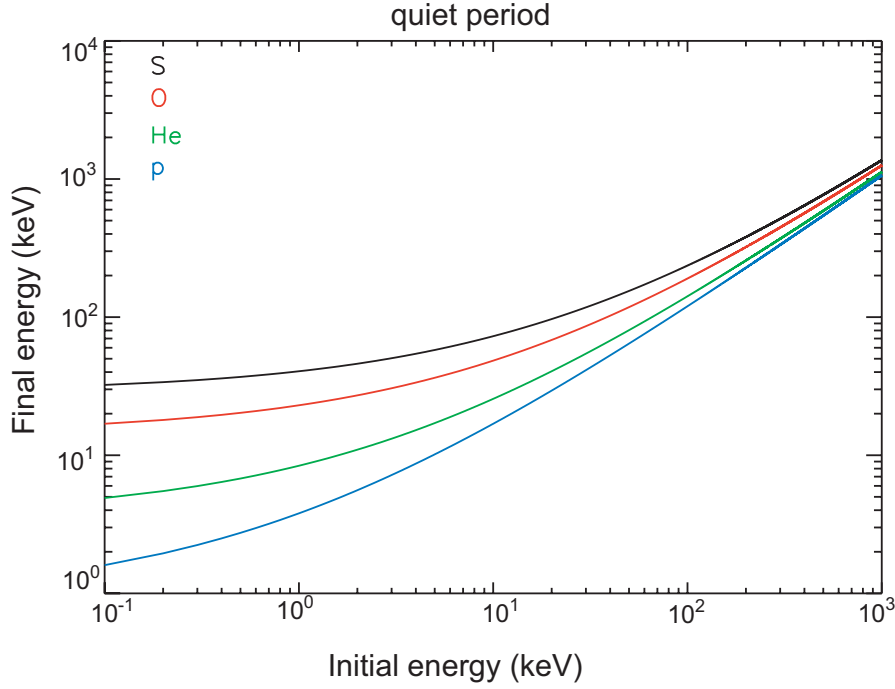


Figure 4.4: Sulfur, oxygen, helium and proton final energy (in keV) as a function of their initial energy (in keV) according to the current sheet acceleration model for $B_z = 1.2$ nT and $E_y = 0.25$ mV/m, corresponding to a quiet region.

state q is given by:

$$\begin{aligned}
 \frac{du_x}{dt} &= \frac{q}{m} u_y B_z \\
 \frac{du_y}{dt} &= \frac{q}{m} E_y + \frac{q}{m} (u_z B_x - u_x B_z) \\
 \frac{du_z}{dt} &= -\frac{q}{m} u_y B_x
 \end{aligned} \tag{4.7}$$

where the u_i is the i component of the ion velocity. Entering the current sheet the particle motion is no longer adiabatic, since the first adiabatic invariant is not conserved. The particles are oscillating in the z plane and are moving towards dawn accelerated by the dusk to dawn electric field. Since the B_z component of the magnetic field is non-zero the particle will eventually be ejected out of the current sheet. The velocity the particles are ejected at is given by the analytical solution of equations 4.7 (Speiser 1965):

$$u_1 = 2E_y/B_z + u_0, \tag{4.8}$$

u_1 and u_0 is the final and initial velocity of an ion, respectively. As discussed in the Section 1.3 the final velocity is independent of m/q . However, the time of the ejection $\tau_{ej} (\propto \frac{1}{B_z(q/m)})$ and the distance x the particles drift towards the planet is $x (\propto \frac{E_y}{B_z^2(q/m)})$ depend on m/q . Thus, ions with large m/q will be oscillating for longer time (τ_{ej}) and

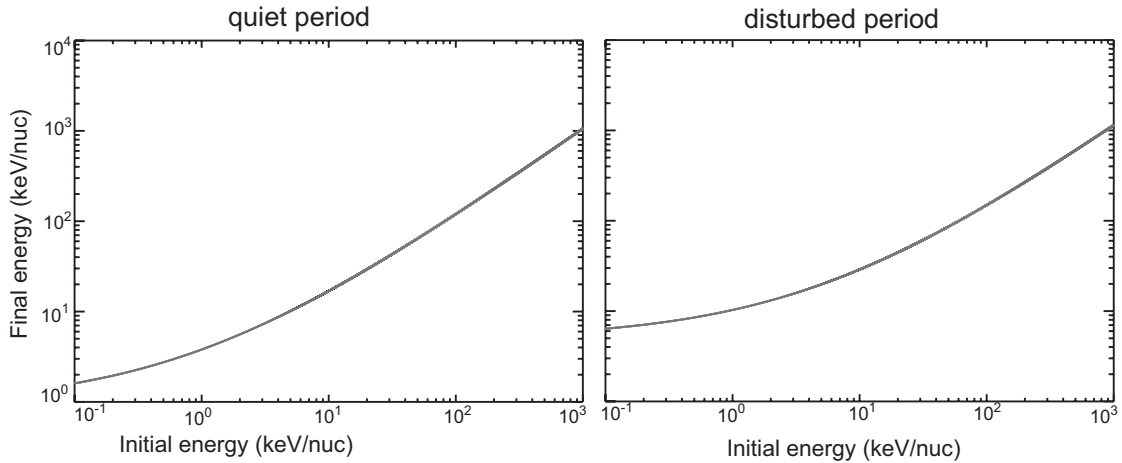


Figure 4.5: Ion final energy (in keV/nuc) as a function of their initial energy (in keV/nuc) for quiet time periods (left) and for periods with reconfiguration events occurring (right) as derived by the model for $B_z = 0.04$ nT, $E_y = 0.02$ mV/m and $B_z = 1.2$ nT, $E_y = 0.25$ mV/m, respectively.

drift further (x) than those with smaller m/q , but the ejected velocity of all ions will be the same.

To test how the different particles are energized the model is initially applied for model parameters $B_z = 1.2$ nT and $E_y = 0.25$ mV/m which correspond to a quiet period with a thick current sheet. The final particle energy (in keV) is calculated as a function of the initial one, shown in Figure 4.4 for the various species. It is evident that ions with larger mass gain more energy, since $E \propto m$. For example oxygen ions of initial energy 100 keV are accelerated to ~ 236 keV, while protons of the same initial energy are accelerated only to ~ 119 keV.

To evaluate if this ion acceleration mechanism is responsible for the observed ion composition the energy the particles gain should be ordered by energy/nucleon. The model is applied for the quiet period with a thick current sheet ($d \sim 2.5 R_J$) with model parameters $B_z = 1.2$ nT and $E_y = 0.25$ mV/m and for thinner current sheet ($d \sim 0.17 R_J$) just before reconnection occurs with $B_z = 0.04$ nT and $E_y = 0.02$ mV/m. The final energy is plotted as a function of the initial energy for the quiet and disturbed periods shown in the left and right panel of Figure 4.5, respectively. In the disturbed period all ions are accelerated stronger compared to that during the quiet time because of the larger ratio of $\frac{E_y}{B_z}$. However, the initial and final energy are ordered by keV/nuc and are the same for all ions independent of their m/q . Thus, no change in the relative ion abundance ratios after the acceleration can be produced and this model can not explain the observed composition changes in that region.

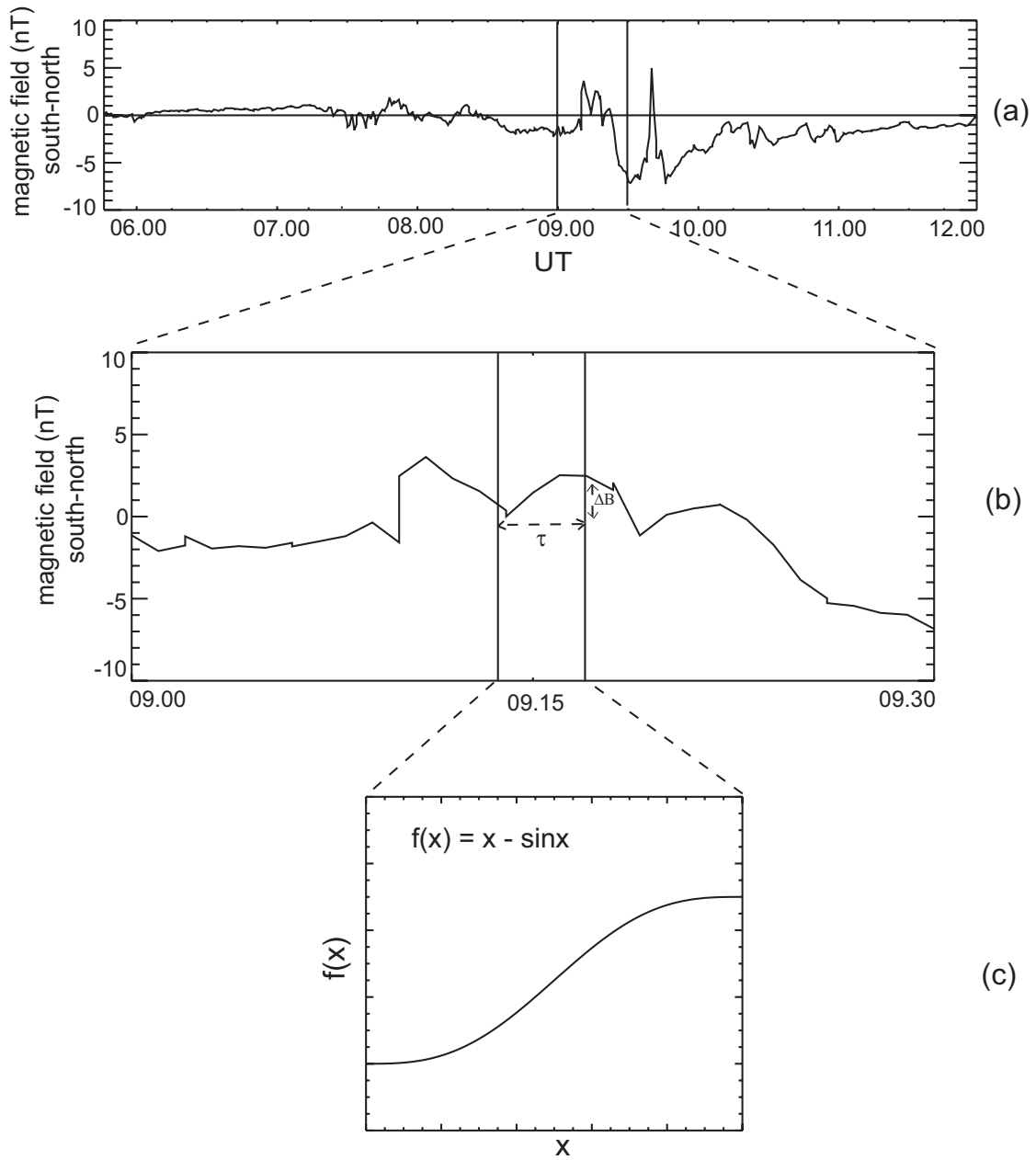


Figure 4.6: (a) High resolution of the south-north component of the magnetic field for the reconfiguration event (3) of Figure 3.15, (b) a close up view of the south-north magnetic field component for the time interval 9:00 to 9:30 UT (c) functional form of the selected south-north magnetic field variation.

4.2.2 Acceleration during small scale variations of the magnetic field lines

Apart from the acceleration in the current sheet due to the time stationary dusk to dawn convection electric field particle acceleration is evaluated for transient electric fields induced by the time varying magnetic field during the reconfiguration events.

During such events small-scale time variations of the south-north component of the magnetic field are observed. Panel (a) of Figure 4.6 shows a typical example of a reconfiguration event along the G2 orbit (event (3) of Figure 3.15), with a sequence of transient magnetic field variations. A characteristic example observed between 9.00 - 9.30 UT is shown in a close up view (panel (b)). These small-scale variations correspond to consecutive reconnection signatures, associated with plasmoid release (Kronberg 2006). The area marked in the panel (c) shows the time variation of the south-north magnetic field component, described by the functional form $F(x) = x - \sin x$.

Making use of this functional form, the north-south magnetic field component at a given time t is described in terms of the variation $\Delta B = B_m - B_0$ (where B_m and B_0 are the maximum and minimum values of the magnetic field component) and the duration τ for the time interval $0 \leq t \leq \tau$ as follows:

$$B(t) = -\frac{\Delta B}{2\pi} \left(\frac{2\pi t}{\tau} - \sin\left(\frac{2\pi t}{\tau}\right) \right). \quad (4.9)$$

The time-varying magnetic field induces an electric field in the vicinity of the plasma sheet. To calculate the induced electric field Faradays law is used.

$$\begin{aligned} \nabla \times \mathbf{E} &= -\frac{\partial \mathbf{B}}{\partial t} \Rightarrow \\ \frac{E(t)}{L} &= \frac{\Delta B}{\tau} \left(1 - \cos\left(\frac{2\pi t}{\tau}\right) \right) \Rightarrow \\ E(t) &= E_m \left(1 - \cos\left(\frac{2\pi t}{\tau}\right) \right), \end{aligned} \quad (4.10)$$

where E_m is the maximum electric field given by:

$$E_m = \frac{L \Delta B}{\tau}, \quad (4.11)$$

for the impulsive time scale τ and spatial scale L . The spatial scale is related to the length of the released plasmoid which is approximated by the duration of the magnetic field variation τ and the speed of the plasmoid u_{pl} (Kronberg 2006). Figure 4.7 shows the variation of the north-south component of the magnetic field (top) and the induced electric field (bottom) with time (for the time interval τ in arbitrary units), where the ΔB , the maximum electric field E_m as well as the duration of the magnetic field variation τ are indicated.

If the time scale of the duration of the induced electric field is comparable to the particle's gyroperiod then the particle can be accelerated non-adiabatically by the induced electric field. In case that $\tau \gg \tau_g$ the motion is adiabatic and the impulsive electric field does not energize the particle. To examine whether this non-adiabatic acceleration can generate the observed changes in the ion composition a modified model initially introduced by Delcourt et al. (1997) is used. This model is used to explain heavy ion enhancements during substorms in the terrestrial magnetosphere (Nosé et al. 2000a,b), events with characteristics similar to the reconfiguration events observed at Jupiter. Figure 4.8 shows a schematic illustration of the modified model used for the present study. Two orthogonal axis X and Y in the gyration plane are defined, which point towards Jupiter and towards dawn, respectively. The origin of phase is chosen $\psi_0 = 0$, which corresponds to particle

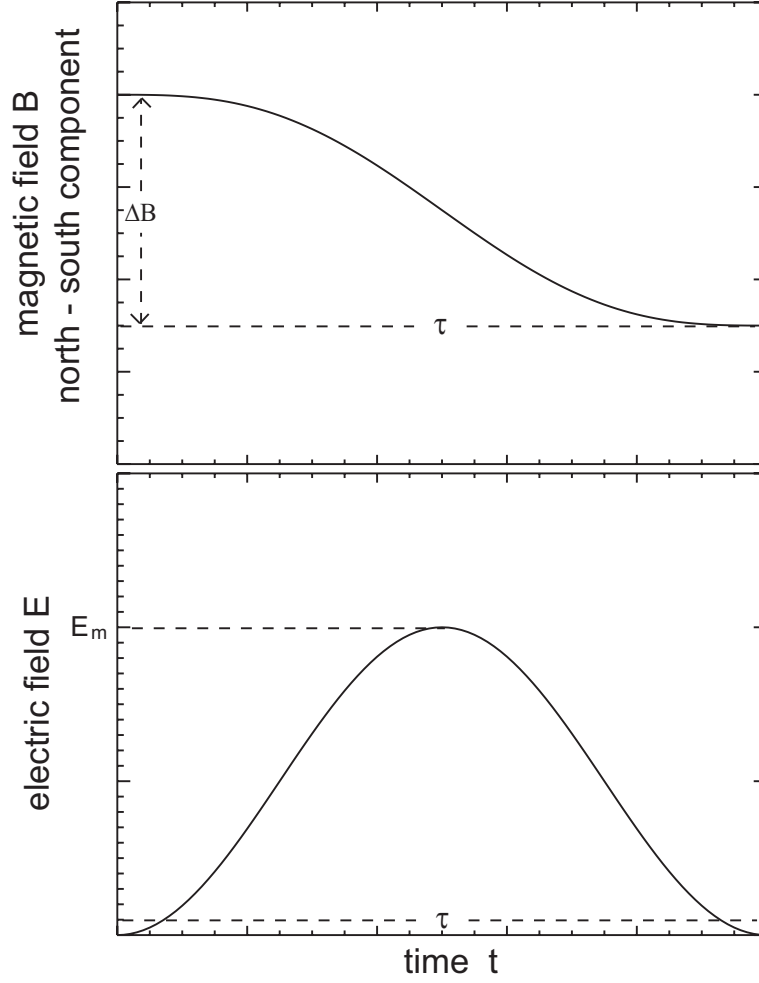


Figure 4.7: Top: North-south component of the magnetic field (top) and the induced electric field (bottom) as a function of time for the time interval τ as described by equations 4.9 and 4.10, respectively. The magnetic field variation ΔB , the maximum electric field E_m , as well as the duration of the magnetic field variation are indicated.

velocity V_0 in the Y direction. The dusk to dawn electric field $E(t)$ points in the +Y direction and based on the equation 4.10 can be described for a given time t :

$$E(t) = \begin{cases} E_m[1 - \cos(\frac{2\pi t}{\tau})] & : 0 \leq t \leq \tau \\ 0 & : t < 0, t > \tau \end{cases} \quad (4.12)$$

where E_m is the peak of the electric field and τ is the time scale of the magnetic field variation which corresponds to the duration of the impulsive electric field. For simplicity the magnetic field B is assumed to be uniform in the +Z direction and from now on B denotes the B_z component. The equation of motion in the X-Y plane is:

$$\begin{aligned} \frac{du_x}{dt} &= \frac{q}{m} u_y B \\ \frac{du_y}{dt} &= \frac{q}{m} E - \frac{q}{m} u_x B \end{aligned} \quad (4.13)$$

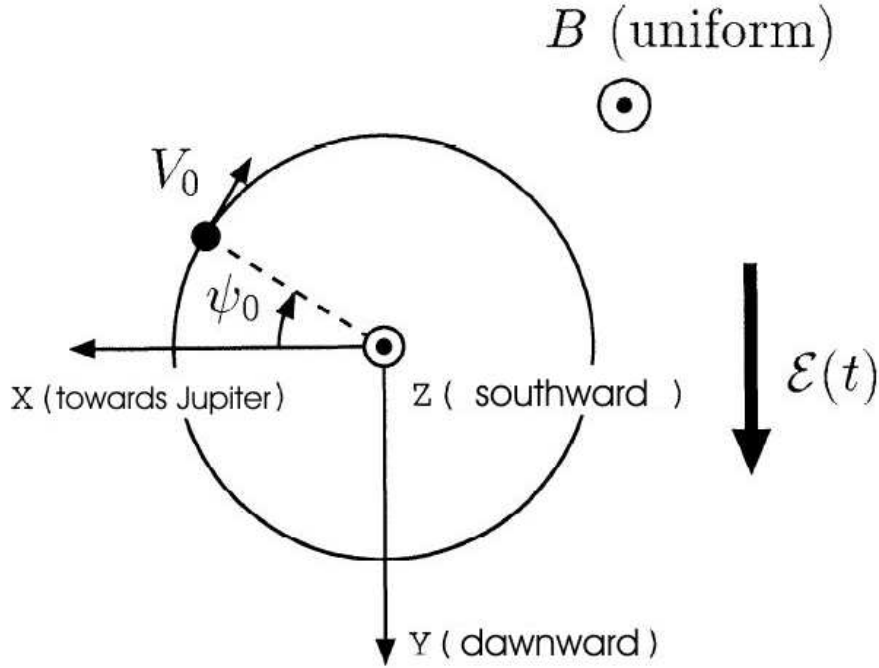


Figure 4.8: Schematic illustration of the simplified dipolarization model for the case of Jupiter (adapted from Delcourt et al. (1997)).

where m and q are the particle's mass and charge state, while u_x and u_y are the velocity in the X and Y direction. The equation of motion is solved under the oversimplification that the interaction is restricted to first cyclotron turn ($B = B_m$), considering only equatorial mirroring particles (Delcourt et al. 1997). Thus the particle's final ($t = \tau$) velocity V_1 is related to the initial V_0 by:

$$V_1^2 = V_0^2 \left[1 + \left(\frac{2E_m}{V_0 B_m} \frac{\sin \pi \chi}{\chi^2 - 1} \right)^2 + \frac{4E_m}{V_0 B_m} \frac{\sin \pi \chi}{\chi^2 - 1} \cos(\pi \chi + \psi_0) \right]. \quad (4.14)$$

where $\chi = \tau / \tau_g$ is the ratio of the time scale of the impulsive electric field to the gyroperiod of the particle.

The model is applied to the selected time interval shown in panel (b) of Figure 4.6. The magnetic field variation is $\Delta B = 3$ nT, it lasts $\tau = 3.4$ min and the spatial scale L is estimated to be $\sim 1 R_J$ (for $u_{pl} = 300 - 400$ km/sec, which corresponds to the local Alfvén speed). Thus the maximum electric field is calculated, from equation 4.11 to be $E_m \sim 1$ mV/m. These parameters are considered typical for such small scale variations (Kronberg 2006).

For an initial particle energy of 50 keV/nuc the final energy is calculated from equation 4.14 and is plotted as a function of χ in Figure 4.9. It is shown that the particle gains the maximum energy for $\chi \rightarrow 1$ in accordance with the previous statement that if the particle's gyro period τ_g is comparable to the impulsive time scale τ the maximum acceleration is obtained. If $\chi \gg 1$ the motion is adiabatic and the particles can not be accelerated by the impulsive electric field.

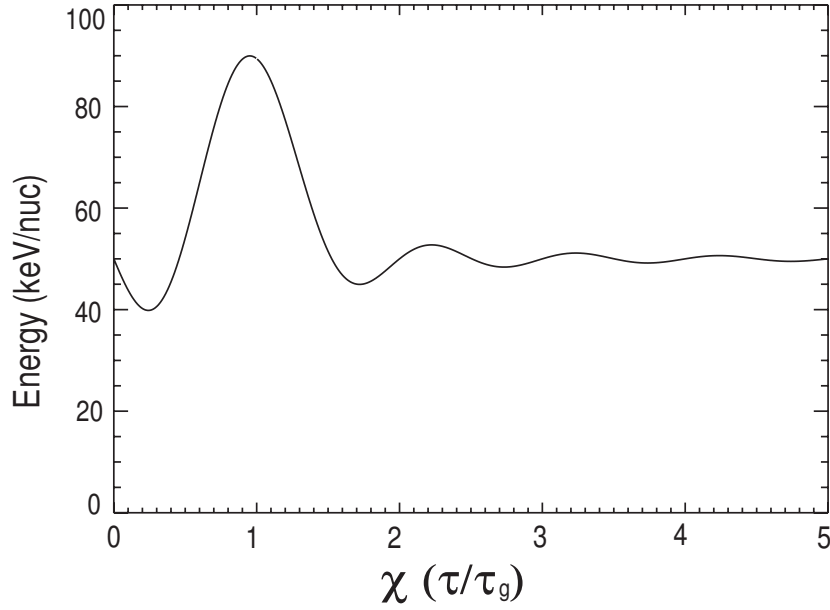


Figure 4.9: Particle's energy (keV/nuc) as a function of $\chi = \frac{\tau}{\tau_g}$ as derived by the model for initial energy 50 keV/nuc, magnetic field $B = 3$ nT and electric field $E_m = 1$ mV/m.

In order to investigate the effect of the impulsive electric field on the particle's energy the particle's gyroperiod is calculated. The gyroperiod depends on the mass m and charge q of the various particles and is given by $\tau_g = \frac{m}{qB}$ (sec/rad). As average charge states of the various ions in the Jovian magnetosphere are assumed 1.5 for helium, 2 for oxygen and 3 for sulfur. For magnetic field $B_m = 3$ nT the particle's gyroperiods are calculated as follows: $\tau_{su} = 233$ sec, $\tau_{ox} = 174$ sec, $\tau_{he} = 64.7$ sec and $\tau_p = 21.8$ sec. Figure 4.10 shows the modeled variation of the energy/nucleon for sulfur, oxygen, helium and protons as a function of the impulsive time scale τ for initial energy 50 keV/nuc. It is evident that different time scale variations of the electric field are needed to accelerate the various species. For the above model parameters, variations of 2 to 4 min duration accelerate more effectively sulfur and oxygen ions while variations less than 2 min can result in acceleration of helium and protons without energizing sulfur and oxygen.

Changes in the ion composition inferred by such an electric field can be studied by applying the model to ion energy spectra during a quiet time period. For this purpose a sample spectra taken on the C10 Galileo orbit at $\sim 80 R_J$ in the predawn sector (~ 1.40 LT) is used. These spectra can be regarded as being representative for quiet time spectra in this local time sector since no reconfiguration events were observed for an extended period of time. The observed ion energy spectra of sulfur, oxygen, helium ions and protons during the quiet time are shown in Figure 4.11 by black lines.

To calculate the ion energy spectra after the acceleration, Liouville's theorem is applied. According to this theorem during a dynamic evolution of the plasma (e.g. particle acceleration) the phase space density f remains constant. The differential particle flux $J(E, \alpha, \mathbf{r})$ per unit area at a given energy E , pitch angle α and position \mathbf{x} is connected with the phase space distribution $f(\mathbf{u}, \mathbf{r})$ as follows. The particle flux across a surface is

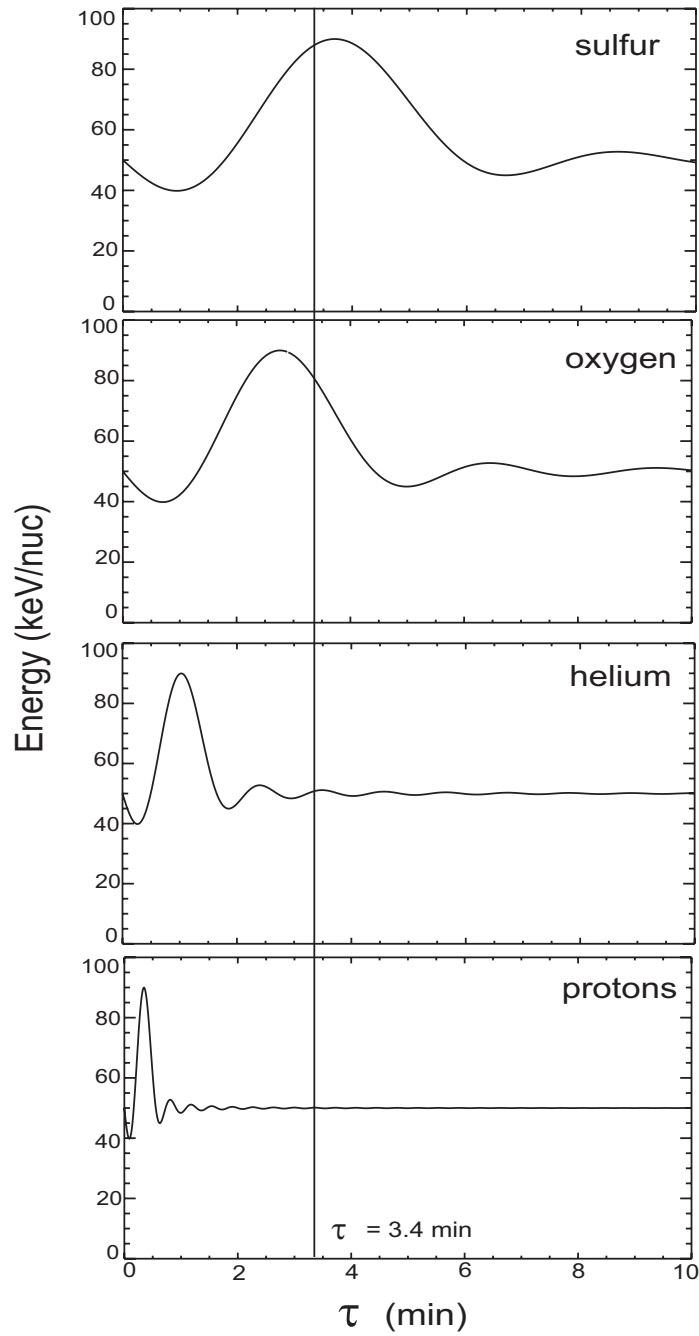


Figure 4.10: Energy (keV/nuc) of sulfur, oxygen, helium ions and protons as a function of the time scale of the magnetic field variation τ (min) as derived by the model for initial energy 50 keV/nuc, magnetic field $B = 3$ nT and electric field $E_m = 1$ mV/m. The vertical line indicates an observed value of the time scale of the magnetic field variation, $\tau = 3.4$ min.

given by the number density times the velocity component u :

$$J(E, \alpha, \mathbf{r}) = udn, \quad (4.15)$$

where the number density of particles dn in a velocity interval du and a solid angle $d\Omega$ is:

$$dn = fu^2dud\Omega. \quad (4.16)$$

From equations 4.15 and 4.16 it follows:

$$J(E, \alpha, \mathbf{r})dEd\Omega = f(u_{\parallel}, u_{\perp}, \alpha, \mathbf{r})u^3dud\Omega \quad (4.17)$$

using $dE = mudu$ equation 4.17 becomes:

$$J(E, \alpha, \mathbf{r}) = \frac{u^2}{m}f(u_{\parallel}, u_{\perp}, \alpha, \mathbf{r}) \quad (4.18)$$

Equation 4.18 relates the measured particle flux in a certain energy interval to the velocity distribution function of the measured particles. From Liouville's theorem for a given pair of differential particle flux J_1 and J_2 and velocity u_1 and u_2 it holds:

$$f = const \Rightarrow \frac{J_1}{u_1^2} = \frac{J_2}{u_2^2} \Rightarrow \frac{J_1}{E_1} = \frac{J_2}{E_2} \Rightarrow \frac{J}{E} = const. \quad (4.19)$$

Considering that the ions have initial energy E_q during quiet time and that they are accelerated according to the model to E_s during the disturbed time, the final differential particle flux J_s , can be calculated as a function of the initial J_q by:

$$J_s = \frac{E_s}{E_q}J_q \quad (4.20)$$

The energy spectra of sulfur, oxygen, helium ions and protons are calculated after the acceleration by the electric field and are shown in Figure 4.11 in red. Sulfur and oxygen ions are accelerated stronger than helium ions and protons within the given duration of the impulsive electric field, in accordance with Figure 4.10. From the ion energy spectra the relative ion abundance ratios can be calculated at a given energy/nuc. They are summarised and compared with those during the quiet time in Table 4.3. Substantial enhancements of the S/O, S/He and O/He during the disturbed time periods are generated while no significant change is produced for the p/He ratio.

Figure 4.12 shows the variations of the observed ratios during a part of the G2 orbit (in red), together with the average ratios during quiet time (in black). The modeled values (in green) are shown for comparison and they agree very well with the observed values of the S/O, S/He, O/He and p/He ratios for specific time periods. However, these results are produced by a typical single event, a better statistical study of the characteristics of such small-scale variations could give a more complete view of the ion composition in that region.

In addition the S/O, S/He, O/He and p/He ion abundance ratios after acceleration are calculated as a function of the impulsive time scale τ for the previous input parameters, shown in Figure 4.13. It is shown that the ratios exhibit a wide range of values with their maximum occurring at different time scales. This can explain the fact that the observed enhancements of the S/O, S/He and O/He are not in phase with those of the p/He ratio. Magnetic field variations with different characteristics result either in $\frac{\tau}{\tau_g} \ll 1$ or in $\frac{\tau}{\tau_g} \gg 1$ which corresponds to an adiabatic motion and none of the ratios is affected.

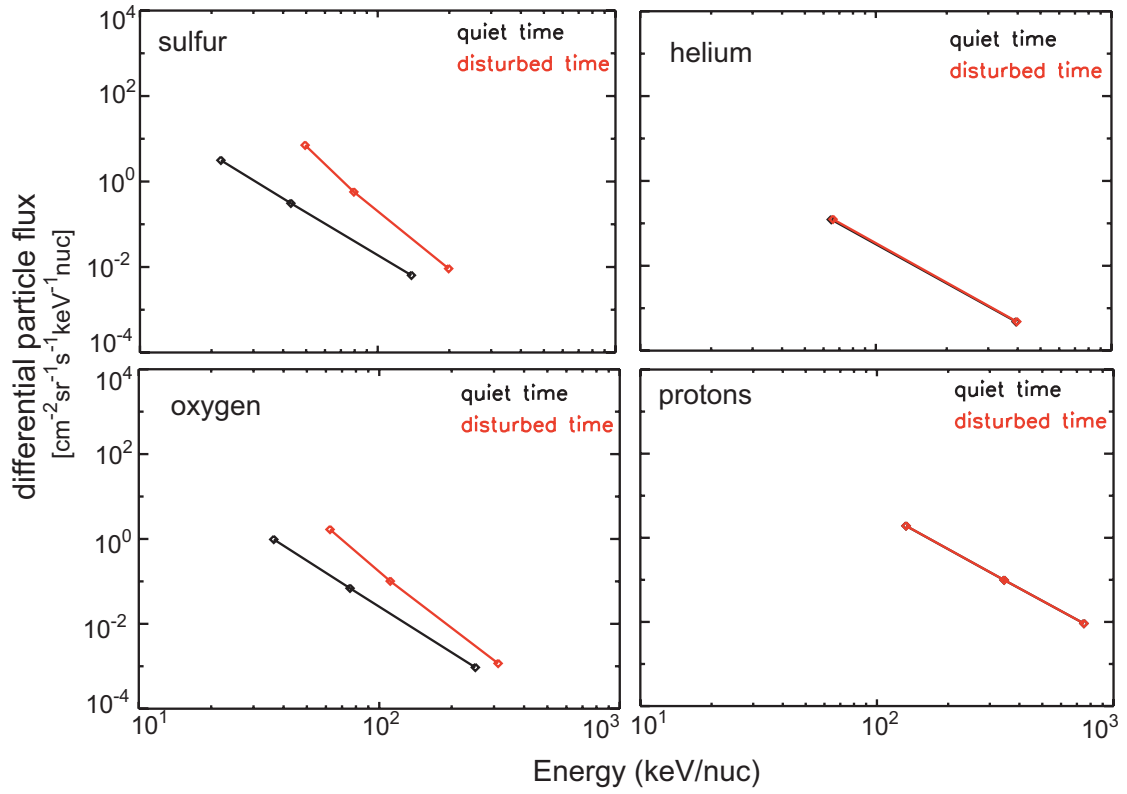


Figure 4.11: Sulfur, oxygen, helium and proton ion energy spectra from observations during a quiet time (black lines) along the C10 Galileo orbit (at $\sim 80 R_J$ and 1:40 LT) and spectra produced by the model for disturbed times (red lines).

Table 4.3: Observed ion abundance ratios during quiet time and modeled values for the disturbed period.

ion abundance ratio	quiet time (observed)	disturbed time (modeled)
S/O at 39 keV/nuc	0.59	1.54
S/He at 68 keV/nuc	0.66	11.5
O/He at 89 keV/nuc	0.85	6.05
p/He at 185 keV/nuc	139	134

Examples of the existence of such cases are shown at very few time periods along the disturbed time in Figure 4.12.

A reconfiguration event (substorm-like event) in the Jovian magnetotail can last a few days. In the present study such a global long-lasting event is not considered because the time scales of the magnetic field variation are not comparable with the particle gyroradius ($\tau \gg \tau_g$), the motion is adiabatic and the induced electric field can not accelerate the

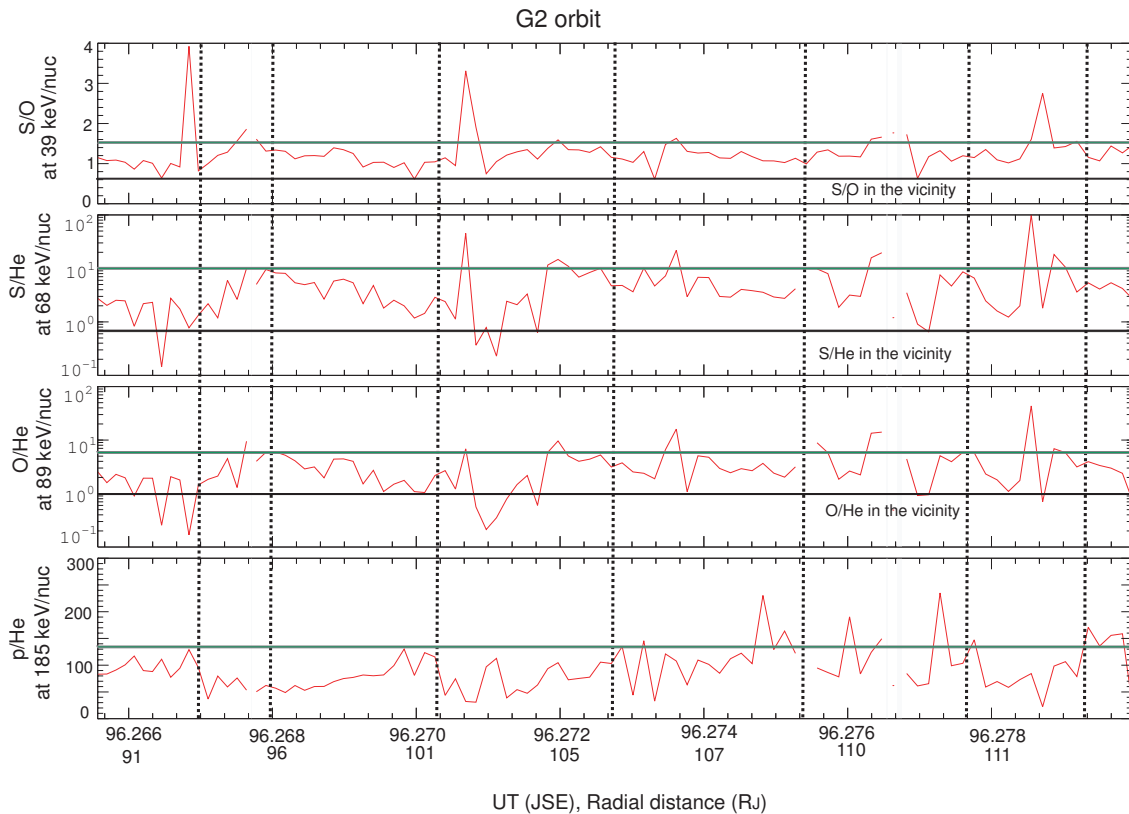


Figure 4.12: S/O, S/He, O/He and p/He ion abundance ratios (from top to bottom) in the same format as Figure 3.16. The observed ion abundance ratios are plotted in red, the black horizontal lines indicate the level of the ratio in the vicinity and the green lines are added to indicate the values derived by the accelerated spectra according to the model with input parameters $B = 3$ nT, $E_m = 1$ mV/m and $\tau = 3.4$ min. The vertical dashed lines indicate the onset of the reconfiguration events.

particles. Only the small-scale variations shown in Figure 4.6 affect the ion composition according to the above mechanism. Such events are observed frequently, approximately every 2 hours and widespread specifically in the predawn sector during the active phase of a reconfiguration event. Thus the acceleration mechanism described above can reproduce the observed ion abundance ratios along the G2 orbit during the time period where the reconfiguration events are present. Such events are also seen in the dusk sector but not as frequent (Kronberg 2006) and ion acceleration is moderate and does not lead to significant ion composition changes (Figure 3.18).

It should be noted that the present acceleration mechanism explains only locally the composition enhancements during the reconfiguration events in the predawn sector. However the particles accelerated in that region are expected to be transported inwards, in accordance with the flow pattern (see Figure 1.6) and will have an effect on the ion composition in other magnetospheric regions. Energetic particle measurements have shown evidence of such transport. Measurements between 25 and 80 R_J within 1 to 2 hours of

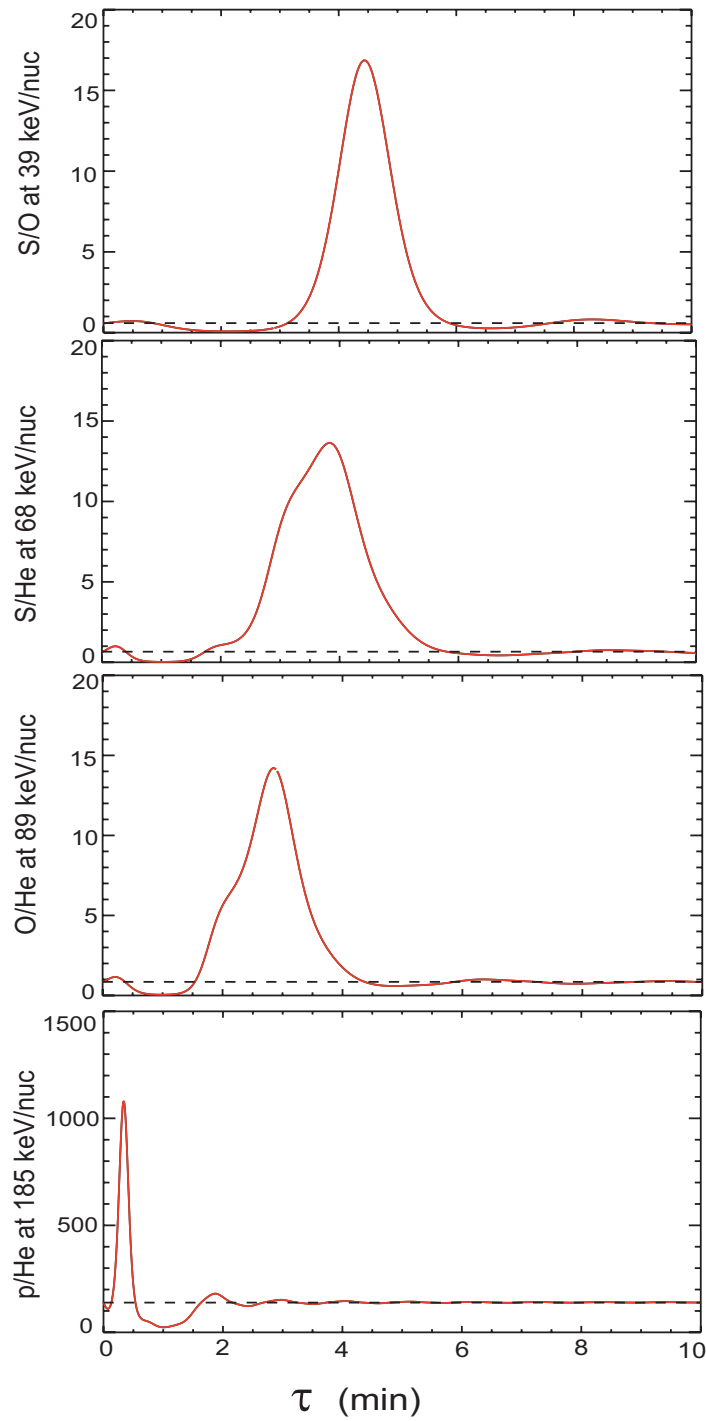


Figure 4.13: S/O, S/He, O/He and p/He ion abundance ratios as a function of the time variation of the electric field τ as predicted by the model, with model parameters $B_m = 3$ nT and $E_m = 1$ mV/m. The horizontal dashed lines correspond to the ratios observed during quiet time used as initial condition (Galileo orbit C10, at $\sim 80 R_J$ and 1:40 LT).

local midnight (parts of the Galileo orbits C9, C10) have shown quasi-periodic variations of energetic ion intensities and energy spectra. They are associated with the reconfigura-

tion events taking place in the predawn sector (Woch et al. 1998). The periodicity of these modulations linked them to the quasi-periodic transition between the two states of the Jovian magnetotail: the quiet dipolar-like state and the state with plasma sheet thinning and plasmoid formation (see section 1.2.2).

Two acceleration mechanisms are examined as candidates for the observed composition changes during reconfiguration events in the Jovian magnetotail. It is concluded that acceleration by small-scale magnetic field variations during such events can effectively accelerate ions and generate the observed ion abundance ratios, while acceleration in the current sheet due to the steady-state dawn to dusk electric field is not adequate to explain the composition changes.

5 Summary and conclusions

Based on the first 15 orbits of Galileo the composition of the energetic ion population of the Jovian magnetosphere has been studied for the first time on a global scale. More specific, three different types of ions are investigated: helium as the tracer of the solar wind, sulfur and oxygen as tracers of the internal source Io and protons with a mixed origin from the solar wind, Jovian atmosphere/ionosphere and the Europa gas torus.

Fundamental for the investigation of the ion composition is the study of the ion energy spectra, which provides information of the particle's source and any dynamical processes that have intervened from the time of the particle's injection until the detection. The Galileo energetic particle instrumentation provides measurements of the ion energy spectra in the power law part of the kappa distribution. The ion energy spectra show a break from a harder to a softer spectrum at energies of several keV/nuc. Since this spectral kink appears between the energy range of two detector systems of the energetic particle instrumentation the test of the reliability of the dataset is necessary prior to the study of the ion composition. An in-depth analysis proved that the instrument is well calibrated, and the observed ion energy spectra are not caused by instrumental effects. The ion energy spectral shapes of the Jovian magnetosphere are consistently found at various distances and local times.

Based on the observed ion energy spectra the relative ion abundance ratios of S/O, S/He, O/He and p/He at a specific energy/nucleon are derived and global maps are constructed. It is shown that the S/O ratio is rather stable and ranges between 0.4 to 1.2. However, these values should not be compared directly with the dissociation source of SO_2 . Sulfur and oxygen are emitted from the Io torus (with a neutral sources S/O ratio of 0.25 to 0.58) at energies of a few eV. They are transported and accelerated to several keV composing the global figure derived in this work. From the global maps it is also shown that helium dominates over oxygen and sulfur at larger distances, while the p/He ratio does not show a clear trend, consistent with the mixed origin of protons from the solar wind, Jovian atmosphere/ionosphere and the Europa gas torus. The global coverage of the Galileo trajectories enables a quantitative comparison with results of previous flyby missions, specifically of Voyager 2 for the same radial distance and local time. Based on the global maps the results from the two missions are compared for the same local time, radial distance and energy range. The observed large discrepancies are attributed to temporal variations between the two missions 17 to 19 years apart and to a strong energy dependence of the ion abundance ratios associated with the energy spectral shapes. Temporal variations of the ion abundance ratios not only on time scales of several years but also on several weeks, only implied by previous missions are now established. Results from consecutive Galileo orbits have shown pronounced variations of the S/O, S/He and O/He ratios, which could be related to the temporal variability of the Io torus emissions,

to the solar wind, but also to variations induced by particle acceleration processes. The less time-variable p/He ratio implies that protons originate to a large fraction from the solar wind.

A comparative study of the ion composition in different local time sectors is performed for the first time. The study shows that the relative ion abundance ratios exhibit only minor local time asymmetries, with an exception of the predawn sector, where the S/O, S/He and O/He ratio are very much enhanced. The observed composition changes in this region are associated with reconfiguration processes that occur in the magnetotail. The present study connects these reconfiguration events with substantial enhancements of the heavy ion composition apart from strong radial flow anisotropies, changes in the energy spectra of the energetic particles and polarity changes in the magnetic field north-south component.

The last part of this work investigates ion acceleration mechanisms which are at least partly responsible for establishing the observed ion abundance ratios. First, an attempt is made to explain the observed shape of the ion energy spectra, responsible for the energy dependence of the ion abundance ratios, by a model of ion stochastic acceleration by Alfvén waves. The observed ion energy spectra of the four species at three radial distances 10, 15 and 25 R_J are fitted by the model with wave spectra measurements in the Jovian magnetosphere as an input. The model parameters required for the acceleration exceed the Jovian magnetospheric scale indicating that the model of ion stochastic acceleration by Alfvén waves can not sufficiently explain the ion energy spectral shapes in the Jovian magnetosphere. Ion stochastic acceleration by Alfvén waves gives only diffusion in energy, and it is suggested that a combined model with radial diffusion could possible complement this work.

Additionally, the pronounced composition changes along the predawn sector are studied locally in terms of two candidate acceleration processes: ion acceleration in the tail by the time-stationary dusk to dawn electric field and ion acceleration by small-scale time variations of the south-north component of the magnetic field during reconfiguration events. It is concluded that the second one is responsible for the observed composition changes at that region. When the time scale of the magnetic field variation is comparable to the particle gyro period the particle is accelerated by the induced electric field. Based on observations of the magnetic field variations during the reconfiguration events in the Jovian magnetosphere it is shown that such a mechanism can energize sulfur and oxygen ions more effectively than helium and protons generating the observed ion abundances.

Bibliography

Bagenal F. and Sullivan J. D. (1981) , Direct plasma measurements in the Io torus and inner magnetosphere of Jupiter, *J. Geophys. Res.*, 86, 8447-8466.

Bagenal F., D. E. Shemansky, R. L. McNutt Jr., R. Schreier and Eviatar (1992), The abundance of O^{++} in the Jovian magnetosphere, *Geophys. Res. Lett.*, 19, 79-82.

Bame S. J. et al. (1992), Jupiter's Magnetosphere: Plasma Description from the Ulysses Flyby, *Science*, 257, 1539.

Barbosa D.D. (1979), Stochastic acceleration of solar flare protons, *Astrophys. J.*, 233, 383.

Barbosa D.D. (1981), On the injection and scattering of Protons in Jupiter's magnetosphere, *J. Geophys. Res.*, 86, 8981-8990.

Barbosa D.D., A. Eviatar and G. L. Siscoe (1984), On the acceleration of energetic ions in the Jupiter's magnetosphere, *J. Geophys. Res.*, 89, 3789-3800.

Barbosa D.D. (1994), Stochastic acceleration of energetic ions in Jupiter's magnetosphere, *J. Geophys. Res.*, 99, 13,509 - 13,520.

Brice, N. M. and G. A. Ioannidis (1970), The magnetospheres of Jupiter and Earth, *Icarus* 13, 173.

Burch, J. L. (1987), Plasma populations in the magnetosphere in *Solar wind and the Earth*, edited by S.-I. Akasofu and Kamide, pp. 103-122, Terra Scientific Company, Tokyo.

Burke, B. F. and K. L. Franklin (1955), Observations of a variable radio source associated with the planet Jupiter, *J. Geophys. Res.*, 60, 213.

Carr, T. D. and S. Gulkis (1969), The magnetosphere of Jupiter. *Ann. Rev. Astron. Astrophys.*, 7, 577-618.

Cheng, A. J., and A. F. Krimigis (1989), A model of global convection in the Jupiter's magnetosphere, *J. Geophys. Res.*, 94, 12,003-12,008.

Cheng, A. J. (1990), Current sheet interaction and particle acceleration in the Jovian magnetosphere, *J. Geophys. Res.*, 94, 4271-4276.

- Cheng, A. J. and R. B. Decker (1992), Nonadiabatic particle motion and corotation lag in the Jovian magnetodisk, *J. Geophys. Res.*, 97, 1397-1402.
- Cohen, C. M. S., E. C. Stone, and R. S. Selesnick (2001), Energetic ion observations in the middle Jovian magnetosphere, *J. Geophys. Res.*, 29, 871-881.
- Cooper, J. F., R. E. Johnson, B. H. Mauk, H. B. Garrett, and N. Gehrels (2001), Energetic ion and electron irradiation of the icy Galilean satellites, *Icarus* 149, 133-159.
- Cowley, S. W. H. and E. J. Bunce (2001), Origin of the main auroral oval in Jupiter's coupled magnetosphere-ionosphere system, *Planet. Space Sci.*, 49, 1067-1088.
- Delamere P.A. and F. Bagenal (2003), Modeling variability of plasma conditions in the Io torus, *J. Geophys. Res.*, 108, A71276, doi:10.1029/2002JA009706.
- Delamere P.A. A. Steffl and F. Bagenal (2004), Modeling temporal variability of plasma conditions in the Io torus during the Cassini era, *J. Geophys. Res.*, 109, A10216, doi:10.1029/2003JA010354.
- Delcourt, D. C., J. A. Sauvaud, and A. Pedersen (1990), Dynamics of single-particle orbits during substorm expansion phase, *J. Geophys. Res.*, 95, 20,853-20,865.
- Delcourt, D. C., J. A. Sauvaud, and T. E. Moore (1997), Phase bunching during substorm dipolarization, *J. Geophys. Res.*, 102, 24,313-24,324.
- Dungey, J. W. (1961), Interplanetary magnetic field and the auroral zones, *Phys. Rev. Lett.* 6, 47-48.
- Dungey, J. W. (1963), The structure of the exosphere or adventures in the velocity space edited by Dewitt, C., Hieblolt, J., Lebeau, A. in *Geophysics: The Earth's environment*, pp 505-550, Gordon and Breach, New York.
- Feldman, P. D., T. B. Ake, A. F. Berman, H. W. Moos, D. J. Sahnou, D. F. Strobel, H. A. Weaver, and P. R. Young (2001), Detection of chlorine ions in the Far Ultraviolet Spectroscopic Explorer spectrum of the Io plasma torus, *Astrophys. J.* 554, L123-L126.
- Fillius R. W. , C. E. McIlwain, A. Mogro-Campero (1975), Radiation belts of Jupiter: A second look, *Science*, 188, 464.
- Frank L. A. and W. R. Paterson (2001), Survey of thermal ions in the Io plasma torus with the Galileo spacecraft, *J. Geophys. Res.*, 106, 6131-6149.
- Fujimoto M., A. Nishida (1990), Monte Carlo simulation of energization of Jovian trapped electrons by resirculation, *J. Geophys. Res.*, 3841-3853.
- Geiss, J., et al. (1992), Plasma composition in Jupiter's magnetosphere: Initial results from the Solar Wind Ion Composition Spectrometer, *Science*, 257, 1535-1539.
- Goertz, C. K. The current sheet in Jupiter's Magnetosphere (1976), *J. Geophys. Res.*, 81,3368-3372.

Goertz, C. K. Energization of charged particles in Jupiter's outer magnetosphere (1978), *J. Geophys. Res.*, 83,3145-83,3150.

Hamilton, D. C., G. Gloeckler, S. M. Krimigis, C. O. Bostrom, T. P. Armstrong, W. I. Axford, C. Y. Fan, L. J. Lanzerotti, and D. M. Hunten (1980), Detection of energetic hydrogen molecules in Jupiter's magnetosphere by Voyager 2: Evidence for an ionospheric plasma source, *Geophys. Res. Lett.*, 7, 813 - 816.

Hamilton, D. C., G. Gloeckler, S. M. Krimigis, and L. J. Lanzerotti (1981), Composition of nonthermal ions in the Jovian magnetosphere, *J. Geophys. Res.*, 86, 8301 - 8318.

Hill, T. W., (1979), Inertial limit on corotation, *J. Geophys. Res.* 84, 6554-6558.

Hill, T. W., A. J. Dessler, and C. K. Goertz (1983), Magnetospheric models, in *Physics of the Jovian Magnetosphere*, edited by A. J. Dessler, pp. 353-394, Cambridge Univ. Press, New York.

Ioannidis, G. and N. Brice (1971), Plasma densities in the Jovian magnetosphere: Plasma slingshot or Maxwell demon?, *Icarus* 14, 360.

Jokipii J. R. (1971), Propagation of cosmic rays in the solar wind, *Rev. Geophys. Space Phys.*, 9, 27.

Kane, M., (1991), A convected kappa distribution model for hot ions in the outer Jovian magnetosphere, Ph.D. thesis, Johns Hopkins University, Baltimore, Md.

Kivelson, M. G. (1976), Jupiter's distant environment in *Physics of Solar Planetary Environments*, edited by D. J. Williams, p. 836, AGU, Washington, D. C.

Kivelson, M. G. and D. J. Southwood (2003), First evidence of IMF control of Jovian magnetospheric boundary locations: Cassini and Galileo magnetic field measurements compared, *Planet. Space Sci.*, 51, 891-898.

Khurana, K. K, M. Kivelson, V. M. Vasyliūnas, N. Krupp, J. Woch, A. Lagg, B. H. Mauk, W. S. Kurth (2004), The configuration of Jupiter's magnetosphere, In: Bagenal, F., T. Dowling, W. Mckinnon (Eds.), *Jupiter: The planet, Satellites and Magnetosphere*, Cambridge Planet. Science, Cambridge, 617-638.

Krimigis, S. M. and E. C. Roelof (1983), Low-energy particle population, in *Physics of the Jovian Magnetosphere*, edited by A. J. Dessler, pp. 106-156, Cambridge Univ. Press, New York.

Krimigis, S. M., et al. (1979), Low energy charged particle environment at Jupiter - A first look, *Science*, 204, 998 - 1003.

Krimigis, S. M. et al. (1979), Hot plasma environment at Jupiter: Voyager 2 results, *Science*, 206, 977 - 984.

Krimigis, S. M., J. F. Carbary, E. P. Keath, C. D. Bostrom, W. I. Axford, G. Gloeckler, L. J. Lanzerotti, and T. P. Armstrong, Characteristics of hot plasma in the Jovian magnetosphere: Results from the Voyager spacecraft, *J. Geophys. Res.*, 86, 8227.

- Krupp, N. (1994), Drei-dimensionale Richtungsverteilungen und relative Häufigkeiten energiereicher Ionen in der Magnetosphäre des Jupiter, Ph.D. thesis, Max-Planck-Institut für Aeronomie, Katlenburg-Lindau, Germany, June.
- Krupp, N., J. Woch, A. Lagg, B. Wilken, S. Livi, and D.J. Williams (1998), Energetic particle bursts in the predawn Jovian magnetotail, *Geophys. Res. Lett.*, 25, 1249-1252.
- Krupp, N., M. K. Dougherty, J. Woch, R. Seidel, and E. Keppler (1999), Energetic particles in the duskside Jovian Magnetosphere, *J. Geophys. Res. Lett.*, 104, 767-780.
- Krupp, N., A. Lagg, S. Livi, B. Wilken, and J. Woch (2001), Global flows of energetic ions in Jupiter's equatorial plane: First-order approximation, *J. Geophys. Res. Lett.*, 106, 26,017-26,032.
- Krupp, N., V. M. Vasyliūnas, J. Woch, A. Lagg, K. K. Khurana, M. G. Kivelson, B. H. Mauk, E. C. Roelof, D. J. Williams, S. M. Krimigis, W. S. Kurth, L. A. Frank and W. R. Paterson (2004), Dynamics of the Jovian Magnetosphere, In: Bagenal, F. , T. Dowling, W. Mckinnon (Eds.), *Jupiter: The planet, Satellites and Magnetosphere*, Cambridge Planet. Science, Cambridge, 617-638.
- Krupp, N., J. Woch , A. Lagg, S. Livi, D. G. Mitchell, S. M. Krimigis, M. K. Dougherty, P. G. Hanlon, T. P. Armstrong, and S. A. Espinosa (2004), Energetic particle observations in the vicinity of Jupiter: Cassini MIMI/LEMMS results, *J. Geophys. Res.*, 109, A09S10, doi:10.1029/2003JA010111.
- Kronberg, E. A., J. Woch, N. Krupp, A. Lagg, K. K. Khurana and K.-H. Glassmeier (2005), Mass release at Jupiter - substorm-like processes in the Jovian magnetotail, *J. Geophys. Res.*, 110, A03211, doi:10.1029/2004JA010777.
- Kronberg, E. A. (2006), Dynamics of the Jovian magnetotail, Ph.D. thesis, Max-Planck-Institut für Sonnensystemforschung, Katlenburg-Lindau, Germany.
- Kuppers, M. and N. M. and Schneider (2000), Discovery of chlorine in the Io torus, *Geophys. Res. Lett.* 27, 513-516.
- Lagg, A., *Energieriche Teilchen in der inneren Jupitermagnetosphäre: Simulation und Ergebnisse des EPD-Experimentes an Bord der Raumsonde Galileo*. University of Innsbruck, Austria, 1998.
- Lagg, A., N. Krupp, J. Woch (2003), In-situ observations of the neutral gas torus at Europa, *Geophys. Res. Lett.*, 30, 1556, doi:10.1029/2003GL017214.
- Lanzerotti, L., et al. (1992), The hot plasma environment at Jupiter: Ulysses results, *Science*, 257, 1518-1524.
- Lanzerotti, L., C. G. MacLennan, and D. M. Feldman (1993), Ulysses measurements of energetic H₃ molecules in Jupiter's magnetosphere, *J. Geophys. Res.*, 98, 21145-21149.
- Louarn, P., A. Roux, S. Perraut, W. Kurth, D. Gurnett (1998), A study of the large-scale dynamics of the Jovian magnetosphere using the Galileo plasma wave experiment, *Geophys. Res. Lett.* 25, 2905-2908.

- MacLennan, C. G., L. J. Lanzerotti, and A. Lagg (2001), Hot plasma heavy ion abundance in the inner Jovian magnetosphere ($< 10 R_J$), *Planet. Space Sci.*, 49, 275-282.
- Mall, U., J. Geiss, H. Balsiger, G. Gloeckler, A. B. Galvin, and B. Wilken (1993), Hydrogen from Jupiter's atmosphere in the Jovian magnetosphere, *Planet. Space Sci.*, 41, 947-951.
- Mauk, B. H., et al. (1996), Hot plasma parameters of Jupiter's inner magnetosphere, *J. Geophys. Res.*, 101, 7685-7695.
- Mauk, B. H., et al. (1998), Galileo-measured depletion of near-Io hot ring current plasmas since the Voyager epoch, *J. Geophys. Res.*, 103, 4715-4722.
- Mauk, B. H., et al. (2003), Energetic neutral atoms from a trans-Europa gas torus at Jupiter, *Nature*, 421, 920-922.
- Mauk, B. H., D. G. Mitchell, R. W. McEntire, C. P. Paranicas, E. C. Roelof, D. J. Williams, and S. M. Krimigis (2004), Energetic ion characteristics and neutral gas interactions in Jupiter's magnetosphere, *J. Geophys. Res.*, 109, A09S12, doi:10.1029/2003JA010270.
- McDonald F. B., A. W. Schardt, and J. H. Trainor (1979), Energetic protons in the Jovian magnetosphere, *J. Geophys. Res.*, 84, 2579.
- Mitchell, D. G., C. P. Paranicas, B. H. Mauk, E. C. Roelof, and S. M. Krimigis (2004), Energetic neutral atoms from Jupiter measured with the Cassini magnetospheric imaging instrument: Time dependence and composition, *J. Geophys. Res.*, 109, A09S11, doi:10.1029/2003JA010120.
- Morabito, L. A., S. P. Synnott, P. N. Kupferman, S. A. Collins (1979), Discovery of currently active extraterrestrial volcanism, *Science*, 204, 972.
- Nishida, A. (1976), Outward diffusion of energetic particles from the Jovian radiation belt. *J. Geophys. Res.* 81,1771-1773
- Ness N. F., M. H. Acuña, R. P. Lepping, L. F. Burlaga (1979), Magnetic field studies at Jupiter by Voyager 1: Preliminary Results, *Science*, 204, 982.
- Ness N. F., M. H. Acuña, R. P. Lepping, L. F. Burlaga, K. W. Behannon, F. M. Neubauer (1979), Magnetic field studies at Jupiter by Voyager 2: Preliminary Results, *Science*, 206, 966.
- Nosé, M., A. T. Y. Lui, S. Ohtani, B. H. Mauk, R. W. McEntire, D. J. Williams, T. Mukai, and K. Yumoto (2000a), Acceleration of oxygen ions of ionospheric origin in the near/Earth magnetotail during substorms, *J. Geophys. Res.*, 105, 7669-7677.
- Nosé, M., S. Ohtani, A. T. Y. Lui, S. P. Christon, R. W. McEntire, D. J. Williams, T. Mukai, Y. Saito, and K. Yumoto (2000b), Change of energetic ion composition in the plasma sheet during substorms, *J. Geophys. Res.*, 105, 23,277/23,286.

- Nosé, M., S. Ohtani, K. Takahashi, A. T. Y. Lui, R. W. McEntire, and D. J. Williams (2001), Ion composition of the near-Earth plasma sheet in storm and quiet intervals: Geotail/EPIC measurements, *J. Geophys. Res.*, 106, 8391-8403.
- Radioti A., N. Krupp, J. Woch, A. Lagg, K.-H. Glassmeier, L. S. Waldrop (2005), Ion abundance ratios in the Jovian magnetosphere, *J. Geophys. Res.*, 110, A07225, doi:10.1029/2004JA010775.
- Russell, C. T., K. K. Khurana, D. E. Huddleston, M. G. Kivelson (1998), Localized reconnection in the near Jovian magnetotail. *Science* 280, 1061-1064
- Russell C. T., D. E. Huddleston, K. K. Khurana and M. G. Kivelson (2000), Waves and fluctuations in the Jovian magnetosphere, *Adv. Space Res.*, 26, 1489-1489.
- Russell, C. T., (2001), The dynamics of planetary magnetospheres, *Planet. Space Sci.* 49, 1005-1030.
- Sánchez, E. R., B. Mauk, and C.-I. Meng (1993), Adiabatic vs. non-adiabatic particle distributions during convection surges, *Geophys. Res. Lett.*, 20, 177-180.
- Schardt, A. W., F. B. McDonald and J. H. Trainor (1981), Energetic particles in the predawn magnetotail of Jupiter, *J. Geophys. Res.*, 86, 8413-8428.
- Schreier R., A. Eviatar, V. Vasyliūnas, J. Richardson (1993), Modeling the Europa plasma torus, *J. Geophys. Res.*, 98, 21,231-21,243.
- Selesnick, R. S., C. M. S. Cohen, and K. K. Khurana (2001), Energetic ion dynamics in Jupiter's plasma sheet, *J. Geophys. Res.*, 106, 18,895-18,905.
- Sentman, D. D., J. A. Van Allen, and C. K. Goertz (1975), Recirculation of Energetic particles in Jupiter's magnetosphere, *Geophys. Res. Lett.* 2,465-2,468.
- Simpson, J. A., D. C. Hamilton, G. Lentz, R. B. McKibben, A. Mogro-Campero, M. Perkins, K. R. Pyle, and A. J. Tuzzolino (1974), Protons and electrons in Jupiter's magnetic field: Results from the University of Chicago Experiment on Pioneer 10, *Science*, 183, 306.
- Simpson, J. A., D. C. Hamilton, R. B. McKibben, A. Mogro-Campero, K. R. Pyle, and A. J. Tuzzolino (1974), The protons and electrons trapped in the Jovian dipole magnetic field region and their interaction with Io, *J. Geophys. Res.*, 79, 3522-3544.
- Smith E. J., L. Davis, D. E. Jones, D. S. Colburn, P. J. Coleman, P. Dyal, C. P. Sonett (1973), Magnetic field of Jupiter and its interaction with the solar wind, *Science*, 183, 305.
- Speiser T. W. (1965), Particle trajectories in model current sheets. 1. Analytical solutions, *J. Geophys. Res.*, 70, 4219-4226.
- Trainor, J. H., J. B. McDonald, B. J. Teegarden, W. R. Webber, and E. C. Roelof (1974), Energetic particles in the Jovian magnetosphere, *J. Geophys. Res.*, 79, 3600-3613.

- Van Allen, J. A., D. N. Baker, B. A. Randall, M. F. Thomsen, D. D. Sentman, H. R. Flindt (1974), Energetic electrons in the magnetosphere of Jupiter, *Science*, 183, 309.
- Van Allen, J. A., B. A. Randall, D. N. Baker, C. K. Goertz, D. D. Sentman, M. F. Thomsen, H. R. Flindt (1975), Pioneer 11 Observations of Energetic Particles in the Jovian Magnetosphere, *Science*, 188, 459.
- Vasyliūnas, V. M. (1971), Deep space plasma measurements, in *Methods of Experimental Physics*, vol. 9B, edited by R. H. Loveberg and H. R. Griem, p.49, Academic, San Diego, Calif.
- Vasyliūnas, V. M. (1975), Theoretical models of magnetic field-line merging, *Rev. Geophys. Space Phys.* 13,303-13,336.
- Vasyliūnas, V. M. (1983), Plasma distribution and flow, in *Physics of the Jovian Magnetosphere*, edited by A. J. Dessler, pp. 395-453, Cambridge Univ. Press, New York.
- Vogt, R. E., et al. (1979), Voyager 1: Energetic ions and electrons in the Jovian magnetosphere, *Science*, 206, 1003-1006.
- Vogt, R. E., A. C. Cummings, T. L. Garrard, N. Gehrels, E. C. Stone, J. H. Trainor, A. W. Schardt, T. F. Conlon, and F. B. McDonald (1979), Voyager 2: Energetic ions and electrons in the Jovian magnetosphere, *Science*, 206, 984-987.
- Waldrop, L. S. (2004), Probing the Structure Composition, and Dynamics of the Jovian Plasma Sheet with Energetic Particles, Ph.D. thesis, Boston University, Boston, USA.
- Walt, M., Introduction to geomagnetically trapped radiation, Cambridge University Press, Cambridge, 1994.
- Warwick, J. W., et al. (1979), Plasma observations near Jupiter: Initial Results from Voyager 1, 204, 987.
- Williams, D. J., R. W. McEntire, S. Jaskulek, and B. Wilken, (1992), The Galileo Energetic Particles Detector, *Space Sci. Rev.*, 60, 385-412.
- Woch, J., N. Krupp, A. Lagg, B. Wilken, S. Livi, D. J. Williams (1998), Quasi periodic modulations of the Jovian magnetotail, *Geophys. Res. Lett.* 25, 1253-1256.
- Woch, J., et al. (1999), Plasma Sheet Dynamics in the Jovian Magnetotail: Signatures for Substorm-like Processes?, *J. Geophys. Res.*, 26, 2137-2140.
- Woch, J., N. Krupp, A. Lagg (2002), Particle bursts in the Jovian magnetosphere: evidence for a near Jupiter neutral line, *Geophys. Res. Lett.*, 29, 10.1029/2001GL014080.
- Woch, J., N. Krupp, A. Lagg, A. Tomás (2004), The structure and dynamics of the Jovian energetic particle distribution, *Adv. Space Res.*, 33, 2030-2038.

Acknowledgements

First of all, I would like to thank my two supervisors at the Max-Planck-Institute für Sonnensystemforschung Dr. Norbert Krupp and Dr. Joachim Woch for guiding me through my project, for all their interest, support and patience, for motivating and encouraging me. I also would like to thank Andreas Lagg for providing the Galileo EPD software, without which this work would not be possible and also for the scientific contributions to this work. I am grateful to Prof. Dr. Karl-Heinz Glassmeier for the valuable discussions fundamental for the development of my thesis. Special thanks to Ana Tomás and Elena Kronberg for developing scientific discussions, for sharing the office and creating a very friendly and productive atmosphere.

I am thankful to the coordinator of the Solar System Research School, Dr. Dieter Schmidt for his support and help and for organising the seminars and the retreats, which contributed to the broadening of our knowledge.

I would like to thank the Director of the Institute Prof. Dr. Solanki, Prof. Dr. Christensen, to Prof. Dr. Vasyliūnas and the MPRS for financing this work and for giving me the opportunity to work in a stimulating scientific environment. This work was partly financed by the BMBF (Bundesministerium für Bildung and Forschung) by the DLR (Deutsches Zentrum für Luft- und Raumfahrt e.V.) under the contract 50 OH 0201. My thanks also to the PI of the EPD instrument D. Williams at JHU/APL.

Many thanks to the secretary of my group Sybilla Siebert-Rust for her precious help and for making all the problems look simple. My thanks also to Petra Fahlbusch for the support in all the paper work I needed to make here in Germany.

I would like especially to thank Prof. L. Vlahos and Prof. J.H. Seiradakis for supporting me during my undergraduation studies at the Aristotle University of Thessaloniki. Thank you for inspiring and motivating me to commence a Ph.D., thank you for believing in me.

I thank all the friends I made here in Lindau, to all the moments we shared and to those that will come.

Special thanks to Robert Chares for the mathematical support of this work and for his assistance with \LaTeX problems. In particular thank you for all your patience, love and courage.

Τέλος, ευχαριστώ την οικογένειά μου που με στήριξε τόσο στον επαγγελματικό όσο και στον προσωπικό μου αγώνα τα τρία αυτά χρόνια. Με εμπνεύσατε με αγάπη για την μάθηση και λαχτάρα για την έρευνα. Στην άπειρη συμπαράσταση, στην αστείρευτη υπομονη και αγάπη σας. Σας ευχαριστώ!

Curriculum Vitae

PERSÖNLICHE DATEN

Name	Aikaterini Radioti
Geburtsdatum	Februar 4, 1980
Geburtsort	Ptolemaida, Griechenland
Eltern	Antigoni Radioti und Georgios Radiotis
Staatsangehörigkeit	Griechisch

SCHULBILDUNG

1986-1991	Primary school, Ptolemaida, Greece
1991-1994	Secondary School (Gymnasium), Ptolemaida, Greece
1994-1997	Unified Lyceum with many branches of Ptolemaida, Ptolemaida, Greece

STUDIUM

1997-2002	Physics Diploma (Major: Astrophysics) - Diploma Thesis: "Conversion of EPN (European Pulsar Network) format to XML (eXtensible Markup Language) format", Department of Physics, School of Science, Aristotle University of Thessaloniki, Thessaloniki, Greece
-----------	---

PROMOTION

2003-2006	Stipendium des Max-Planck-Instituts für Sonnensystemforschung
-----------	---